DEPARTMENT OF PHYSICS
UNIVERSITY OF JYVÄSKYLÄ
RESEARCH REPORT No. 3/2007

PRECISION MASS MEASUREMENTS OF NEUTRON-RICH NUCLIDES AROUND A = 100

BY
ULRIKE HAGER

Academic Dissertation
for the Degree of
Doctor of Philosophy

To be presented, by permission of the
Faculty of Mathematics and Natural Sciences
of the University of Jyväskylä,
for public examination in Auditorium FYS-1 of the
University of Jyväskylä on July 9, 2007
at 12 o'clock noon

Jyväskylä, Finland
July 2007

ISBN 978-951-39-3182-7
URN:ISBN:978-951-39-3182-7

Preface

The work reported in this thesis was carried out during the years 2004-2007 at the Department of Physics of the University of Jyväskylä, and at the ISOLDE facility at CERN, Geneva. I would like to thank the whole staff of the Department of Physics for the friendly working atmosphere.

I wish to thank my supervisor professor Juha Äystö for giving me the opportunity to carry out this work, and for his guidance and support. I would also like to thank the members of the IGISOL group, past and present, especially Dr. Stefan Kopecky, Dr. Ari Jokinen, Tommi Eronen, Jani Hakala, Viki Elomaa, Dr. Iain Moore and Thomas Kessler.

Part of this work was carried out at CERN, and I would like to thank the whole ISOLTRAP group for their warm welcome. Martin Breitenfeldt, Romain Savreux, Mélanie Marie-Jeanne, Michael Dworschak, Dr. Chabouh Yazidjian and Dr. Alexander Herlert have made my time at CERN not only educational but also fun. In addition, I would like to express my warmest thanks to Dr. habil. Klaus Blaum for his support and the interest he showed in my work.

The financial support from the Graduate School of Particle and Nuclear Physics is gratefully acknowledged.

Finally, I would like to thank my family, especially my brothers, for their support and encouragement.

Abstract

The masses of 73 neutron-rich fission products were measured with high precision using the JYFLTRAP Penning trap setup at the IGISOL facility in Jyväskylä. These new data enable mapping of the mass surface in this region of the nuclear chart. The data are compared to nuclear model calculations, and various systematic trends are analysed. Since these measurements are part of one of the first precision mass measurement campaigns conducted at JYFLTRAP, the systematic uncertainties of the setup were explored and quantified as far as possible. In addition, analysis programs had to be written to handle the raw data efficiently.
At the mass spectrometer ISOLTRAP, CERN, a new project was initiated to install a tape station at the end of the setup. Exploiting the high resolving power of this setup, this will provide the possibility for decay spectroscopy with pure samples. A first design for the new apparatus is presented in this work.

Contents

List of Figures

List of Tables

1 Introduction

An important parameter in studies of nuclear structure and in nucleosynthesis is the mass of the nucleus, which is connected to the mass of its constituents and the binding energy:

$$M(N,Z) = N \cdot m_n + Z \cdot m_p - B(N,Z) \tag{1.1}$$

with m_n the mass of the neutron, m_p the mass of the proton and $B(N,Z)$ the binding energy of a nucleus with N neutrons and Z protons. Therefore, from the exact knowledge of the nuclear masses follow the binding energies, which in turn are needed for models of nuclear interactions.

For several decades the neutron-rich region between $A \approx 80$ and $A \approx 130$ has been subject to intense study via decay spectroscopy. The reason for this is the suggested shape transition in the rhodium, palladium region from an SU(5) vibrational state to a O(6) γ-unstable state, as noted by Stachel *et al.* [1], though no sharp onset of deformation was expected. Indication of this transition was also found by Aryaeinejad *et al.* [2] for neutron-rich palladium, suggesting that the occupation of the $\nu h_{11/2}$ orbital may cause the very slow change in excitation energies from $N = 64$ to $N = 70$ and lead to oblate deformation. Lhersonneau *et al.* [3] noted that nuclei with $N \geq 60$ have strong ground state quadrupole deformations, while the intermediate $N = 59$ isotones of strontium, yttrium and zirconium still have spherical ground states. This rapid change is explained by unusually large deformations on the one hand and a strong subshell closure on the other hand. Houry *et al.* [4] agree on the importance of the $\nu h_{11/2}$ orbital, but claim prolate rather than oblate deformation. Additionally, the deformation parameter is calculated to decrease with increasing mass, leading smoothly to a quasi-spherical shape for ^{121}Pd without the need for shape transitions. More recently, it has been suggested that the $N = 82$ shell closure might weaken or be quenched far from stability. This quenching has been predicted by models and experimental indication has been found [5]. Shell closures manifest, for example, in sudden jumps in the evolution of the two-neutron separation energy S_{2n} along an isotopic chain. One example of the appearance of a neutron subshell was found at $N = 60$ around the zirconium region, as described in [3], and could recently be confirmed by measurements conducted with JYFLTRAP [6]. That work has since been continued towards the neutron shell closure at $N = 82$ by measuring neutron-rich isotopic chains of technetium, ruthenium, rhodium and palladium, and also towards lighter nuclei, i.e. isotopes of rubidium and bromine.

Another reason for interest in this region of the nuclear chart is its importance for stellar nucleosynthesis, as the rapid neutron capture process (r-process), is assumed to proceed here, producing more than half the nuclei heavier than iron existing in the universe today [7].

A variety of methods have been developed to measure nuclear and atomic masses (for an overview over different methods, see [8]). One of these is the Penning trap, which employs a strong magnetic field combined with an electric quadrupole field to trap ions. These ions can then be excited at their cyclotron frequency, a process which is mass selective. This method was first employed for radioactive species at ISOLTRAP at the ISOLDE facility at CERN. At the IGISOL facility at the University of Jyväskylä a double Penning trap system, JYFLTRAP, has been installed. It consists of a trap for isobaric beam purification and one for precision mass measurements. This latter trap

was commissioned in 2003. Some of the first data taken with it is presented in this work.

Another application of the Penning trap is to provide a pure sample for decay spectroscopy, reducing the background considerably. Such trap-assisted spectroscopy has already been conducted at JYFLTRAP [9]. A similar setup is planned for ISOLTRAP.

The experimental work presented in this thesis was carried out at the JYFLTRAP experiment at the accelerator laboratory of the University of Jyväskylä and at the ISOLTRAP experiment at ISOLDE, CERN. The author of this thesis was involved in commissioning the JYFLTRAP precision trap and in preparing and performing the subsequent precision mass measurements. She has written a data analysis program and analysed all the data presented in this work. At the ISOLTRAP experiment, the author has begun the design of a tape station setup for trap-assisted decay-spectroscopy, including ion-optical simulations and various technical drawings.
The thesis is based on the following enclosed publications:

First Precision Mass Measurements of Refractory Fission Fragments
U. Hager, T. Eronen, J. Hakala, A. Jokinen, V. S. Kolhinen, S. Kopecky, I. Moore, A. Nieminen, M. Oinonen, S. Rinta-Antila, J. Szerypo, and J. Äystö
Phys. Rev. Lett. 96 (2006) 042504

Precision mass measurements of neutron-rich Tc, Ru, Rh and Pd isotopes
U. Hager, V.-V. Elomaa, T. Eronen, J. Hakala, A. Jokinen, A. Kankainen, S. Rahaman, S. Rinta-Antila, A. Saastamoinen, T. Sonoda, J. Äystö
Phys. Rev. C 75 (2007) 064302

Precise atomic masses of neutron-rich Br and Rb nuclei close to the r-process path
S. Rahaman, U. Hager, V.-V. Elomaa, T. Eronen, J. Hakala, A. Jokinen, A. Kankainen, P. Karvonen, I. D. Moore, H. Penttilä, S. Rinta-Antila, J. Rissanen, A. Saastamoinen, T. Sonoda and J. Äystö
Eur. Phys. J. A, 32 (2007) 87

Precision mass measurements of neutron-rich yttrium and niobium isotopes
U. Hager, A. Jokinen, V.-V. Elomaa, T. Eronen, J. Hakala, A. Kankainen, S. Rahaman, J. Rissanen, I. D. Moore, S. Rinta-Antila, A. Saastamoinen, T. Sonoda, J. Äystö
accepted for publication in Nucl. Phys. A

This thesis consists of the following chapters:

Chapter 2 gives a short introduction to global nuclear models and pairing, and then explains the principles of the astrophysical r-process.

Chapter 3 compares different techniques used to measure the mass of the nucleus.

Chapter 4 describes the experimental methods used in this work at both IGISOL in Jyväskylä, and ISOLDE at CERN, starting with the production of radioactive ion beams (RIBs) and going on to give an overview of the Penning traps installed at the two facilities.

Chapter 5 presents the data taken at JYFLTRAP and its analysis. Systematic trends in the mass surface are examined.

Chapter 6 deals with the ongoing effort of placing a tape station at the end of the ISOLTRAP beam line for trap-assisted spectroscopy.

2 Nuclear masses

2.1 Global mass models

Figure 2.1 shows the nuclear binding energy per nucleon as a function of the mass number A. The binding energy per nucleon is roughly 8 – 8.5 MeV, with a maximum around iron.
The first attempt at theoretically describing the binding energy of the nucleus was the semi-empirical mass formula by von Weiszäcker [11]. This *liquid drop model* is based on the assumption that the nucleus behaves like a drop of nuclear matter. The density distribution is assumed to be constant inside a sharp boundary and zero outside. A good approximation for the radius of a nucleus is then

$$R = r_0 \cdot A^{1/3} \; ; \; r_0 \approx 1.3 \text{ fm} \tag{2.1}$$

The total binding energy depends on the volume ($\propto A$), the surface area of the nucleus ($\propto A^{2/3}$), the Coulomb repulsion between the protons ($\propto \frac{Z^2}{A^{1/3}}$) and the proton-neutron asymmetry ($\propto \frac{(N-Z)^2}{A}$). From this follows the semi-empirical Weizsäcker formula for the binding energy:

$$B = a_{vol} \cdot A - a_{sur} \cdot A^{2/3} - a_{coul} \cdot \frac{Z^2}{A^{1/3}} - a_{asymm} \cdot \frac{(N-Z)^2}{A} + \delta(A) \; . \tag{2.2}$$

The additional $\delta(A)$ term comes from pair binding, which increases the binding energy for nuclei of even proton or neutron number. The factors a_{vol}, a_{sur}, a_{coul}, a_{asymm} and δ are obtained by fitting to the experimental data. The pairing can be approximated by $\delta \approx 12A^{-1/2}$ MeV [12].

The liquid drop model describes the approximate development of the binding energy for increasing mass number quite well, with the largest binding energies being found around iron. As can be seen from Fig. 2.1, though, the binding energy is not a completely smooth function of the mass number. Increasingly precise mass measurements have revealed structures not described in the liquid drop model. Certain nuclei with so-called magic proton or neutron numbers are found to be especially stable. This observation led to the introduction of the shell model, also known as the independent particle model. The formation of a shell structure requires a common field in which the particles move largely independently of each other, leading to the conclusion that the nucleonic interactions must smooth themselves out into a mean field.

Different approaches are used to combine the liquid-drop and shell model aspects of the nucleus into one model. The most fundamental of these is the Hartree-Fock (HF) model [10], which is based on solving the Schrödinger equation with a model wave function using effective interactions. For heavier nuclei this method becomes computationally demanding due to the large dimensionality of the matrix of the exact Hamiltonian to be diagonalised in a basis of shell-model states. As a simplification, one can assume that all nucleons move in a single-particle field, that is, an independent-particle model. The trial wave function takes the form of a Slater determinant (the wave function of a many-fermion system satisfying the Pauli principle) and variational methods are employed to find the solution. Different effective forces are used in these calculations, a popular one being the Skyrme force [8], which is of zero range and includes a three-body term. It's 5 parameters are adjusted to the experimental

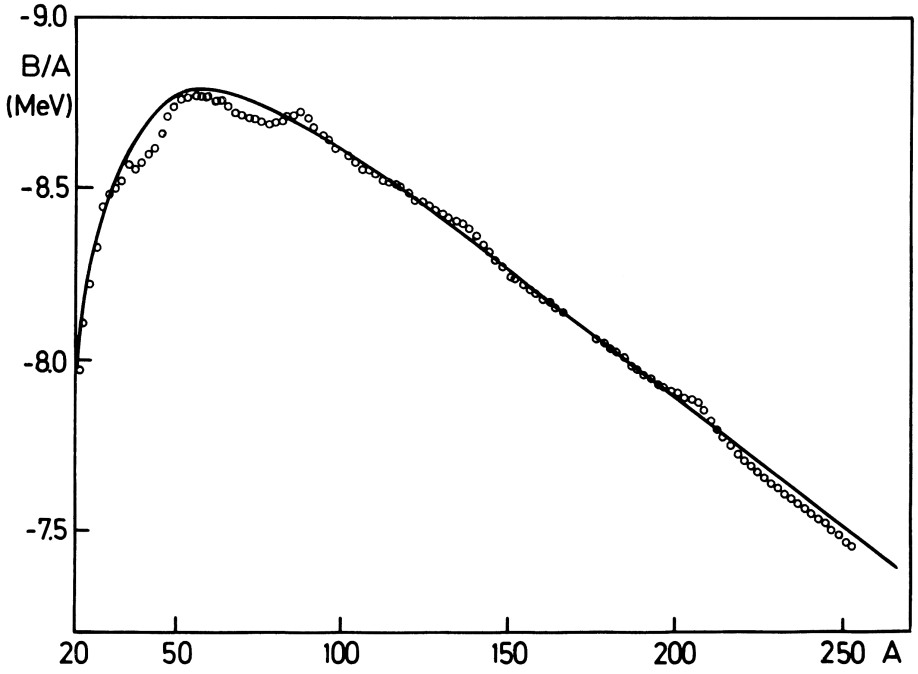

Figure 2.1: Nuclear binding energy per nucleon as a function of mass number A. The circles mark experimental values, the line was calculated using Eq. 2.2. The picture was taken from [10].

binding energies and radii.

Not all experimentally observed features can be explained in this mean-field picture but rather have to be expressed as a configuration mixing of Slater determinants. One of these features is the pairing of like nucleons; if a nucleus has an even number of both protons and neutrons, the nucleons will couple to yield the angular momentum 0. This also shows in the binding energies in that nuclides with even proton or neutron numbers are bound more strongly than their neighbours of odd particle number. In analogy to the theory of superconductivity, pairing correlations can be included in the HF approach by applying the BCS (Bardeen-Cooper-Schrieffer) method. In the resulting HF-BCS model [13], the pairing is treated as constant and not variational like the single-particle functions. The Hartree-Fock-Bogoliubov (HFB) model [14], on the other hand, is fully variational, and the pairing correlations are treated similarly to the single-particle part. Another problem of the mean-field calculations is that they systematically underbind $N = Z$ nuclei. An additional, so-called Wigner term has been proposed to correct for this effect, though a more direct description in terms of proton-neutron pairing seems more suitable. An important change that was made in the second version of the HFB model, HFB-2, compared to HFB-1 is the treatment of the pairing cutoff [15], i.e. the single-particle states included in the pairing calculation. In the HFB-1 calculations the cutoff energy was $\hbar\omega = 41A^{-1/3}$ MeV, whereas for the HFB-2 the spectrum was confined to an interval around the Fermi energy of $E_F \pm 15$ MeV. While the former approach leads to a narrowing of the available spectrum for neutrons as one moves towards the neutron dripline, the latter one actually widens the single-particle spectrum included in the neutron-pairing calculations. This will result in the weakening of the neutron-shell far from stability, i.e. shell quenching, which indeed seems to be confirmed by experiment.

A different way of combining the liquid-drop and the shell model is to graft microscopic corrections onto the liquid-drop model, also called the microscopic-macroscopic ('mic-mac') approach. Various models have evolved from this idea. One of these is the finite-range droplet model (FRDM) [16]. As opposed to the drop model, the droplet model takes into account the finite thickness of the nuclear surface and the finite compressibility of nuclear matter. The densities are thus only approximately constant in a system with a diffuse surface region. The finite range of the nucleonic interaction is accounted for by the Yukawa force. Shell corrections are included using the Strutinsky averaging method; also included are BCS pairing corrections and a Wigner term. The adopted pairing parametrisation leads to a steady weakening of the pairing gap when moving towards the neutron dripline. Therefore, no shell quenching is predicted.

A mic-mac model closer to the HF method is the ETFSI (extended Thomas-Fermi plus Strutinski integral) algorithm [17]. It is based on the Skyrme force, and the energy of the nuclide is calculated using the Thomas-Fermi approximation (i.e. the energy of the system is calculated using a functional of the particle density). Since the Thomas-Fermi approximation, originating from atomic physics, is not well suited for many-body systems with very short-range two body forces, an extended Thomas-Fermi (ETF) method is used. From this the macroscopic part is derived. The microscopic part is calculated based on the same Skyrme force as the macroscopic part, hence both parts are more closely related than is the case for the FRDM. The model yields a close approximation to the HF calculations, with the advantage of being faster. With increasing computational power, however, it becomes less important.

More fundamental than the mic-mac models is the mass formula by Duflo and Zuker [18]. Similar to the HF calculations, it assumes effective interactions, pseudopotentials, but then separates the Hamiltonian into monopole and multipole terms. The former gives the single-particle properties, while the latter describes the residual interactions with a very general configuration mixing. In this manner, the model includes pairing and Wigner correlations, and the magic numbers arise naturally. Though the model disagrees with experimental results around $N_0 = 50$, it does reproduce experimental trends around both $N_0 = 82$ and $N_0 = 126$ and predicts strong quenching of these shells. Two versions of the model exist, one with 28 free parameters, and another with 10 parameters. Yet another, less fundamental way of obtaining a mass formula is the KUTY/KTUY model [19]. It again consists of two parts, one describing global trends, the other one fluctuations about these trends. The model fits 34 parameters to the data, more than the other models. When moving towards the neutron dripline, this model binds more strongly than the FRDM.
The models discussed above have been compared to some of the data presented in this work in [20, 21].

2.2 Pairing and deformation

As stated in the introduction, deformation plays an important role in the region around neutron-rich zirconium. A unified shell-model [22] picture can be employed in order to explain – to some extent – these properties. In this model, a shell structure that persists even for strong collective behaviour is assumed. A central potential representing the average interaction of the nucleons leads to the existence of a shell structure, where single-particle levels group into shells with small energy gaps separated by larger energy gaps. These levels all have the same parity (normal levels), except for one of opposite parity (intruder level). Since the energy gap between shells is large, once a shell is filled, the nucleons will form an inert core and the nuclear properties arise from the behaviour of the valence nucleons above that shell.

The interaction of two nucleons with each other depends on whether they are identical or not. Identical nucleons interact strongly in the case that they both occupy the same orbit (nlj) and

couple to $J^\pi = 0^+$. This is called pairing. Otherwise the short range of the nuclear force together with the Pauli principle, which keeps like nucleons apart, will hinder interaction. However, once such a pair of nucleons is formed, the pair as a whole can be scattered into a different valence orbit, leading to a smearing out of the Fermi surface. The pairing is stronger the larger the angular momentum and the larger the spatial overlap. Since the outer nucleons in heavier nuclei are further apart, the pairing strength decreases with increasing mass number. On the other hand, a proton and a neutron can interact in any pair of orbits $(n_\pi l_\pi j_\pi)$ and $(n_\nu l_\nu j_\nu)$. The strength of the interaction is determined by the respective orbits [22] and is particularly large for

$$n_\pi = n_\nu \text{ and } \frac{l_\nu - l_\pi}{l_\nu + l_\pi} \text{ small} . \tag{2.3}$$

In other orbits, the neutron-proton matrix elements will be weaker than those for the pairing of like nucleons.

One consequence of the pairing interaction of like nucleons is that the ground state spin and parity of odd-mass nuclei is determined by the spin of the last unpaired nucleon. Another consequence is that the interaction between like nucleons, due to the very weak quadrupole force, will produce only spherical shapes. The neutron-proton interaction, on the other hand, has a strong quadrupole component, which can produce deformation. Therefore, deformation will occur when the neutron-proton correlations dominate over those of like nucleons. In a system of N_n valence neutrons and N_p valence protons, the energy due to pairing is proportional to the number of valence nucleons, since each nucleon can only couple with one like nucleon,

$$E_{pair} \propto M_{pair}(N_n + N_p) , \tag{2.4}$$

where M_{pair} is an average of the relevant pairing matrix elements. The neutron-proton interaction, by contrast, is proportional to the product of valence protons and neutrons, since any neutron and proton can interact,

$$E_{n-p} \propto M_{n-p} N_n N_p , \tag{2.5}$$

with M_{n-p} being an average of the neutron-proton quadrupole matrix elements. In most cases, M_{n-p} is smaller than M_{pair}. Still, for sufficiently large numbers of valence nucleons, E_{n-p} will dominate over E_{pair}. If, however, the active shell is small, E_{n-p} will dominate only if the conditions given in Eq. 2.3 are met, leading to larger matrix elements M_{n-p}.

In addition to the quadrupole part of the neutron-proton interaction, the monopole component plays an important role in shifting the spherical single-particle energies. This component, too, is strongest between protons and neutrons in orbits fulfilling Eq. (2.3). Once the protons and neutrons are filling pairs of such orbits, the spectrum of single-particle levels can change rapidly. To study the behaviour of a single-particle level in a deformed potential, Nilsson [23] used a modified harmonic oscillator potential, though a more realistic calculation can be performed using a Woods-Saxon potential. The $(2j+1)/2$-fold degeneracy of the spherical orbits is broken in such a potential, and j is no longer a good quantum number. Commonly, the asymptotic quantum numbers $\Omega^\pi[Nn_z\Lambda]$ are used to describe the state, where Ω is the projection of the single-particle angular momentum onto the symmetry axis, see Fig. 2.2, N is the principle quantum number, n_z is the number of oscillator quanta along the symmetry axis, i.e. the number of nodes in the wave function along the symmetry axis, and Λ the projection of the orbital angular momentum l_i on the symmetry axis. The parity π is given by $(-1)^N$. The resulting level schemes relevant to the region covered in this work as a function of the deformation are shown in Figs. 2.3 and 2.4.

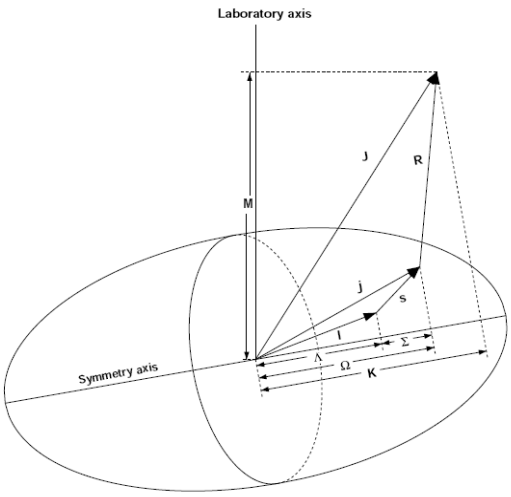

Figure 2.2: Schematic view of a deformed nucleus, taken from [24]. M is the projection of total angular momentum J on the laboratory axis, R the angular momentum from the collective motion of the nucleus, Ω the projection of total angular momentum j (orbital l plus spin s) of the odd nucleon on the symmetry axis, and Λ the projection of angular momentum along the symmetry axis. $\Omega = \Lambda + \Sigma$ where Σ is the projection of intrinsic spin along the symmetry axis.

2.3 The astrophysical r-process

As mentioned above, about half of the elements heavier than iron existing in the universe today are assumed to have been produced in the r-process [7, 25]. This process takes place in an environment with a high neutron density $n_n \approx 10^{24}/\mathrm{cm}^3$ and a temperature of $T \approx$ 1-2 GK. Under these conditions neutron-capture will be faster than β-decay. The neutron-capture reactions will proceed until an equilibrium is reached between neutron-capture (n,γ) and photodisintegration (γ,n). The respective reaction rates are connected by

$$\lambda_{\gamma n} \propto \frac{T^{3/2}}{N_n} e^{(-\frac{S_n}{k_B T})} \lambda_{n\gamma}$$

When this waiting point is reached, the reaction stops and waits for β-decay.

$$(Z, A+i) \rightarrow (Z+1, A+i) + \beta^- + \overline{\nu}$$

From the resulting nuclide (Z+1,A+i) a new reaction chain starts, absorbing neutrons until the next waiting point is reached. Thus, the r-process path lies about 10–20 neutrons to the neutron-rich side from stability. The neutron separation energy at the waiting point at a given temperature T and neutron density N_n is the same for all proton numbers and is about $S_n \approx 3$ MeV. When the neutron flow stops freeze-out occurs and the neutron-rich nuclei β-decay to stable isobars. The longer than average β-decay half-lives at the magic number waiting points result in larger abundances for these nuclides. Thus, the r-process abundance peaks at $A \approx$ 80,130,195 due to the closed neutron shells at $N =$ 50,82,126. Possible astrophysical sites for the r-process to occur are Type II Supernovae and Neutron Star Mergers. A part of the r-process path, relevant to this work, is shown in Fig. 2.5.

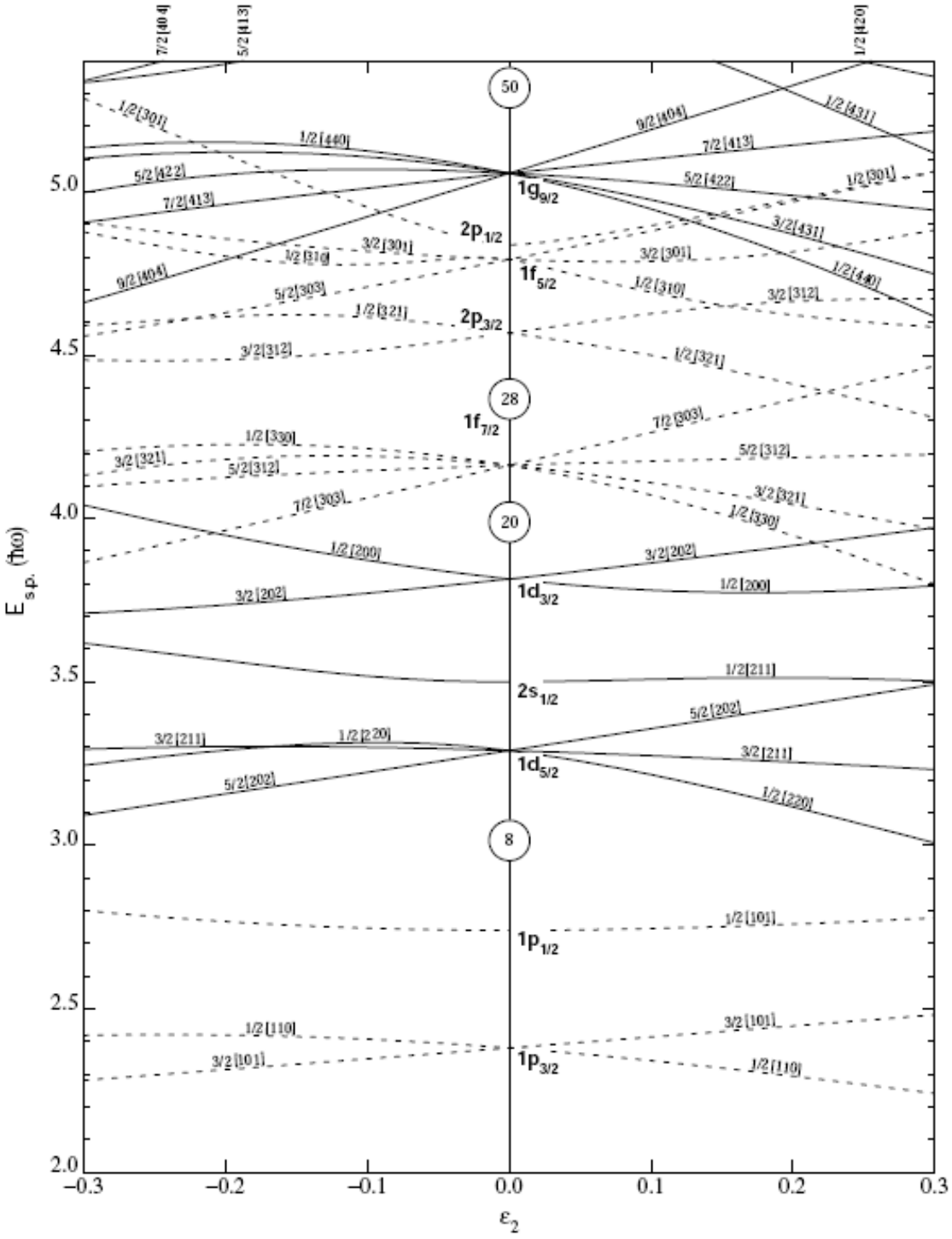

Figure 2.3: Nilsson diagram for neutrons and protons with Z or $N \leq 50$, taken from [24].

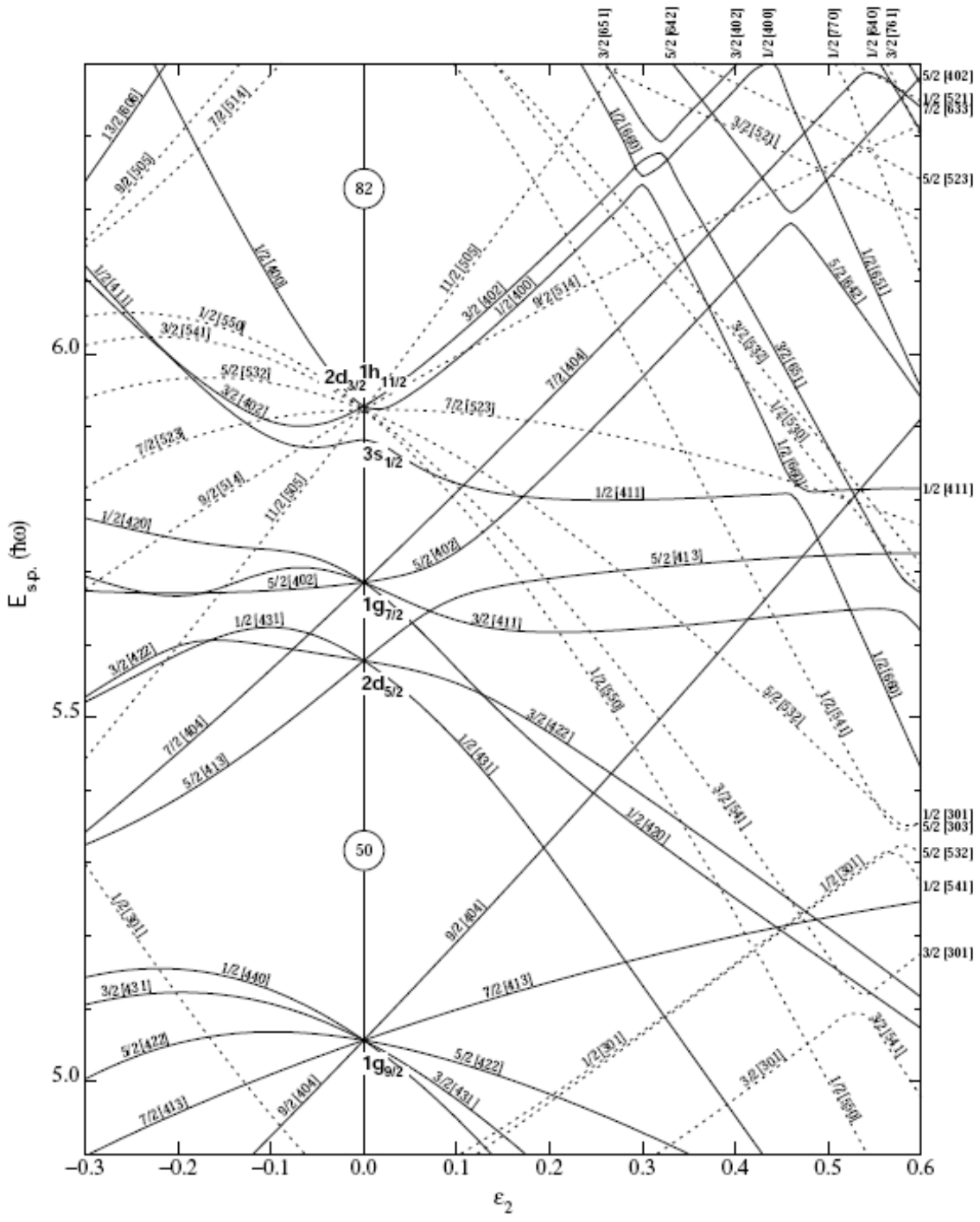

Figure 2.4: Nilsson diagram for neutrons $50 \leq N \leq 80$, taken from [24].

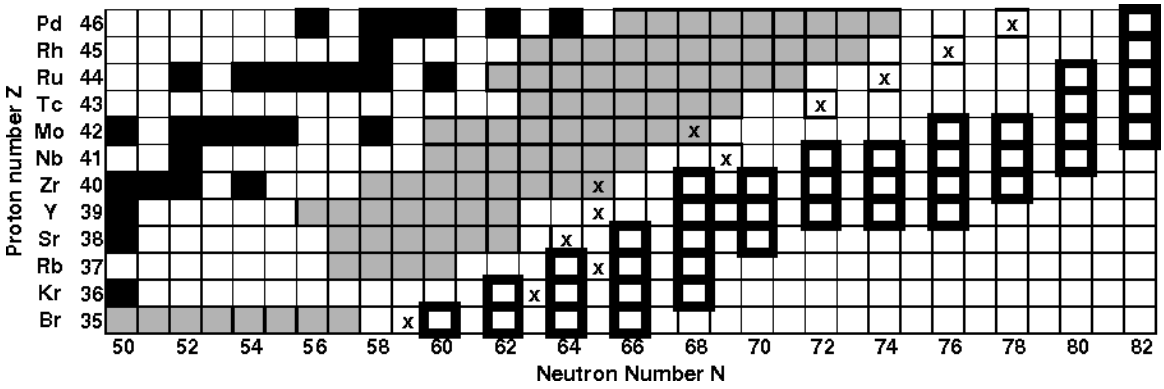

Figure 2.5: Schematic outline of the stellar r-process relevant to this work. The thick squares mark the assumed path of the r-process [26], the black filled boxes mark stable nuclei, the filled grey boxes denote masses studied at JYFLTRAP [6, 20, 21, 27]. The crosses mark the heaviest isotope of each element with known half-lives [28, 29].

3 Mass measurement techniques

Mass measurement techniques are often divided into indirect, i.e. reaction and decay, and direct measurements, e.g time-of-flight measurements, as the former yield mass differences rather than masses. Since, however, the direct techniques rely on reference masses, these, too, do not yield absolute masses, unless the reference mass is ^{12}C, on which the atomic mass unit is based.

3.1 Indirect techniques

A nuclear reaction $A(a,b)B$ can be used to determine the mass of the unknown product B if the incoming and outgoing particles and the target mass are known. In addition, the kinematics of the unknown mass or the reaction Q-value must be determined. These requirements limit the applicability of reaction studies somewhat. However, since B does not need to be bound, it is possible to study nuclei that would otherwise not be accessible.

The mass of a radioactive nuclide can also be derived from its decay Q-value. This, however, will only yield a mass difference between parent and daughter nucleus; obtaining the mass of the parent requires linking this mass difference to a known mass, which can be quite far away, thus leading to cumulative errors along a decay chain. Additional uncertainties arise from an insufficient knowledge of the decay scheme, where high-lying decay branches might not be detected. β decay is especially complicated in that it is a three-body process, with a neutrino being emitted along with the β-particle carrying away part of the decay energy:

$$A(Z,N) \rightarrow A(Z+1,N-1) + e^- + \overline{\nu}_e \; ; \; \beta^-$$

It is therefore necessary to determine the maximum energy of the β particle, the endpoint of the β spectrum.

3.2 Direct techniques

3.2.1 Time-of-flight measurements

An example of using a time-of-flight measurement to determine the mass of a nucleus is the spectrometer SPEG located at GANIL [30]. The nuclides produced in fragmentation reactions are preseparated in a α-shaped spectrometer. They then enter the SPEG, where their magnetic rigidity $B\rho$ and their velocity are measured. The flight path is 82 m, leading to a typical time of flight of 1 μs. The detector response limits the time resolution to about $2 \cdot 10^{-4}$. The determination of the magnetic rigidity by a position sensitive detector achieves a relative momentum resolution of about 10^{-4}. The advantages of SPEG are its single-ion sensitivity and the short measurement time enabling a rough mapping of the mass surface very far from stability. In order to improve the resolution of a time-of-flight measurement, a longer flight path is needed. This can be achieved by using a cyclotron, where the ion path increases to over 1 km, as is done at the CSS2 at GANIL [31]. A mass resolution of $3 \cdot 10^{-5}$ can be reached for nuclides with half-lives down to a few tens of μs.

3.2.2 Storage rings

The revolution frequency of an ion in a storage ring depends on the circumference, which in turn depends on the ion optical settings. For an ensemble of ions, the difference in revolution frequencies is determined by the different mass to charge ratios $\Delta(m/q)/(m/q)$ and the different velocities $\Delta v/v$

$$\frac{\Delta f}{f} = -\frac{1}{\gamma_t^2}\frac{\Delta(m/q)}{m/q} + \frac{\Delta v}{v}\left(1 - \frac{\gamma^2}{\gamma_t^2}\right). \tag{3.1}$$

γ_t is the so-called transition energy at which the revolution frequency is independent of the energy for an ion species with fixed m/q-ratio and depends on the ion optical settings of the storage ring and can thus be varied. For relation 3.1 to be velocity independent and thus enable mass measurements, the second term on the right hand side must be zero. This can be achieved either by reducing the velocity spread Δv, or by operating the ring in isochronous mode with $\gamma = \gamma_t$. Reducing the velocity spread is a prerequisite of Schottky mass spectrometry [32] and requires an ion-cooling mechanism. One possible method is stochastic cooling using an active electronic feedback system. This is most effective for hot beams and therefore suited for pre-cooling. A second technique is electron cooling, where the hot ions are cooled in collisions with cold, collinear electrons, resulting in beams of small size and momentum spread. The cooling time is proportional to the cube of the velocity spread. Electron cooling works better the lower the initial temperature of the ions.

Once the highly-charged ions are cooled, the revolution frequency of the ions can be measured by sampling the induced signal – the Schottky noise – in a pair of electrodes. From this, an ion's mass can be derived if a reference mass is present in the ring at the same time for calibration. With this method many different ion species can be studied simultaneously with single-ion sensitivity. However, the relatively long cooling times set a limit on the half-life of the nuclide of about a second. With this method mass resolving powers of better than 10^6 have been reached [33]. Isochronous mass spectrometry does not suffer this limitation, as no cooling is required. The ions are injected at the transition energy, rendering the revolution time for a certain species independent of the velocity. A thin-foil detector placed in the ions' path registers each passage of each stored ion. Thus a time-of-flight spectrum is obtained from which the masses can be derived if a suitable reference mass is present. The number of simultaneously stored ions is limited to about 50, but the single ion sensitivity remains. A resolving power of about 10^5 has been reached [34].

3.2.3 Radio frequency transmission spectrometers

The MISTRAL experiment [35, 36] at ISOLDE, CERN combines a magnetic mass spectrometer with a time-of-flight spectrometer. It determines the cyclotron frequency ν_c of an ion in a homogeneous magnetic field from transmission peaks. The ions enter the field and follow a helicoidal trajectory for two turns. After one half turn their kinetic energy is modulated using a radio frequency signal. The change in kinetic energy leads to a changed cyclotron radius. One turn later, this modulation is repeated. If the modulation frequency ν_{RF} is

$$\nu_{RF} = (n + 1/2)\nu_c \tag{3.2}$$

the net effect of the two modulations is zero. Only ions for which this is the case are transmitted through a narrow slit and are detected. Since no cooling or other beam preparation is required, this method is very fast, and hence very short-lived ($T_{1/2} \approx 10$ ms) nuclides are accessible. The mass resolving power is limited by the emittance of the ISOLDE beam and the width of the exit slit. A resolving power of better than 10^5 can be reached.

3.2.4 Penning traps

Penning traps employ a superposition of a strong homogeneous magnetic field with a weak electric quadrupole field to trap ions. The determination of the ion's cyclotron frequency $\nu_c = \frac{qB}{2\pi m}$ relative

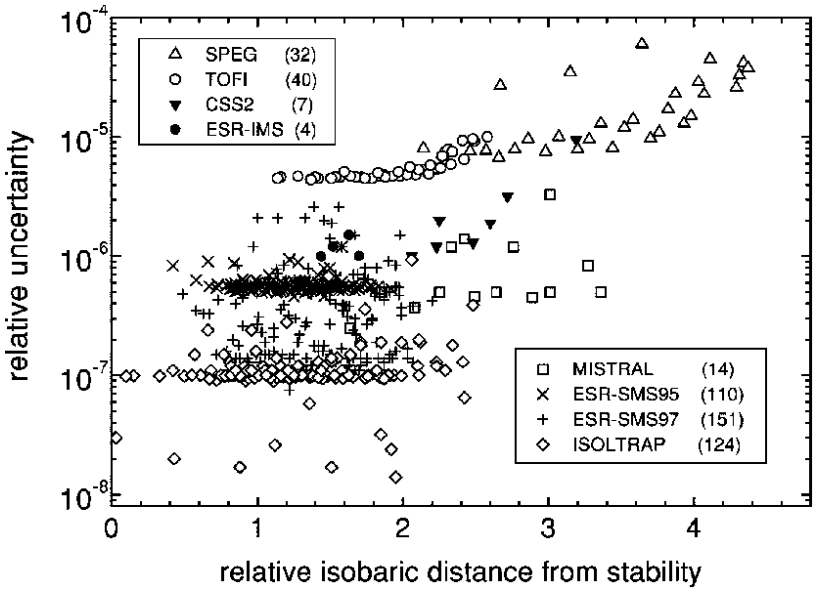

Figure 3.1: Uncertainties of different mass measurement techniques, taken from [8]. The numbers in brackets give the number of points for each experiment.

to a well-known reference nuclide yields the ion's mass. Penning traps have been used to measure the masses of nuclides with half-lives down to about 60 ms, and relative precisions of $\leq 10^{-8}$ can be reached [37]. The working principle of the Penning trap will be explained in more detail in Chapter 4.

3.2.5 Comparison

The precisions that can be reached by different direct mass measurement techniques are compared in Fig. 3.1. As can be seen, the farther one goes from stability, the lower the reached precision. The highest precisions are currently reached in Penning trap measurements, whereas the SPEG spectrometer can access nuclides the farthest from stability. A more detailed comparison is given by Lunney et al. [8].

4 Experimental methods

The experiments described in this work were conducted using the JYFLTRAP setup at the IGISOL facility in Jyväskylä, Finland. Additional work was conducted at the ISOLTRAP setup at ISOLDE, CERN, Switzerland. Both experiments use the ISOL-method to produce radioactive beams which are first prepared in an RFQ-cooler/buncher and then transferred to a double Penning trap setup.

4.1 Radioactive ion beam production

4.1.1 Overview

Different methods exist to produce beams of radioactive ions for different applications. The two most common techniques are the in-flight separation and the on-line isotope separation (ISOL). The former produces high-energy beams by fragmentation, preserving the forward momentum of the fragments, while for the latter the nuclear reaction products are stopped and reaccelerated. In the following, the ISOL technique will be described in more detail.

4.1.2 The ISOL technique

To produce radioactive nuclei, a target is bombarded with high-energetic particles from an accelerator, inducing spallation, fission and fragmentation reactions. The reaction products are stopped either in the thick target, or, if a thin target is used, stopped in a separate catcher. This is schematically shown in Fig. 4.1. In the case of a thick target, the nuclides are evaporated out by heating the target and then transferred to an ion source, where they are ionised using e.g. surface, plasma or laser ionisation. In either case the ions are reaccelerated and mass separated using a bending magnet.

4.1.3 IGISOL

The working principle of the IGISOL technique [38] is shown in Fig. 4.2. The beam coming from the accelerator, the JYFL K130 cyclotron, hits the target and induces nuclear reactions. The products of these reactions recoil out of the target and are stopped in helium gas at a pressure of about 100–300 mbar. Because of charge exchange processes with the gas the ions will be singly charged, or even be neutralised in the presence of a plasma. The ions are then transported with the helium flow out of the chamber. A skimmer or a sextupole ion beam guide is placed outside the exit hole to reduce the helium flow to the beamline. The neutralised reaction products are pumped away with the helium. The singly-charged positive ions, however, are accelerated towards the extraction electrode.

Different ion guides are available, depending on the nuclear reaction needed to produce the desired reactions products:

- The *Light-Ion Ion Guide* will give a beam of neutron-deficient ions produced in proton-, deuteron- or ^{3}He-induced fusion evaporation reactions (e.g. (p,xn)) on a target. Since the

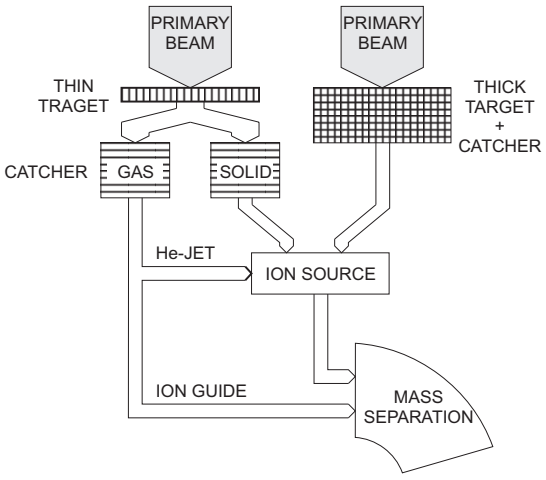

Figure 4.1: ISOL methods, using thick or thin targets with solid or gaseous catcher.

reaction products have a small recoil energy, the target is placed inside the gas chamber

- The *HIGISOL Heavy-Ion Ion Guide* is used for reactions induced by a primary beam of heavier nuclei creating a compound nucleus which subsequently decays. Since the reaction products have a large forward momentum distributed in a cone shape, the target is placed outside the gas cell, and the primary beam is prevented from entering the cell by a beam stopper located in front of the cell's entrance window. Because of the ions' large kinetic energy, the gas cell is operated at higher buffer gas pressures of over 200 mbar.

- The *Fission Ion Guide*, Fig. 4.3, is used to produce neutron-rich isotopes by proton- or neutron-induced fission of uranium or thorium. The resulting ions cover a large mass range due to the asymmetric fission of uranium. The target is placed outside the stopping volume at an angle of 7° with respect to the beam, leading to an effective thickness of 120 mg/cm^2. Separating the target from the stopping volume avoids the problem of beam-induced plasma forming in the buffer gas. The buffer gas pressure in the gas cell is between 100 and 400 mbar.

The IGISOL technique is chemically non-selective and very fast (sub-ms).

4.1.4 ISOLDE

The ISOLDE facility [39] at CERN, Switzerland, can provide beams of about 800 isotopes of over 60 different elements with half-lives down to a few milliseconds for volatile elements. It uses the classical ISOL technique, with 1.4 GeV protons from the Proton Synchrotron booster impinging on a thick target and inducing fission, spallation and fragmentation reactions in the target. The protons are pulsed, which on the one hand side means great stress for the target during the impact of the high-intensity bunch, but on the other hand also enhances the release of short-lived species from the target. The reaction products diffuse out of the target, a process enhanced by the heating of the target to about 2000°C. The atoms can be ionised in different ways, for example, an ECRIS and the laser ion

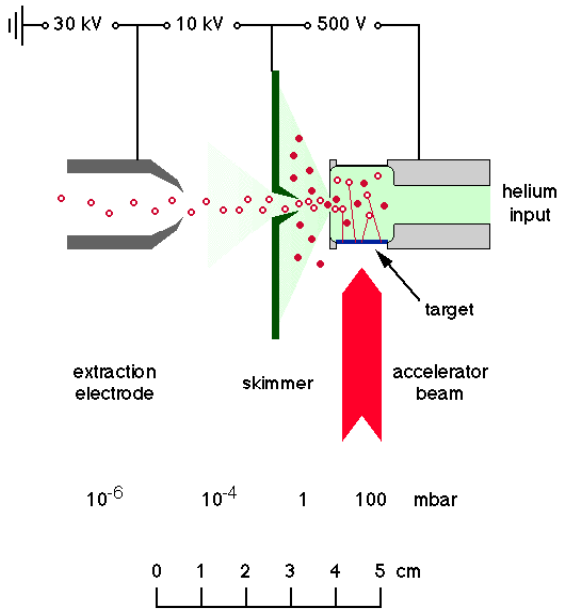

Figure 4.2: IGISOL working principle, the empty red circles indicate ions, the filled ones have been neutralised in charge exchange reactions with the buffer gas.

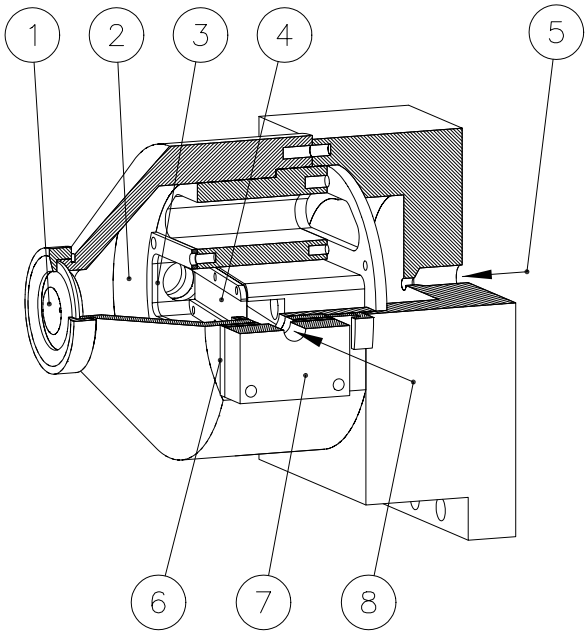

Figure 4.3: The fission ion guide. The numbered parts are 1) the exit nozzle, 2) the stopping volume, 3) the separating foil, 4) the uranium target, 5) the helium inlet, 6) beam window, 7) graphite collimator, and 8) the accelerator beam.

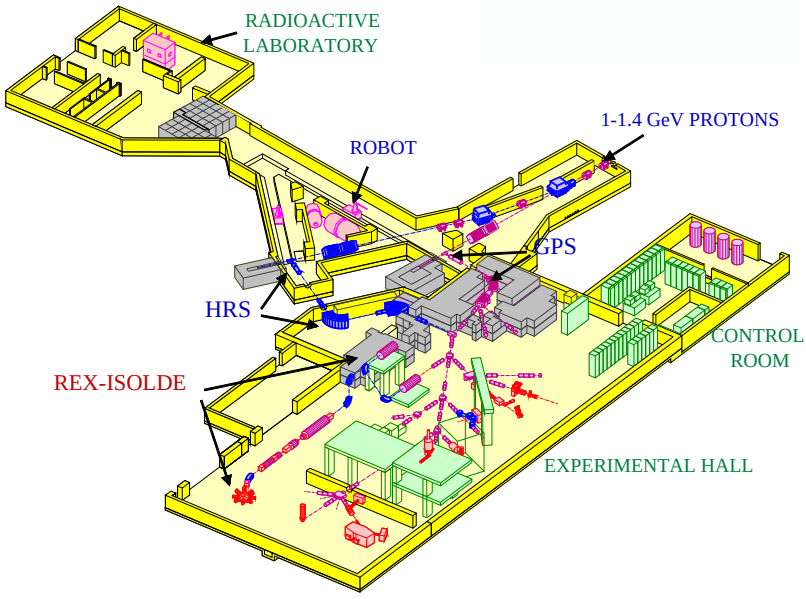

Figure 4.4: Schematic layout of the ISOLDE hall

source setup RILIS are available. The ions are accelerated to typically 60 keV and mass separated, for which two magnetic mass separator systems have been implemented, namely the General Purpose Separator (GPS) and the High Resolution Separator (HRS). The GPS consists of a 60° bending magnet with a resolving power of about 1000, followed by a switchyard, where the primary beam can be split into three beams within a mass range of ±15% from the central mass, which can be sent to three different experiments simultaneously. The HRS consists of two bending magnets, the first one of 90°, and the second one of 60° in the opposite direction. A resolving power of 15000 can be reached, while during normal operation a resolving power of 5000 is typically achieved. The resulting radioactive ion beam typically has a transverse emittance of the order of $\epsilon_{95\%} \approx 10 - 20\pi$-mm-mrad, and an energy spread of normally less than a few eV. Its intensity is proportional to the target thickness, the primary beam intensity, the production cross section, and the release and ionisation efficiency, which in turn depend on the element and isotope to be produced, on the target and on the ion source. This technique is chemically selective, as volatile elements will easily leave the target, whereas refractory elements cannot be extracted at all. This can be an advantage, as it reduces the background, but at the same time it limits the range of available beams. To enhance the extraction of a certain element, chemically reactive elements or molecules can be added, which form molecules of higher vapour pressure with the elements to be extracted. Additional chemical selectivity is provided by the choice of the ion source, with laser ion sources producing almost clean beams of one element.

4.2 Radio frequency-coolers/bunchers

Since the ion beams produced by the ISOL method are DC beams and usually have too large an emittance and energy spread for direct injection into a magnetic field, linear Paul traps are used to prepare the beams for injection into a Penning trap. When the ions enter the cooler, they are first decelerated by an electrostatic lens system. They then enter the radio frequency quadrupole (RFQ), a structure of four parallel rods with an oscillating radio frequency field of opposing phases applied to adjacent rods. This focuses the ions towards the center of the structure, trapping them in the transverse direction. The rods are each divided into segments, so that different potentials can be

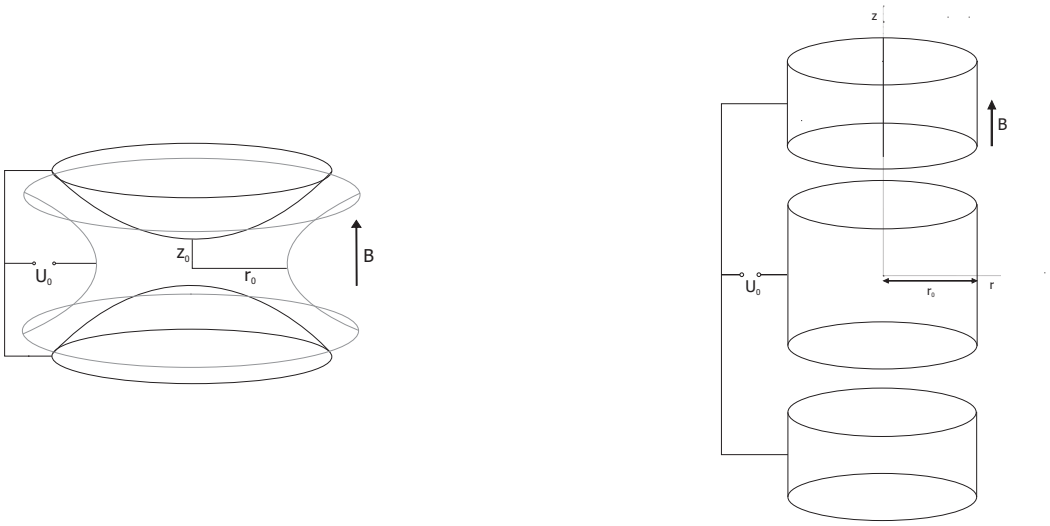

Figure 4.5: Two possible Penning trap electrode structures: using a hyperboloid ring electrode (left), and a cylindrical electrode (right). Correction electrodes are not shown.

applied along them to form a potential well into which the ions are guided along the cooler axis and where they are stored and bunched. In order to cool the ions, the RFQ is filled with helium buffer gas. The thermalised ions are then extracted out of the cooler and re-accelerated.

4.3 Penning traps

4.3.1 Principles

A Penning trap employs an electric quadrupole field in combination with a strong homogeneous magnetic field to trap ions. There are two methods commonly used to create the quadrupole field: (1) a hyperboloid ring electrode with two endcap electrodes, with the surfaces of the electrodes following the equipotential surfaces of the field, or (2) a set of cylindrical ring electrodes which together form the field around the axis of the central electrode. Both possibilities are shown schematically in Fig. 4.5. Method (1) has the advantage of a very precise field geometry, whereas method (2) is a more open construction and simplifies the injection of ions or buffer gas into the trap. Otherwise, the methods are equivalent, and the motion of ions in the traps can be described in the same way.

An ion of charge q and mass m_{ion} in a magnetic field B with a velocity component v perpendicular to the magnetic field will perform a circular motion with the angular frequency

$$\omega_c = \frac{q}{m_{ion}} \cdot B \tag{4.1}$$

and radius $\rho = v/\omega_c$. The frequency $\nu_c = \omega_c/2\pi$ is the ion's cyclotron frequency. The ion is thus bound in the radial direction. The electric quadrupole field in the trap provides confinement in the axial direction, and gives rise to a potential of the form

$$U(\rho, z) = \frac{U_0}{2z_0^2 + r_0^2} \cdot (2z^2 - \rho^2) \tag{4.2}$$

where $2z_0$ is the spacing between the endcap electrodes, and r_0 is the inner radius of the ring

electrode. For the motion in the axial direction, this leads to the equation of motion

$$m\ddot{z} + \frac{qU_0}{d^2}z = 0 \tag{4.3}$$

where d is the characteristic trap dimension

$$4d^2 = r_0^2 + 2z_0^2 \ .$$

This equation describes a harmonic oscillation; the angular frequency is

$$\omega_z = \sqrt{\frac{qU_0}{md^2}} \ . \tag{4.4}$$

To describe the motion in the radial direction, both the electric and the magnetic field have to be included in the equation of motion

$$-m\frac{v^2}{\rho} = -q \cdot v \cdot B + q\frac{U_0}{2d^2}\rho \ . \tag{4.5}$$

Using the above relations for ω_c and ω_z, and $\omega = v/\rho$ this leads to

$$\omega^2 = \omega_c \cdot \omega - \frac{1}{2}\omega_z^2 \ . \tag{4.6}$$

This quadratic equation has the two solutions

$$\omega_\pm = \frac{\omega_c}{2} \pm \sqrt{\frac{\omega_c^2}{4} - \frac{\omega_z^2}{2}} \ . \tag{4.7}$$

There are thus two types of radial motion, ω_+ is called the reduced cyclotron frequency and ω_- is the magnetron frequency. Following this, the position of an ion in the trap is given by

$$x = \rho_+ \cos(\omega_+ t + \phi_+) + \rho_- \cos(\omega_- t + \phi_-) \tag{4.8}$$

$$y = \rho_+ \sin(\omega_+ t + \phi_+) + \rho_- \sin(\omega_- t + \phi_-) \tag{4.9}$$

$$z = \rho_z \cos(\omega_z t + \phi_z) \ , \tag{4.10}$$

where $\rho_{+,-,z}$ and $\phi_{+,-,z}$ are the amplitudes and phases of the three types of motion, respectively. The three superposed motions of an ion in the trap are depicted in Fig. 4.6.

From Eq. 4.7 it is obvious that the sum of both radial frequencies equals the true cyclotron frequency.

$$\omega_c = \omega_+ + \omega_- \ . \tag{4.11}$$

Since this sum frequency only depends on the magnetic field B and the charge-over-mass ratio of the ions, measuring it allows for mass determination if the charge is known and the magnetic field can be determined by measuring a reference ion of well-known mass. From Eq. 4.7 it can also be seen that $\omega_+ > \omega_-$, and with normal settings $\omega_+ >> \omega_-$. It also follows that to first order the magnetron motion is mass independent

$$\omega_- \approx \frac{U_0}{2Bd^2} \ . \tag{4.12}$$

The potential energies of the radial motions are given by

$$-q\frac{U_0}{d^2}\rho_\pm^2 = -m\rho_\pm^2\omega_z^2 = \frac{m}{2}\rho_\pm^2(\omega_+\omega_-) \ , \tag{4.13}$$

and the total energy of the ion in the trap is the sum of the energies of all three types of motion

$$E = \frac{m}{2}\rho_z^2(\omega_z^2) + \frac{m}{2}\rho_+^2(\omega_+^2 - \omega_+\omega_-) + \frac{m}{2}\rho_-^2(\omega_-^2 - \omega_+\omega_-) \ . \tag{4.14}$$

The total energy of the radial eigenmotions is proportional to $(\omega_\pm^2 - \omega_+\omega_-)$. Considering again that $\omega_+ > \omega_-$, it can be seen that the total energy of the magnetron motion is in fact negative while that of the cyclotron motion is positive. Thus, energy loss will lead to an increase of the magnetron motion's amplitude whereas the amplitudes of the cyclotron and axial motion will decrease.

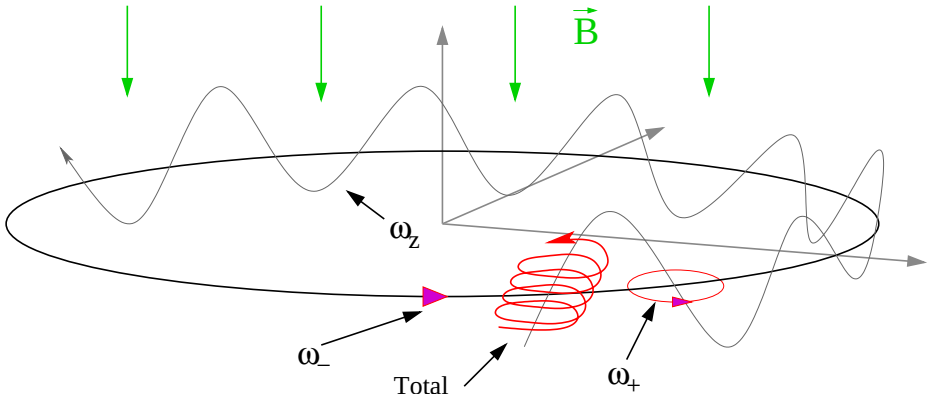

Figure 4.6: Motion of an ion in the trap. ω_- is the magnetron motion, ω_+ the reduced cyclotron motion, ω_z the axial motion.

Dipole excitation Each of the eigenmotions can be excited independently by a dipole rf field of the corresponding frequency. For the axial motion, the exciting field has to be in the axial direction, i.e. between the endcaps, while for the two radial motions a radial field is needed. To create this field the ring electrode has to be split into segments and the rf voltage applied between opposite segments. The applied field will cause the motion's amplitude to increase. However, depending on the initial phase of the external rf field and the position of the ion, it might initially decrease [40]. Radial dipole excitation can thus be used to place the ions in a certain orbit. Since the magnetron frequency is almost mass independent, an excitation at this frequency will affect all ions, while an excitation at the reduced cyclotron frequency only increases the radius for ions of a specific mass.

Quadrupole excitation The ion motion can be excited at sums and differences of the three eigen frequencies. The two motions can thus be coupled and the one converted into the other and back, this is called beating. The most important quadrupole excitation is that at $\omega_+ + \omega_- = \omega_c$. The azimuthal quadrupole needed to create the rf field requires the ring electrode to be split into four segments. The rf voltage is then applied between adjacent segments. The conversion time from one pure motion to the other pure motion depends on the magnetic field B and the amplitude of the rf field V_{rf}

$$T_{conv} = 4\pi a^2 \frac{B}{V_{rf}} \,. \tag{4.15}$$

a is the radius at which V_{rf} is the potential and can be approximated by the inner radius of the ring electrode. If the frequency of the excitation field does not match the ion's cyclotron frequency, the conversion will be incomplete. The energy gain of the ion motion can be given as a function of the detuning $\Delta\omega = \omega_{rf} - \omega_c$

$$E_r(\Delta\omega) = \frac{q^2 V_{rf}}{32ma^2} \frac{\sin^2(\Omega T_{rf})}{\Omega^2} \tag{4.16}$$

where Ω is the beating frequency. During a full conversion of magnetron motion into cyclotron motion, the ion gains kinetic energy

$$\Delta E_r = \frac{m}{2}(\omega_+^2 - \omega_-^2)(\rho_{-,0}^2 - \rho_{+,0}^2) \tag{4.17}$$

where $\rho_{-,0}$ and $\rho_{+,0}$ are the magnetron and cyclotron amplitudes before quadrupole excitation.

4.3.2 Precision mass measurement

Since the cyclotron frequency of an ion is dependent on its mass, determining this frequency enables the measurement of the mass. One way to determine this frequency is the time-of-flight technique [41]. In a first step, a dipole excitation at the magnetron frequency is employed to move all ions in the trap to a well-defined radius. A quadrupole excitation then converts the magnetron motion into cyclotron motion with the same radius if $\omega_{RF} = \omega_c$ for the ions stored in the trap. When the ions are extracted from the trap, their magnetic moments interact with the magnetic field gradient and they experience an axial force $\mathbf{F} = -\mu \cdot \nabla \mathbf{B}$ converting radial kinetic energy into axial kinetic energy. Since the ions whose cyclotron frequency ω_c is in resonance with the excitation frequency ω_{RF} gain radial energy during excitation, they will be accelerated relative to those off resonance. This can be detected by measuring the time of flight to a detector, which is given by

$$T(\omega_{RF}) = \int_0^{z_{det}} \sqrt{\frac{m}{2(E_0 - qU(z) - \mu(\omega_{RF})B(z)}} \mathrm{d}z \ , \tag{4.18}$$

where the integration is along the flight path of the ions from the trap center ($z = 0$) to the detector ($z = z_{det}$). By scanning through different quadrupole excitation frequencies ω_{RF}, a time-of-flight spectrum for the ion species in question can be obtained. For an example of a resonance spectrum obtained with the JYFLTRAP precision trap, see Fig. 4.7. The sideband minima are due to the Fourier transformation of the square pulse envelope of the quadrupole excitation.
Having thus determined the cyclotron frequency, it can be translated into the ion's mass by measuring the time-of-flight resonance spectrum for a reference ion of known mass:

$$m_{meas} = \frac{\omega_c^{ref}}{\omega_c^{meas}}(m_{ref} - m_e) + m_e \ . \tag{4.19}$$

ω_c^{ref}, ω_c^{meas} are the cyclotron frequencies of the reference ion and the measured ion, respectively, m_{ref}, m_e and m_{meas} the masses of the reference ion, the electron and the measured atom, respectively.

A more detailed description of the working principle of the Penning trap can be found in [42] and [43].

4.3.3 Cooling and isobaric purification

In order to decrease their motional amplitudes, the ions are cooled, which results in smaller orbits centered in the trap. In this manner, inhomogeneities of the magnetic field and anharmonicities of the electric quadrupole field will have less impact on the measurement. Cooling is done by inserting a buffer gas into the trap, which gives rise to a viscous drag force

$$\mathbf{F} = -\delta m \mathbf{v} \ . \tag{4.20}$$

The damping parameter δ describes the effect of the buffer gas. The ions lose energy through collisions with the gas atoms, leading to a damping of the axial and the cyclotron motion. However, this also causes the radius of the magnetron motion to increase, since the Lorentz force $F_L = q \cdot \mathbf{v} \times \mathbf{B}$ decreases (Fig. 4.8). Therefore, after some cooling time all ions will be lost as their magnetron radius increases until they hit the trap electrodes. However, as described above, by coupling the cyclotron and magnetron motions with a driving quadrupole field at $\omega_+ + \omega_-$, the unstable magnetron motion can be converted into cyclotron motion, which in turn is cooled away, as it is stable. Since the reduced cyclotron frequency is typically about three orders of magnitude larger than the magnetron frequency, the cyclotron motion is cooled away faster than the magnetron radius expands, leading to a centering of the ions, Fig 4.9. Since, unlike the magnetron frequency, the cyclotron frequency $\omega_c = \omega_+ + \omega_-$ is mass dependent, this centering is mass selective. When the trap is opened, only

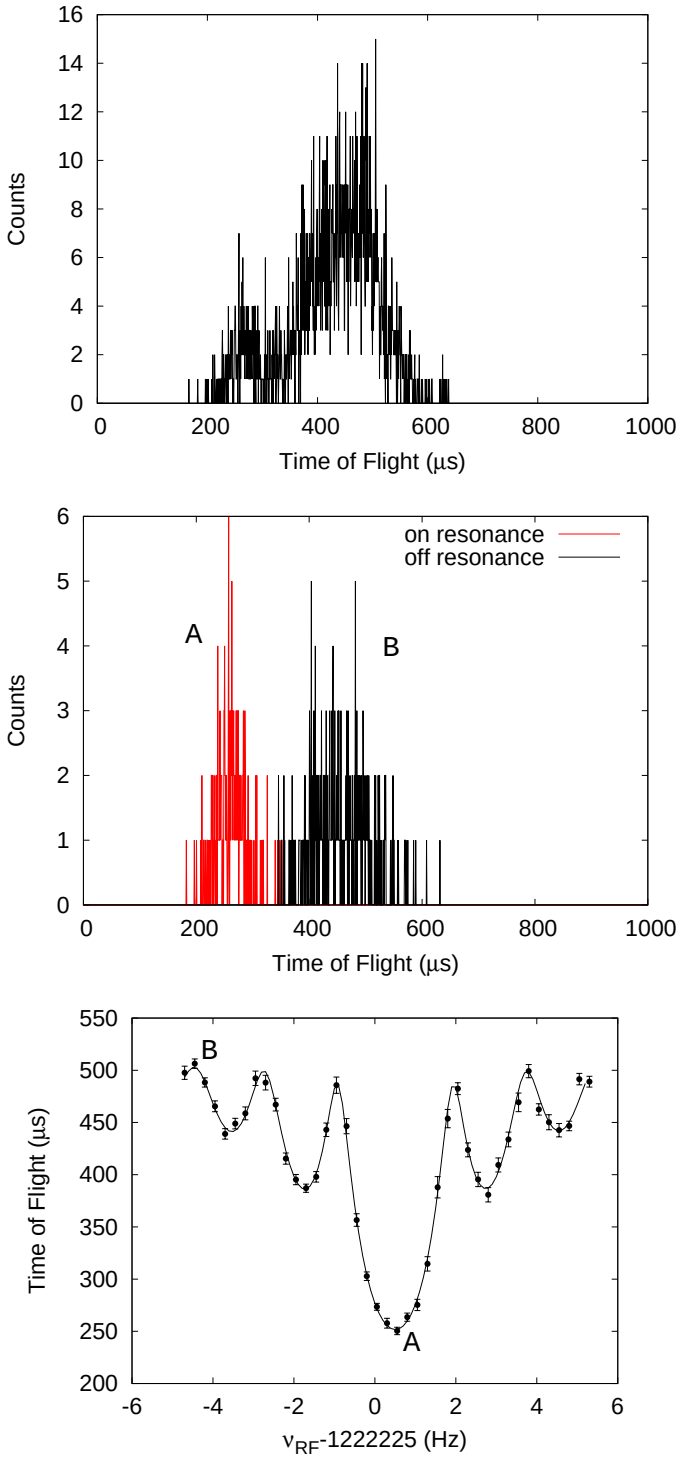

Figure 4.7: Time-of-Flight spectrum from a measurement of $^{88}Rb^{+}$ with 600 ms excitation time. The top figure shows all recorded ions versus their detection times. In the middle, only ions on resonance and off resonance are marked separately. The bottom panel shows the resulting resonance spectrum. The corresponding regions in the two lower panels are marked 'A' and 'B', respectively.

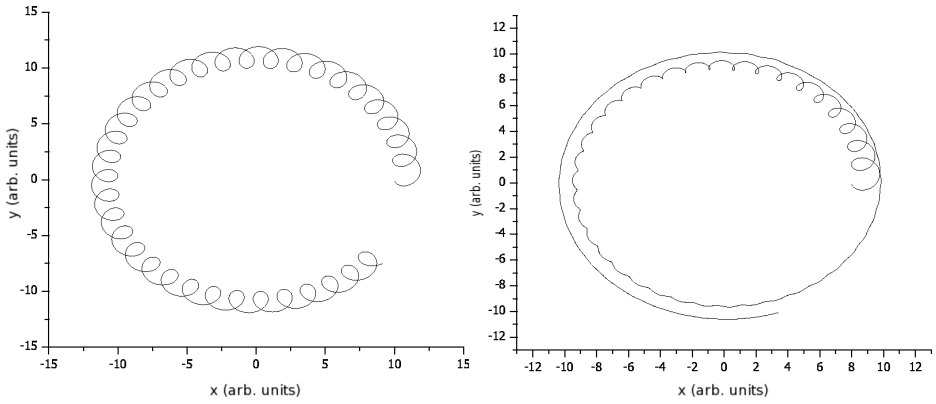

Figure 4.8: Motion of ions in the trap without (left) and with (right) buffer gas. The magnetron motion has a larger radius than the cyclotron motion and is centred around the centre of the electric field. The reduced cyclotron motion is centred around the magnetic field lines.

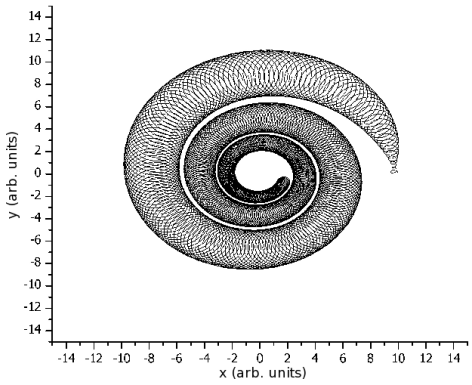

Figure 4.9: Motion of ions in the trap with buffer gas and ω_c-excitation

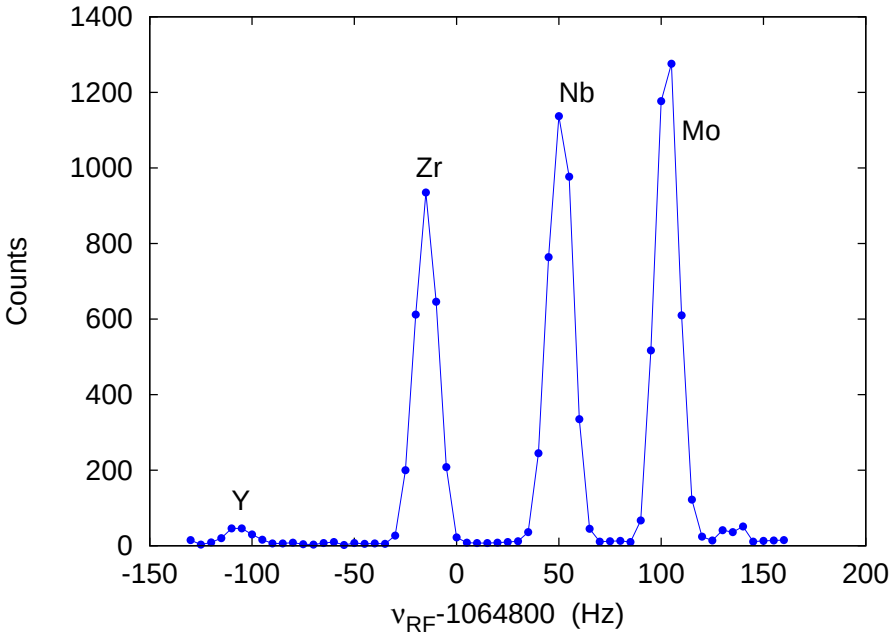

Figure 4.10: Cooling resonance spectrum for $A = 101$ isobars produced in fission reactions

those centred ions will be ejected. An example of a cooling resonance spectrum from the JYFLTRAP purification trap is shown in Fig. 4.10.

Inserting buffer gas into the Penning trap reduces the possible storage time of the ions. Charge exchange with impurities in the gas will neutralise the ions of interest. In addition, molecules can be formed. Therefore, noble gases with high ionisation energies are used. The collisions with the gas atoms also change the ions' orbit, and thus the frequency as they will be in a different field region. This reduces the mass resolving power of the trap. To achieve cooling, the buffer gas atoms have to be lighter than the ions to be cooled, or the distortions of the ions' path will be too great for any net cooling effect. The method of buffer gas cooling in Penning traps was first described in [44].

4.3.4 Decay spectroscopy with pure samples

A common problem in decay spectroscopy is the high background; the ion species of interest makes up only a small fraction of the sample, especially as one moves away from stability. If the daughter nucleus is radioactive, its decay will contribute to the background as well. A solution to this problem is to use a Penning trap for isobaric or even isomeric purification to produce a pure sample. If the sample is initially pure, even a daughter nucleus of similar half-life as the parent can be accounted for, as it is possible to fit a decay curve with two decay parameters if the composition of the initial sample, i.e. the pure sample after the trap, is known. However, the background due to the decay of the daughter nucleus will increase over time as more and more activity is accumulated and decays back to stability. Tape stations are therefore regularly used in decay spectroscopy, where the ions are implanted on a movable tape and, after some measurement time, can be transported away from the detectors. This was done at JYFLTRAP to study the decay of several neutron-rich even zirconium isotopes [9]. A problem in using this technique is the usually small transmission efficiency of Penning traps compared to the large statistics needed for decay spectroscopy.

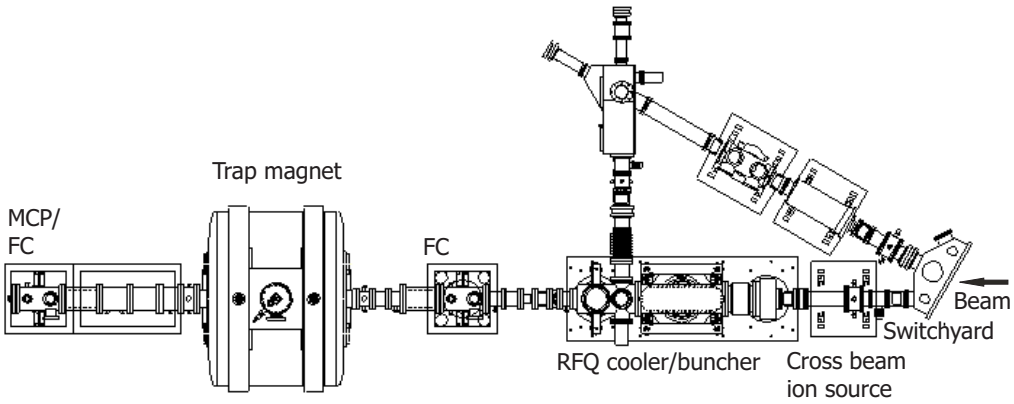

Figure 4.11: The JYFLTRAP setup

4.3.5 JYFLTRAP

The JYFLTRAP triple trap setup consists of a linear Paul trap to cool and bunch the beam and a double Penning trap system for isobaric purification and precision mass measurement. The layout is shown in Fig. 4.11 and will be discussed briefly in the following.

RFQ cooler/buncher

The beam from IGISOL has an emittance of about 13 π-mm-mrad and an energy spread of less than 100 eV. In order to improve the overall beam quality, a RFQ cooler/buncher is located after the bending magnet and the electrostatic beam switchyard. The potential in the cooler and the cooling/bunching principle are depicted in Fig. 4.12. The net effect of this treatment is a reduced transverse emittance of $\sim$ 3 π-mm-mrad at 38 keV and a decreased energy spread of $\sim$ 1 eV of the beam. Also, the initially continuous beam can be bunched by collecting ions in the cooler for a certain time and releasing them in bunches. The cooling process is independent of the chemical properties of the ions, only the radio frequency has to be adjusted depending on the mass of the ions. The pressure in the cooler is typically of the order of 10^{-2} mbar. The RFQ cooler/buncher is described in detail in [45].

The double Penning trap setup

The Penning trap at the IGISOL facility consists of two cylindrical Penning traps housed in the warm bore of a superconducting 7 T magnet. The magnet has two homogeneous field regions of 1 cm^3 each. The electrode configuration of the first trap is shown in Fig. 4.13; the configuration of the second trap is identical except for the diaphragm. Placing both traps in the same magnet avoids the problem of having to transport the ions through strong magnetic field gradients between the traps. The disadvantage, however, is that no pumping is possible between the traps, and the pressure especially in the precision trap is harder to control. The whole trap is kept on a high voltage (HV) platform to decelerate the incoming beam, the HV usually being 30 kV. A description of the technical details of the IGISOL Penning trap is given in [46].

The buffer gas for the first trap is fed directly into the trap structure through a hole in one of the electrodes. The traps are separated by a 5 cm long diaphragm of 2 mm inner diameter. Vacuum pumps are placed at both ends of the magnet. Because of this setup, it is not possible to directly

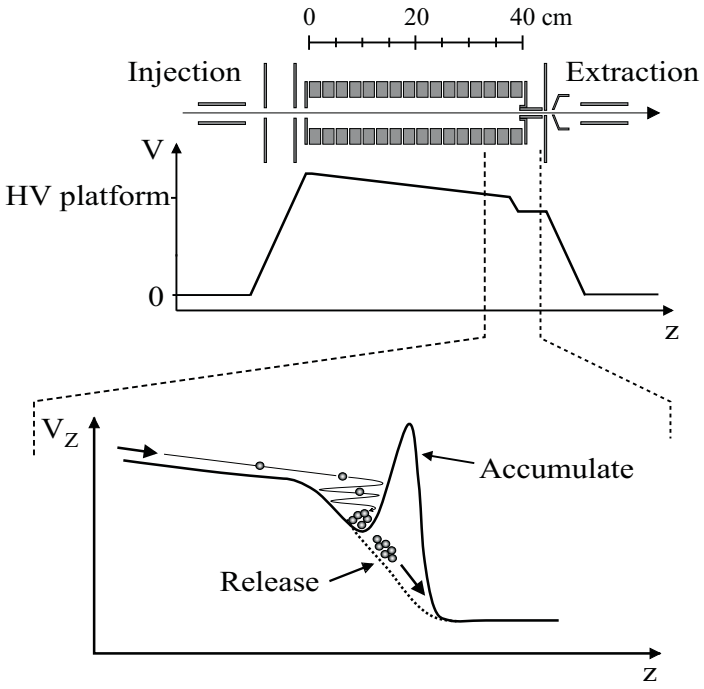

Figure 4.12: Sketch of the IGISOL RFQ cooler/buncher

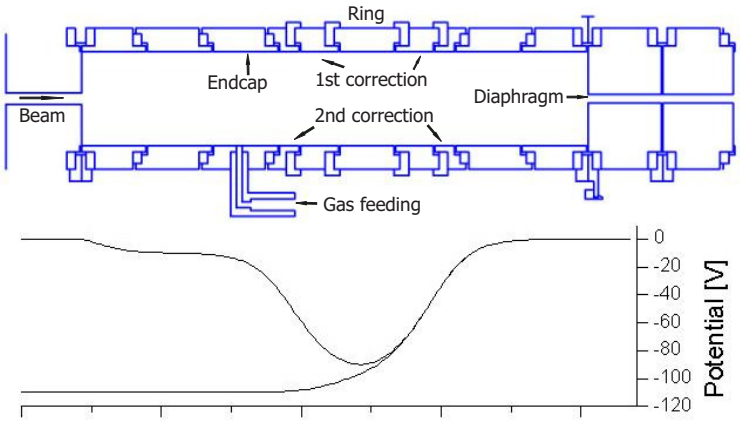

Figure 4.13: Electrode configuration of the JYFLTRAP purification trap

measure the pressure inside the traps, only in the gas feeding line. From the width of the cooling resonance spectra and the shape of the time-of-flight resonance spectrum the pressure can to some extent be deduced. The first trap contains helium buffer gas at a pressure of about 10^{-5}–10^{-4} mbar and is used for cooling and isobaric mass separation. The potential well has a depth of 100 V. The resulting magnetron frequency for these voltages is $\nu_- = 1700$ Hz. A mass resolving power of 145000 can be reached, which is sufficient for isobaric purification, as shown in Fig. 4.10. The second trap is operated in vacuum ($< 10^{-8}$ in the extraction line) for precision mass measurements. The depth of the capturing potential is 10 V.

4.3.6 ISOLTRAP

The ISOLTRAP setup is the pioneer Penning trap experiment from which JYFLTRAP and other experiments were derived. It consists of the same basic elements as the JYFLTRAP setup, namely a RFQ cooler/buncher, and two Penning traps, one for isobaric purification and one for precision measurements. These are aligned vertically due to space constraints in the experimental hall. Contrary to the JYFLTRAP setup, the Penning traps are on ground voltage. The setup is shown in Fig. 4.14

The RFQ cooler/buncher

The RFQ cooler/buncher [47] is located on a 60 kV high-voltage platform, corresponding to the high voltage of the ISOLDE target. It is filled with helium buffer gas at a pressure of $\approx 5 \cdot 10^{-6}$ mbar outside the electrodes. After being extracted in bunches from the RFQ and the HV platform, the ions are decelerated by pulsing an electrode down from 60 kV to about 3 kV. The ions are then deflected vertically, towards the Penning traps. The need to pulse the ions' energy down before guiding them to the traps means that beam tuning through the traps can only be done with bunched ions rather than in continuous mode, which results in a difficult optimisation procedure and mass dependent tuning due to the mass dependent flight time to the pulsed drift tubes.

The Penning traps

The first of the two Penning traps [43] is a cylindrical Penning trap, similar to the ones employed at JYFLTRAP. It is housed in the warm bore of a 4.7 T magnet and is filled with helium buffer gas at a pressure of $\approx 2 \cdot 10^{-6}$mbar in the beam line. A typical purification cycle consists of 5–15 ms magnetron excitation at the magnetron frequency $\nu_- = 304$ Hz, followed by around 100 ms of quadrupole excitation. The depth of the trapping potential is 100 V, though the actual quadrupolar field has a depth of 10 V; the ions are cooled down to the quadrupole potential through collisions with the buffer gas.

The precision trap is housed in a separate 5.9 T magnet. While this complicates tuning further, as the ions have to be injected into a second magnetic field, it does enable differential pumping between the traps and thereby improved vacuum in the precision trap. Inside the trap, very good vacuum conditions with pressures of $< 10^{-8}$ mbar can be reached. The trap is a hyperbolical Penning trap, resulting in a better field definition compared to a cylindrical electrode structure. The magnet has shim coils at room temperature, allowing fine-tuning of the homogeneity of the field. The depth of the trap potential is 10 V, resulting in a magnetron frequency of $\nu_- = 1078$ Hz. The ring electrode itself is at -10 V, meaning that the ions with a typical energy of a few eV, do not have sufficient energy to be transferred to ground potential without additional acceleration.

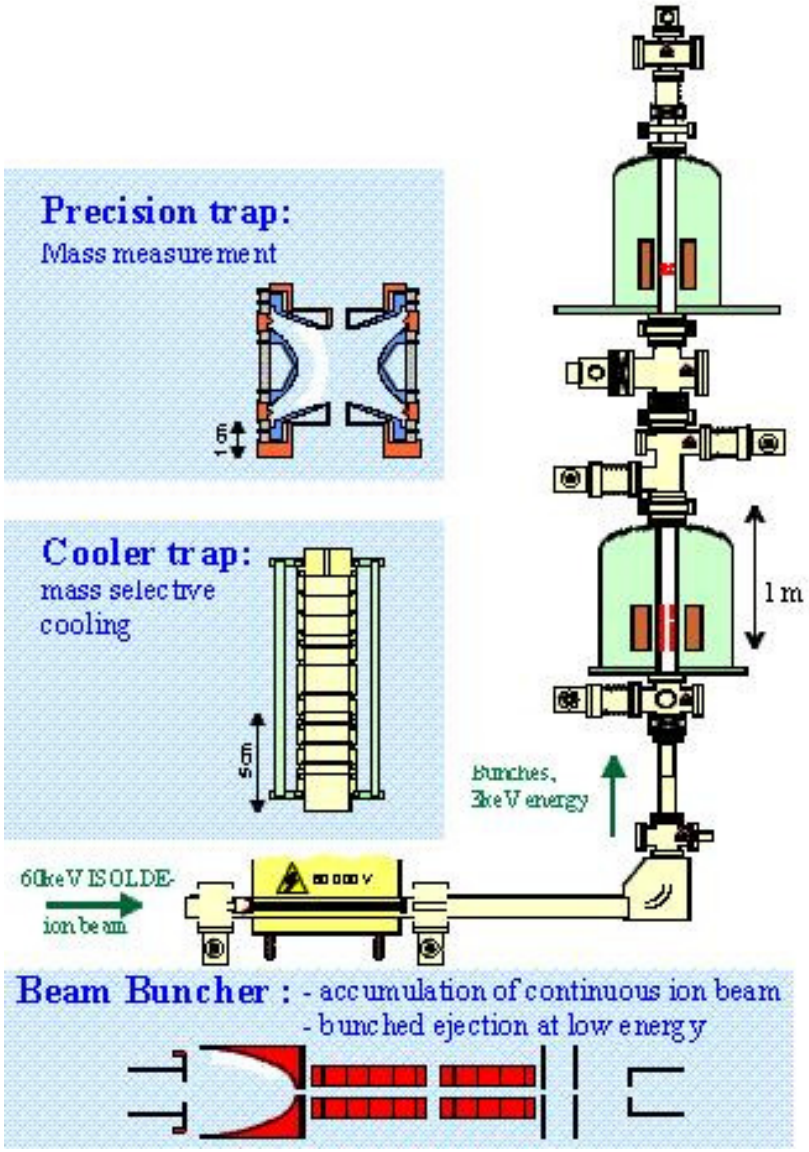

Figure 4.14: Sketch of the ISOLTRAP triple trap setup

5 Precision mass measurements at JYFLTRAP

5.1 Evaluation of the statistical uncertainties

A time-of-flight resonance spectrum is obtained by scanning through a range of frequencies and recording the time of the ions' detection by the MCP. For each measured frequency point the average time of flight is calculated as the mean of the distribution of all recorded ions. The deviation of the ion distribution is taken as the uncertainty of this average value. From the resulting resonance curves the cyclotron frequency of the examined species can be determined by fitting the theoretical line shape [41], using each point's time-of-flight uncertainty for weighting. The Levenberg-Marquardt fitting routine is used, adopted to fit the theoretical time-of-flight resonance shape. The fit yields the centre frequency, its uncertainty and the reduced χ^2. For $\chi^2 > 1$, the fit uncertainty is multiplied with the square root of the reduced χ^2.

To determine the mass of a nuclide the magnetic field in the trap has to be known. To this end, a time-of-flight resonance spectrum of a different nuclide of well-known mass has to be taken, so that the ratio of the two frequencies, and hence the ratio of the masses, can be obtained. For precise measurements it is important to determine the resonance frequency of the reference ion before and after the measurement of the nuclide of interest. In this manner, time-dependent fluctuations, e.g. of the magnetic field, can be averaged,

$$r = \frac{m_{meas} - m_e}{m_{ref} - m_e} = \frac{\nu_{ref}}{\nu_{meas}} = \frac{\frac{1}{2}(\nu_{ref,1} + \nu_{ref,2})}{\nu_{meas}} \tag{5.1}$$

for singly-charged ions. If the time between measurements and reference measurements varies, an interpolation rather than averaging is necessary.
In practice, this means that the examined species and the reference are usually measured alternatingly, starting and ending with the reference mass. This also means, however, that the frequency ratios derived from subsequent measurements are not independent, as they are calculated using a common reference measurement. This has to be considered when calculating the uncertainty of the average frequency ratio for one nuclide. The uncertainty of one individual frequency ratio as calculated in Eq. 5.1, is given by

$$\delta r = \sqrt{\left(\frac{\delta\nu_{ref,1}}{2\nu_{meas}}\right)^2 + \left(\frac{\delta\nu_{ref,2}}{2\nu_{meas}}\right)^2 + \left(\frac{\frac{1}{2}(\nu_{ref,1} + \nu_{ref,2})}{\nu_{meas}^2} \cdot \delta\nu_{meas}\right)^2}. \tag{5.2}$$

The weight of this one ratio when calculating the average of a set of measurements is then

$$w_i = \frac{1/(\delta r_i)^2}{\sum_i 1/(\delta r_i)^2} \tag{5.3}$$

and the average is given by

$$\overline{r} = \sum_i r_i \cdot w_i. \tag{5.4}$$

The uncertainty of the average of the frequency ratios of a set of N frequencies of the nuclide of interest and $N+1$ reference frequencies can now be calculated using the uncertainties of the determined frequencies.

$$\begin{aligned}\delta\overline{r} \;=\; & \left[\left(\frac{w_1}{2\nu_{meas,1}}\cdot\delta\nu_{ref,1}\right)^2\right. \\ & +\sum_{i=1}^{N-1}\left(\frac{w_i}{2\nu_{meas,i}}+\frac{w_{i+1}}{2\nu_{meas,i+1}}\right)^2\cdot\delta\nu_{ref,i+1}^2 \\ & \left.+\left(\frac{w_N}{2\nu_{meas,N}}\delta\nu_{ref,N+1}\right)^2+\sum_{i=1}^{N}\left(\frac{\nu_{ref,i}+\nu_{ref,i+1}}{2\nu_{meas,i}^2}w_i\cdot\delta\nu_{meas,i}\right)^2\right]^{1/2}\end{aligned} \tag{5.5}$$

A similar procedure is applied to Q_β measurements, where the mother and daughter nuclides are measured alternatingly, and the Q-value resulting from one measurement is given by

$$Q_i=\left(\frac{\frac{1}{2}(\nu_{daughter,i}+\nu_{daughter,i+1})}{\nu_{mother,i}}-1\right)(m_{daughter}-m_e) \tag{5.6}$$

The advantage of directly measuring the Q-value is that the uncertainty of the mass of the daughter nucleus, which serves as reference, scales with

$$\frac{\nu_{daughter}}{\nu_{mother}}-1$$

which is $\ll 1$, as the masses are very close.

5.2 Systematic uncertainties

In addition to the statistical uncertainty and the uncertainty of the mass of the reference ion, three sources of systematic errors have to be taken into account in the calculation of the final uncertainty: the count rate effect due to a high number of ions in the trap, the fluctuations of the magnetic field and electronics, and a mass-dependent uncertainty due to imperfections in the electric quadrupolar field.

5.2.1 Count rate

Large numbers of ions in the trap, especially of different species, can cause the observed resonance frequency to shift, as described in [48]. This shift is assumed to be caused by Coulomb interactions. If all ions in the trap have the same mass, no shift is expected. If different masses are introduced, the respective resonance frequencies are predicted to be lowered and shifted closer to each other. It is therefore important to keep the number of ions in the precision trap low, and to account for any remaining shifts in the analysis. Where sufficient statistics are available, a count rate class analysis is conducted as described in [49] and shown in Fig. 5.1. The available data set is split into groups depending on the number of detected ions. For each of these groups the resonance frequency is determined by fitting the theoretical line shape. A linear fitting routine is used to extrapolate the frequency to 0.6 ions in the trap, accounting for the 60% efficiency of the detector. Figure 5.1 shows two examples of count rate class analyses conducted this way. As can be seen, in the upper part the extrapolation seems quite reliable and the fitted frequencies line up nicely, though the resonance frequency increases with the count rate, rather than decrease as predicted in [48]. The lower plot, however, illustrates a problem regularly encountered in count rate class analyses at JYFLTRAP.

The scatter of the individual fitted frequencies is considerable, and, looking at the first two classes only, the slope might as well be negative. Indeed, in about 30% of all cases, the slope is found to be negative rather than positive as in Fig. 5.1. This behaviour might be explained by the gradient of the magnetic field in the precision trap. It has been observed that a larger axial amplitude leads to a higher frequency, i.e. the magnetic field increases in the axial direction, while larger radii lead to lower frequencies, i.e. the field decreases in the azimuthal direction. Rather than being caused by different ion species in the trap, the count rate effect might thus be caused by ions of the same species in different positions with different magnetic field strengths. The direction of the frequency shift thus depends on the shape of the ion cloud, which in turn depends on the conditions in the purification trap and on the transfer between the traps. Such a scenario would also explain why a count rate class effect is often observed even if only one stable ion species is present in the trap. This somewhat random behaviour is one reason why this analysis method is not always used. Another reason are low statistics. When the total number of ions collected for a resonance spectrum is too low to split into groups, the maximum number of detected ions per cycle is limited in the analysis, and the remaining systematic uncertainty is estimated based on the count rate class analysis of the spectra with sufficient statistics. The resulting uncertainty is quadratically added to the final averaged frequency ratio, as the effect is expected to cause an offset which will not average out with an increasing number of measurements.

5.2.2 Fluctuations

There are various reasons for the cyclotron frequency to fluctuate. One is the fluctuation of the magnetic field due to the variation of the temperature in the experimental hall. This effect is shown in Fig. 5.2. The frequency shift due to a change in temperature can be quite large, but, as can be seen in Fig. 5.2, the variation is slow, and this drift is accounted for by taking reference measurements before and after each measurement, and by keeping the acquisition time for one resonance spectrum below about one hour. However, the high-voltage cage in which the trap is located has been covered in thermoplastic foil, to try to reduce the fluctuations of the temperature. There are, however, also fluctuations on a shorter time scale, e.g. of power supplies. These residual fluctuations appear to be completely random. They are therefore expected to average out over the course of several measurements. The size of the fluctuations is estimated based on the behaviour of the reference frequencies with time, and the average offset between consecutive references. The resulting uncertainty in terms of a frequency shift is added to each determined cyclotron frequency, and hence the impact on the final value decreases with an increasing number of measurements.

5.2.3 Mass-dependent uncertainties

A misalignment of the magnetic and electric fields, or inhomogeneities in the electric quadrupole field, can cause the cyclotron frequency of one ion species to shift relative to that of another. The bigger the mass difference, the larger this shift. This effect was investigated by comparing the resonance frequencies of O_2 molecules and ^{132}Xe. The measured cyclotron frequencies were $\nu_c(\mathrm{O_2}) = (3358937.32 \pm 0.05)$ Hz and $\nu_c(^{132}\mathrm{Xe}) = (814609.991 \pm 0.018)$ Hz, leading to a mass ratio of $r_{exp} = \frac{\nu_c(^{132}\mathrm{Xe})}{\nu_c(\mathrm{O_2})} = 0.242520153(5)$. The tabulated value is $r_{\mathrm{AME}} = 0.242520137(2)$. The resulting mass dependent uncertainty is

$$\frac{r_{exp} - r_{\mathrm{AME}}}{r_{\mathrm{AME}}} = 7 \cdot 10^{-10} \cdot (A - A_{ref}) \ .$$

This value might, however, underestimate the actual effect for lower masses. The frequency shift is accounted for by multiplying this uncertainty by the difference in mass number between the reference and the measured nuclide and quadratically adding it to the uncertainty of the final average

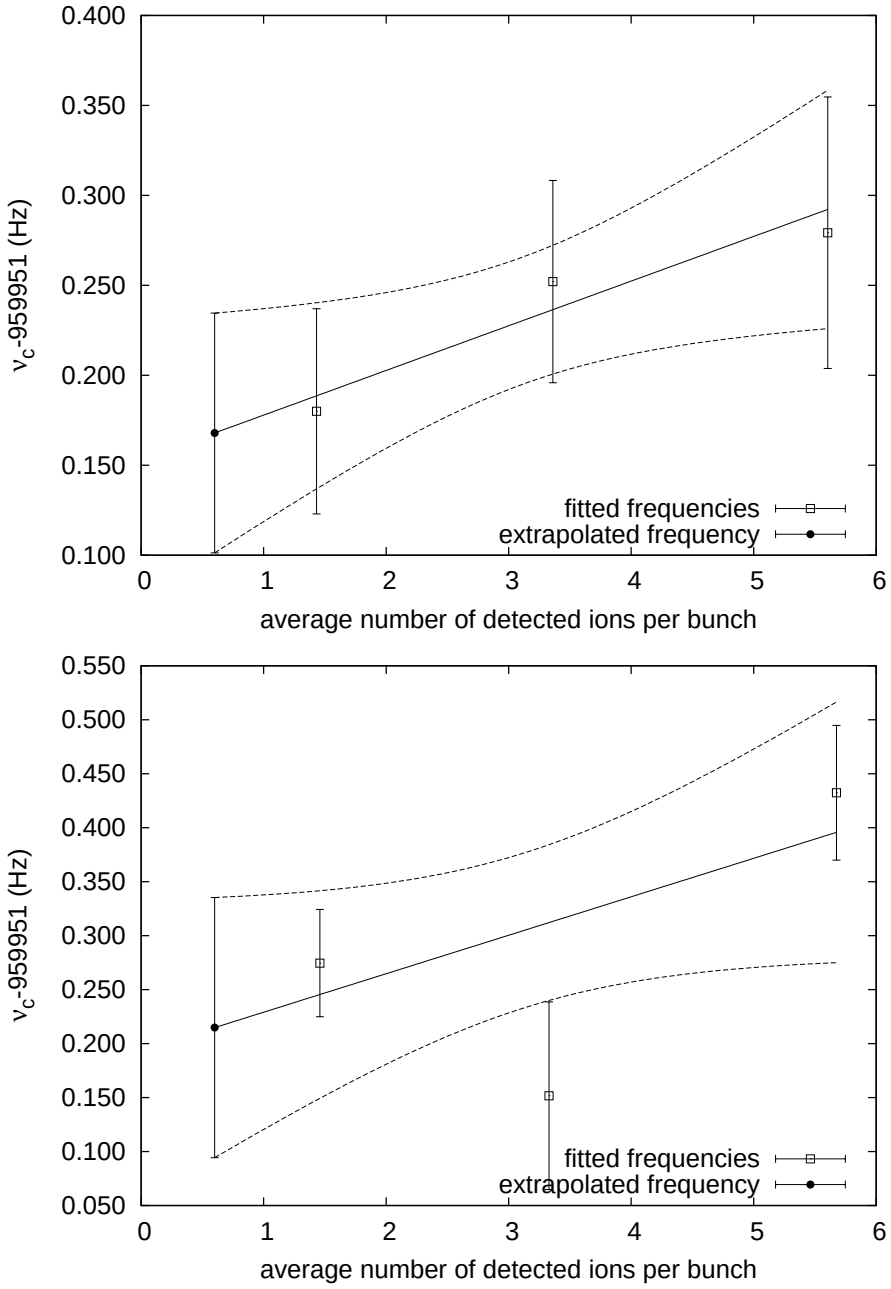

Figure 5.1: Two examples of count rate class analyses for ^{112}Tc. The extrapolated value is at 0.6 ions in the trap, corresponding to a 60% detection efficiency of the MCP.

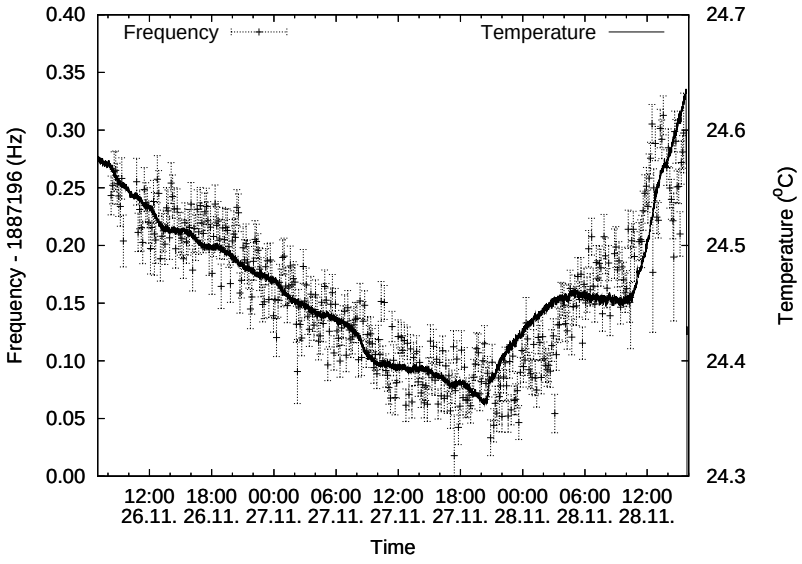

Figure 5.2: Fluctuation of temperature and cyclotron frequency of ^{57}Fe.

frequency ratio.

5.3 Results

The work presented here was conducted using the IGISOL fission ion guide, with a cyclotron beam of 25–30 MeV protons at an intensity of 5–10 μA. Most of the data in this work has been previously published, [6, 20, 21, 27], and details of the analysis can be found in those references. In addition, previously unpublished measurements of $^{102-110}$Mo and $^{100-105}$Zr, done in June 2005, were included. The systematic uncertainties of these measurements, as discussed above, are 0.04 Hz for both the count rate effect and the fluctuations. The number of measurements and the excitation times are given in table 5.1. The reference was ^{97}Zr, as with the already published data for zirconium and molybdenum [6], and it was therefore possible to obtain an average frequency ratio and an average mass excess. The obtained frequency ratios $\frac{\nu_{c,ref}}{\nu_{c,meas}}$ and mass excess values are given in table 5.2.

Table 5.1: Overview of the nuclides studied in June 2005. Given are the number N of resonance spectra taken, excitation time, the half-life, spin, and parity as listed in the AME03 [28]. '#' denotes estimated values, and '()' uncertain spin and/or parity.

Nucleus	N	T_{RF} [ms]	$T_{1/2}$	I^{π}
^{100}Zr	4	800	7.1 s	0^+
^{101}Zr	4	800	2.3 s	$3/2^+$
^{102}Zr	4	800	2.9 s	0^+
^{103}Zr	4	800	1.3 s	$(5/2^-)$
^{104}Zr	4	400	1.2 s	0^+
^{105}Zr	4	400	600 ms	
^{102}Mo	4	800	11.3 min	0^+
^{103}Mo	4	800	67.5 s	$(3/2^+)$
^{104}Mo	4	800	60 s	0^+
^{105}Mo	4	800	35.6 s	$(5/2^-)$
^{106}Mo	4	800	8.73 s	0^+
^{107}Mo	4	800	3.5 s	$(7/2^-)$
^{108}Mo	4	400	1.09 s	0^+
^{109}Mo	4	400	530 ms	$7/2^-$#
^{110}Mo	5	200	300 ms	0^+

Table 5.2: Obtained frequency ratios x for the singly charged positive ions relative to the reference mass, and resulting mass excess values ME in keV.

Isotope	Reference	$\frac{\nu_c^{ref}}{\nu_c^{meas}}$	ME (JYFL) [keV]	ME (AME03) [keV]	Diff
^{85}Br	^{88}Rb	0.965237440(37)	−78575.4 ± 3.5	−78610 ± 19	−34.6
^{86}Br	^{88}Rb	0.977334856(38)	−75632.3 ± 3.5	−75640 ± 11	−7.7
^{87}Br	^{88}Rb	0.988731283(39)	−73892 ± 4	−73857 ± 18	35
^{88}Br	^{88}Rb	1.000145235(39)	−70716 ± 4	−70730 ± 40	−14
^{89}Br	^{88}Rb	1.011550223(40)	−68275 ± 4	−68570 ± 60	−295
^{90}Br	^{88}Rb	1.022977586(41)	−64001 ± 4	−64620 ± 80	−619
^{91}Br	^{88}Rb	1.034388086(43)	−61108 ± 4	−61510 ± 70	−402
^{92}Br	^{88}Rb	1.045822783(82)	−56233 ± 7	−56580 ± 50	−347
^{94}Rb	^{88}Rb	1.068422547(45)	−68564 ± 5	−68553 ± 8	11
^{95}Rb	^{88}Rb	1.079829822(38)	−65935 ± 4	−65854 ± 21	81
^{96}Rb	^{88}Rb	1.091260919(41)	−61355 ± 4	−61225 ± 29	130
^{97}Rb	^{88}Rb	1.102670725(65)	−58519 ± 6	−58360 ± 30	159
^{95}Sr	^{97}Zr	0.979449067(132)	−75121 ± 13	−75117 ± 7	5
^{96}Sr	^{97}Zr	0.989792213(134)	−72924 ± 13	−72939 ± 27	−15
^{97}Sr	^{97}Zr	1.000159088(133)	−68586 ± 13	−68788 ± 19	−203
^{98}Sr	^{97}Zr	1.010501790(136)	−66429 ± 13	−66646 ± 26	−217
^{99}Sr	^{97}Zr	1.020863862(70)	−62523 ± 7	−62186 ± 80	338
^{100}Sr	^{97}Zr	1.031212498(86)	−59831 ± 9	−60220 ± 130	−389
^{95}Y	^{97}Zr	0.979381343(69)	−81235 ± 7	−81207 ± 7	28
^{96}Y	^{97}Zr	0.989732208(70)	−78341 ± 7	−78347 ± 23	−6
^{96}Y^m	^{97}Zr	0.989749280(69)	−76800 ± 7	−77206 ± 21	−406
^{97}Y			−76125 ± 8	−76258 ± 12	−133
^{97}Y^m	^{97}Zr	1.000082958(74)	−75458 ± 8	−75590 ± 12	−132
^{98}Y	^{97}Zr	1.010436763(88)	−72299 ± 12	−72467 ± 25	−168
^{99}Y	^{97}Zr	1.020773794(73)	−70654 ± 8	−70201 ± 24	453
^{100}Y	^{97}Zr	1.031129407(121)	−67332 ± 12	−67290 ± 80	42
^{100}Y^m	^{97}Zr	1.031131010(125)	−67187 ± 12	−67090 ± 220	97
^{101}Y	^{97}Zr	1.041473324(78)	−65065 ± 8	−64910 ± 100	155
^{98}Zr	^{97}Zr	1.010337145(135)	−81292 ± 13	−81287 ± 20	5
^{99}Zr	^{97}Zr	1.020696482(138)	−77633 ± 13	−77768 ± 20	−135
^{100}Zr	^{97}Zr	1.031029154(56)	−76381 ± 6	−76604 ± 36	−223
^{101}Zr	^{97}Zr	1.041383548(57)	−73169 ± 6	−73457 ± 31	−288
^{102}Zr	^{97}Zr	1.051719824(58)	−71593 ± 6	−71742 ± 51	−150
^{103}Zr	^{97}Zr	1.062080443(59)	−67818 ± 6	−68372 ± 109	−554
^{104}Zr	^{97}Zr	1.072422363(60)	−65732 ± 6	−66341 ± 401	−609
^{105}Zr	^{97}Zr	1.082788496(67)	−61460 ± 7	−62364 ± 401	−904
^{100}Nb	^{100}Nb^m	0.999996640(83)	−79802 ± 20	−79939 ± 26	−137
^{100}Nb^m	^{97}Zr	1.030994733(22)	−79488 ± 10	−79471 ± 28	17
^{101}Nb	^{102}Ru	0.990294436(39)	−78883 ± 5	−78942 ± 19	−59
^{102}Nb	^{97}Zr	1.051667579(28)	−76309 ± 10	−76350 ± 40	−41
^{102}Nb^m	^{102}Nb	1.000000983(77)	−76216 ± 20	−76220 ± 50	−4
^{103}Nb	^{102}Ru	1.009961485(41)	−75020 ± 5	−75320 ± 70	−300
^{104}Nb	^{97}Zr	1.072354888(30)	−71823 ± 5	−72220 ± 100	−397
^{105}Nb	^{102}Ru	1.029641706(42)	−69907 ± 5	−70850 ± 100	−943
^{106}Nb	^{102}Ru	1.039493991(43)	−66195 ± 5	−67100 ± 200	−905
^{107}Nb	^{102}Ru	1.049333291(84)	−63715 ± 9	−64920 ± 400	−1205
^{102}Mo	^{97}Zr	1.051587093(57)	−83574 ± 6	−83557 ± 21	17

Isotope	Reference	$\frac{\nu_c^{ref}}{\nu_c^{meas}}$	ME (JYFL) [keV]	ME (AME03) [keV]	Diff
^{103}Mo	^{97}Zr	1.061934753(58)	−80970 ± 6	−80847 ± 61	123
^{104}Mo	^{97}Zr	1.072260324(59)	−80359 ± 6	−80329 ± 54	31
^{105}Mo	^{97}Zr	1.082612522(60)	−77345 ± 6	−77338 ± 71	8
^{106}Mo	^{97}Zr	1.092944645(61)	−76144 ± 6	−76255 ± 18	−111
^{107}Mo	^{97}Zr	1.103303130(62)	−72562 ± 7	−72943 ± 162	−381
^{108}Mo	^{97}Zr	1.113641805(65)	−70769 ± 7	−71303 ± 196	−534
^{109}Mo	^{97}Zr	1.124005948(71)	−66676 ± 7	−67245 ± 298	−569
^{110}Mo	^{97}Zr	1.134348347(82)	−64547 ± 8	−65456 ± 401	−909
^{106}Tc	^{102}Ru	1.039351332(46)	−79736 ± 5	−79775 ± 13	−39
^{107}Tc	^{105}Ru	1.019137991(80)	−78743 ± 9	−79100 ± 150	−357
^{108}Tc	^{105}Ru	1.028699157(81)	−75916 ± 9	−75950 ± 130	−34
^{109}Tc	^{105}Ru	1.038248172(90)	−74276 ± 10	−74540 ± 100	−264
^{110}Tc	^{105}Ru	1.047813645(87)	−71028 ± 9	−70960 ± 80	68
^{111}Tc	^{105}Ru	1.057366451(100)	−69018 ± 11	−69220 ± 110	−202
^{112}Tc	^{102}Ru	1.098383006(58)	−65250 ± 6	−66000 ± 120	−750
^{106}Ru	^{105}Ru	1.009528321(80)	−86310 ± 9	−86322 ± 8	−12
^{107}Ru	^{105}Ru	1.019085671(79)	−83856 ± 9	−83920 ± 120	−64
^{108}Ru	^{105}Ru	1.028619965(80)	−83655 ± 9	−83670 ± 120	−15
^{109}Ru	^{105}Ru	1.038182111(82)	−80732 ± 9	−80850 ± 70	−118
^{110}Ru	^{105}Ru	1.047721142(84)	−80067 ± 9	−79980 ± 50	87
^{111}Ru	^{105}Ru	1.057287033(88)	−76778 ± 10	−76670 ± 70	108
^{112}Ru	^{105}Ru	1.066831083(88)	−75624 ± 10	−75480 ± 70	144
^{113}Ru	^{105}Ru	1.076402249(119)	−71819 ± 12	−72200 ± 70	−381
^{114}Ru	^{105}Ru	1.085950928(126)	−70212 ± 13	−70530 ± 230	−318
^{115}Ru	^{120}Sn	0.958523298(62)	−66071 ± 8	−66430 ± 130	−359
^{108}Rh	^{120}Sn	0.899973318(61)	−84924 ± 8	−85020 ± 110	−96
^{108}Rh^m	^{120}Sn	0.899972299(88)	−85037 ± 10	−85080 ± 40	−43
^{109}Rh	^{120}Sn	0.908312639(60)	−85018 ± 7	−85011 ± 12	7
^{110}Rh	^{120}Sn	0.916673797(61)	−82674 ± 7	−82780 ± 50	−106
^{111}Rh	^{120}Sn	0.925017220(61)	−82311 ± 8	−82357 ± 30	−46
^{112}Rh	^{120}Sn	0.933381862(62)	−79577 ± 8	−79740 ± 50	−163
^{113}Rh	^{120}Sn	0.941729225(63)	−78774 ± 8	−78680 ± 50	94
^{114}Rh	^{120}Sn	0.950097168(65)	−75672 ± 8	−75630 ± 110	42
^{115}Rh	^{120}Sn	0.958450190(65)	−74236 ± 8	−74210 ± 80	26
^{116}Rh	^{120}Sn	0.966822543(69)	−70642 ± 8	−70740 ± 140	−98
^{117}Rh	^{120}Sn	0.975178272(79)	−68904 ± 9	−68950 ± 500	−46
^{118}Rh	^{120}Sn	0.983554346(213)	−64894 ± 24	−65140 ± 500	−246
^{112}Pd	^{120}Sn	0.933321426(62)	−86327 ± 8	−86336 ± 18	−9
^{113}Pd	^{120}Sn	0.941686037(62)	−83597 ± 8	−83690 ± 40	−93
^{114}Pd	^{120}Sn	0.950027102(62)	−83497 ± 8	−83497 ± 24	0
^{115}Pd	^{120}Sn	0.958394697(122)	−80434 ± 14	−80400 ± 60	34
^{115}Pd^m	^{120}Sn	0.958395480(121)	−80347 ± 14	−80310 ± 60	37
^{116}Pd	^{120}Sn	0.966740203(63)	−79838 ± 8	−79960 ± 60	−122
^{117}Pd	^{120}Sn	0.975110888(66)	−76430 ± 8	−76530 ± 60	−100
^{118}Pd	^{120}Sn	0.983460297(66)	−75398 ± 8	−75470 ± 210	−72
^{119}Pd	^{120}Sn	0.991836131(73)	−71415 ± 9	−71620 ± 300	−205
^{120}Pd	^{120}Sn	1.000186128(81)	−70317 ± 10	−70150 ± 120	167

Table 5.3: Previous measurements of strontium.

Isotope	Method	Result	Reference
^{95}Sr	β-endpoint	$Q_\beta = 6082 \pm 10$	Blönnigen(1984) [50]
^{95}Sr	β-endpoint	$Q_\beta = 6052 \pm 25$	Mach(1990) [51]
^{95}Sr	Penning trap	ME $= -75109 \pm 9$	Raimbault-Hartmann(2002) [52]
^{96}Sr	β-endpoint	$Q_\beta = 5332 \pm 30$	Peuser(1979) [53]
^{96}Sr	β-endpoint	$Q_\beta = 5413 \pm 22$	Decker(1980) [54]
^{96}Sr	β-endpoint	$Q_\beta = 5345 \pm 50$	Graefenstedt(1987) [55]
^{96}Sr	β-endpoint	$Q_\beta = 5354 \pm 40$	Mach(1990) [51]
^{97}Sr	β-endpoint	$Q_\beta = 7452 \pm 40$	Blönnigen(1984) [50]
^{97}Sr	β-endpoint	$Q_\beta = 7480 \pm 18$	Gross(1992) [56]
^{98}Sr	β-endpoint	$Q_\beta = 5821 \pm 10$	Blönnigen(1984) [50]
^{98}Sr	β-endpoint	$Q_\beta = 5815 \pm 40$	Graefenstedt(1987) [55]
^{99}Sr	β-endpoint	$Q_\beta = 8030 \pm 80$	Iafigliola(1984) [57]
^{99}Sr	β-endpoint	$Q_\beta = 8360 \pm 75$	Graefenstedt(1987) [55]
^{100}Sr	β-endpoint	$Q_\beta = 7520 \pm 140$	Iafigliola(1984) [57]
^{100}Sr	β-endpoint	$Q_\beta = 7075 \pm 100$	Graefenstedt(1987) [55]

5.4 Discussion

5.4.1 Comparison to previous data

The new mass values for the technetium, ruthenium, rhodium and palladium isotopes have been compared to previous measurements in [20], those of bromine and rubidium in [21], and niobium and yttrium in [27]. Such a comparison for the new strontium, zirconium and molybdenum masses is presented here.

Strontium

The previous measurements of the strontium isotopes are listed in Table 5.3, and depicted in Fig. 5.3 together with the new values. ^{95}Sr has been previously measured in two β-endpoint measurements, [50, 51]. If the mass of the daughter nucleus ^{95}Y is taken from this work, neither one agrees with our new value. However, the mass of ^{95}Sr has also been measured at ISOLTRAP [52] with a precision better than the value presented here. The new JYFLTRAP value agrees with the ISOLTRAP value.

The mass of ^{96}Sr has been measured by four different groups using β-endpoint measurements [53, 54, 55, 51]. Only the result by Decker et al. [54] agrees with the new value; this is also the measurement on which the AME03 value is based. All other results give to high a binding energy. This is also the case for the two previous measurements of ^{97}Sr [50, 56], and those of ^{98}Sr [50, 55], though the result by Graefenstedt et al. [55] almost agrees with the new value if the mass of the daughter nucleus ^{98}Y is taken from this work.

The two previous mass measurements of ^{99}Sr [57, 55] differ greatly, the AME03 value being based on the result by Iafigliola et al. [57] . Even though the resulting mass given in the AME03 differs from our value by almost 380 keV, using the mass of the daughter nucleus ^{99}Y given here reduces the discrepancy between our value and the β-endpoint result to about 100 keV. ^{100}Sr was measured by the same groups as ^{99}Sr, again with greatly differing results. In this case, the AME03 value is based on the measurements by Graefenstedt et al. [55]. Our value, however, confirms the result by Iafigliola et al. [57].

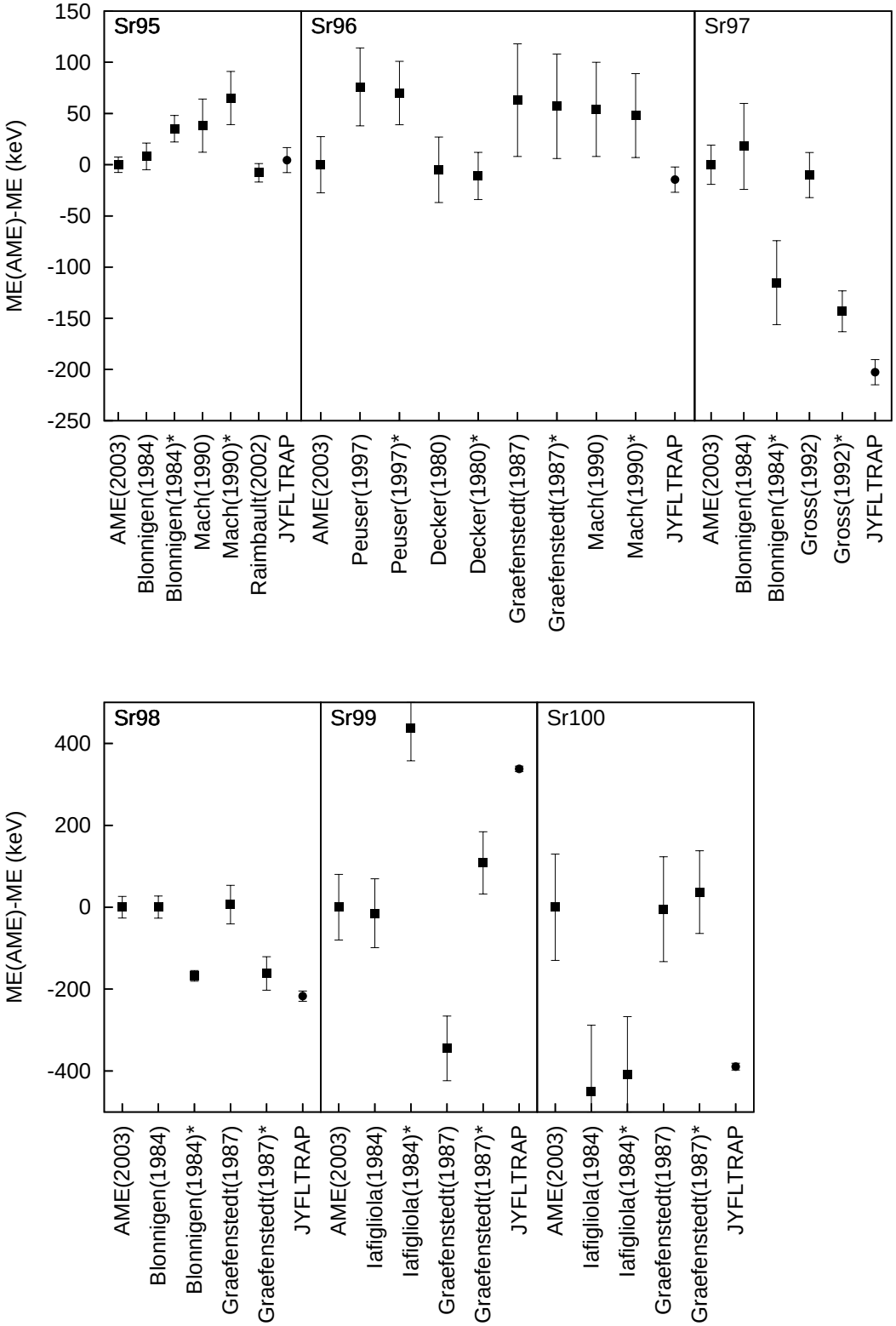

Figure 5.3: Strontium: Comparison between previous literature values and the values presented in this work. For the literature values that were given as a reaction or decay Q-value, the mass excess of the daughter is taken from the AME03, or, when marked with an asterisk (*), from this work.

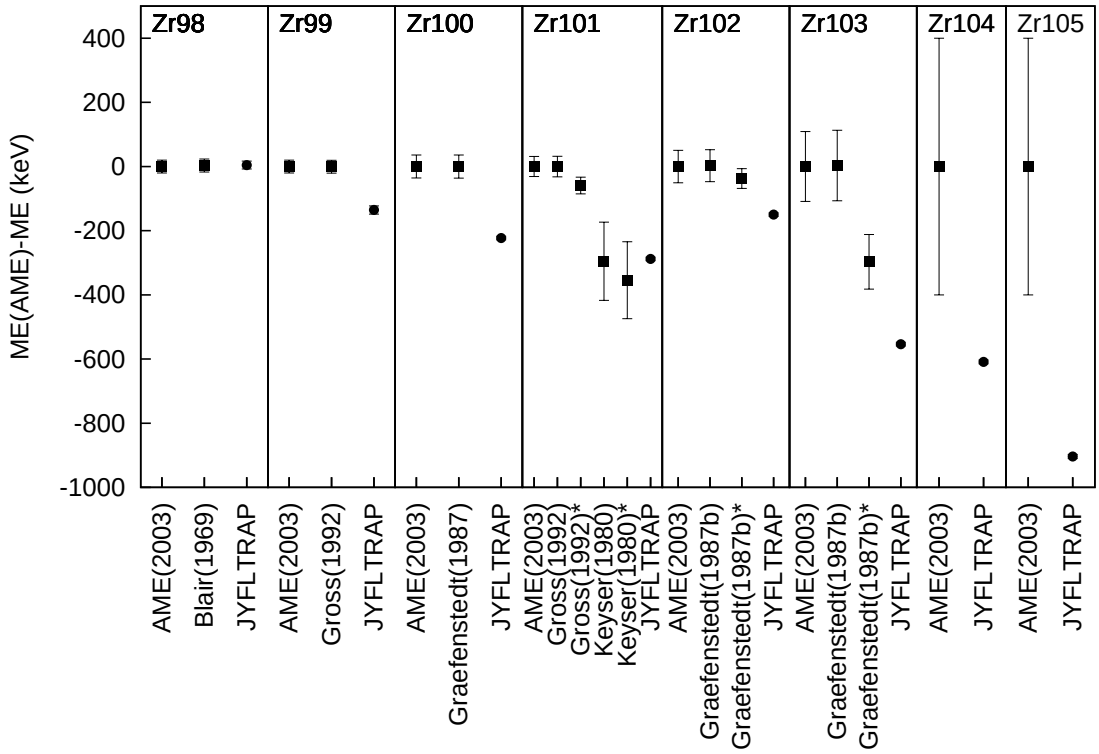

Figure 5.4: Zirconium: Comparison between previous literature values and the values presented in this work. For the literature values that were given as a reaction or decay Q-value, the mass excess of the daughter is taken from the AME03, or, when marked with an asterisk (*), from this work.

Zirconium

Fig. 5.4 shows the results of the previous measurement, which are listed in Table 5.4, and the new values, given in Table 5.2. The mass of ^{98}Zr has previously been measured by Blair et al. [58] in a (t, p) reaction. This results agrees very well with the value presented here. $^{99-103}$Zr were previously studied in β-endpoint measurements. ^{99,101}Zr were measured by Gross et al. [56], in both cases the AME03 value is based on those values. However, both results give too light a mass compared to our new value. The same is true for the results that Graefenstedt et al. obtained for ^{100,102,103}Zr [60, 55]. Again, for all three isotopes, the AME03 value is based on these measurements. ^{101}Zr was also studied by Keyser et al. [59], a measurement which agrees nicely with the value presented here. ^{104,105}Zr had not previously been measured, the masses given in the AME03 are based on extrapolations. Both masses are underestimated.

Molybdenum

For each isotope the previous measurements, given in Table 5.5, and the value measured at JYFLTRAP, as listed in Table 5.2, are compared in Fig. 5.5. The mass of ^{102}Mo has previously been measured both in a (t, p) reaction [61] and in a β-endpoint measurement [62]. Both results agree with each other and with our result. ^{103,104,105}Mo have all been studied by Graefenstedt et al. [60]. For ^{103}Mo their result gives too large a mass, for the other two isotopes, the masses agree with the results

Table 5.4: Previous measurements of zirconium.

Isotope	Method	Result	Reference
^{98}Zr	(t,p)	$Q_{(t,p)} = 3508 \pm 20$	Blair(1969) [58]
^{99}Zr	β-endpoint	$Q_\beta = 4559 \pm 15$	Gross(1992) [56]
^{100}Zr	β-endpoint	$Q_\beta = 3335 \pm 25$	Graefenstedt(1987) [55]
^{101}Zr	β-endpoint	$Q_\beta = 5780 \pm 120$	Keyser(1980) [59]
^{101}Zr	β-endpoint	$Q_\beta = 5485 \pm 25$	Gross(1992) [56]
^{102}Zr	β-endpoint	$Q_\beta = 4605 \pm 30$	Graefenstedt(1987) [55]
^{103}Zr	β-endpoint	$Q_\beta = 6945 \pm 85$	Graefenstedt(1987) [55]

Table 5.5: Previous measurements of molybdenum.

Isotope	Method	Result	Reference
^{102}Mo	(t,p)	$Q = 5034 \pm 20$	Casten(1972) [61]
^{102}Mo	β-endpoint	$Q_\beta = 3508 \pm 20$	Jokinen(1995) [62]
^{103}Mo	β-endpoint	$Q_\beta = 3750 \pm 60$	Graefenstedt(1987) [60]
^{104}Mo	β-endpoint	$Q_\beta = 2155 \pm 40$	Graefenstedt(1987) [60]
^{104}Mo	β-endpoint	$Q_\beta = 2155 \pm 40$	Jokinen(1995) [62]
^{105}Mo	β-endpoint	$Q_\beta = 4950 \pm 45$	Graefenstedt(1987) [60]
^{106}Mo	β-endpoint	$Q_\beta = 3510 \pm 45$	Graefenstedt(1987) [60]
^{106}Mo	β-endpoint	$Q_\beta = 3520 \pm 17$	Gross(1992) [63]
^{106}Mo	β-endpoint	$Q_\beta = 3520 \pm 17$	Jokinen(1995) [62]
^{107}Mo	β-endpoint	$Q_\beta = 6160 \pm 60$	Graefenstedt(1989) [64]
^{108}Mo	β-endpoint	$Q_\beta = 5135 \pm 60$	Gross(1992) [63]
^{108}Mo	β-endpoint	$Q_\beta = 5120 \pm 40$	Jokinen(1995) [62]
^{108}Mo	ESR	ME $= -70830 \pm 200$	Matoš(2004) [65]
^{109}Mo	ESR	ME $= -66650 \pm 230$	Matoš(2004) [65]
^{110}Mo	ESR	ME $= -64780 \pm 250$	Matoš(2004) [65]

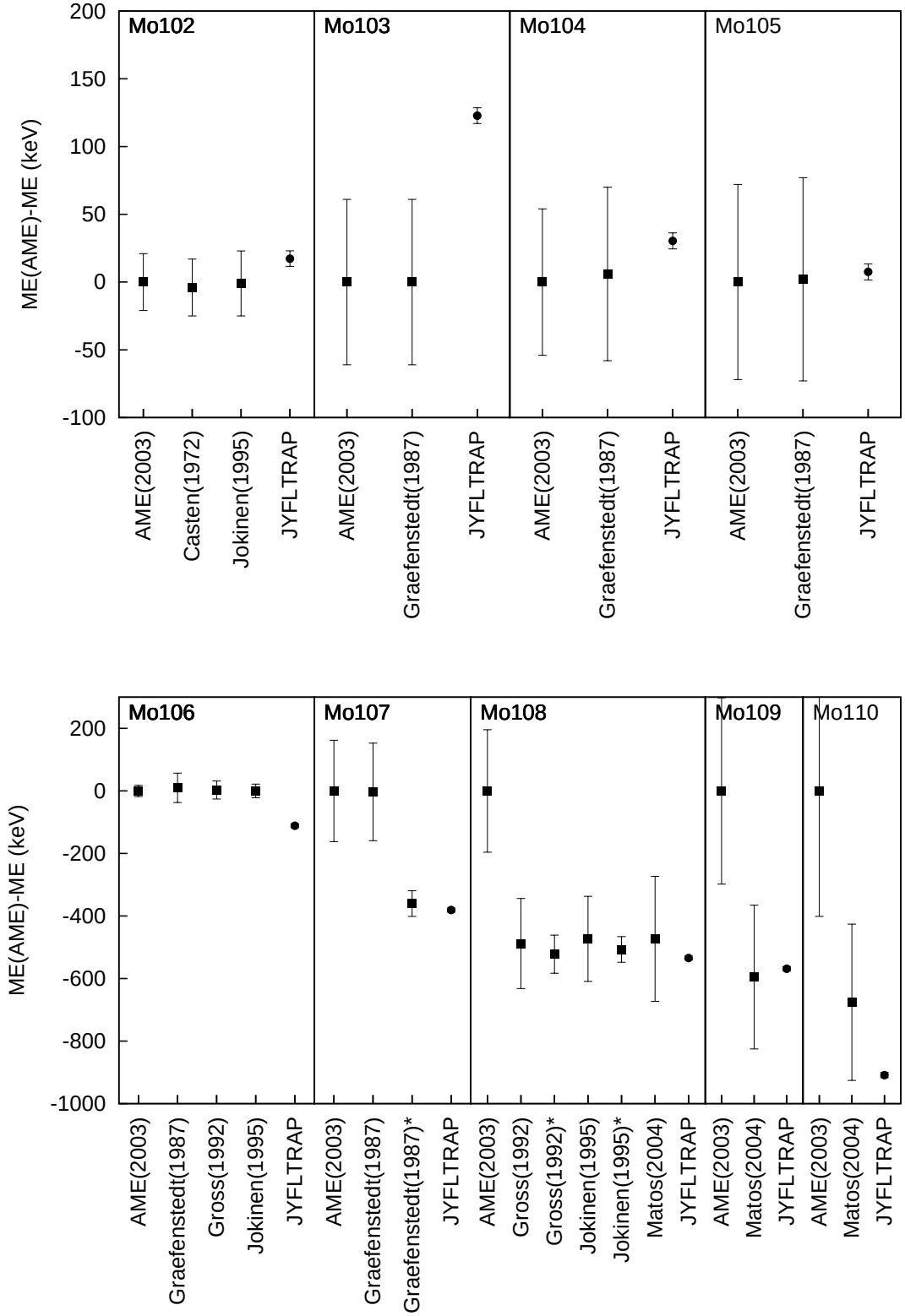

Figure 5.5: Molybdenum: Comparison between previous literature values and the values presented in this work. For the literature values that were given as a reaction or decay Q-value, the mass excess of the daughter is taken from the AME03, or, when marked with an asterisk (*), from this work.

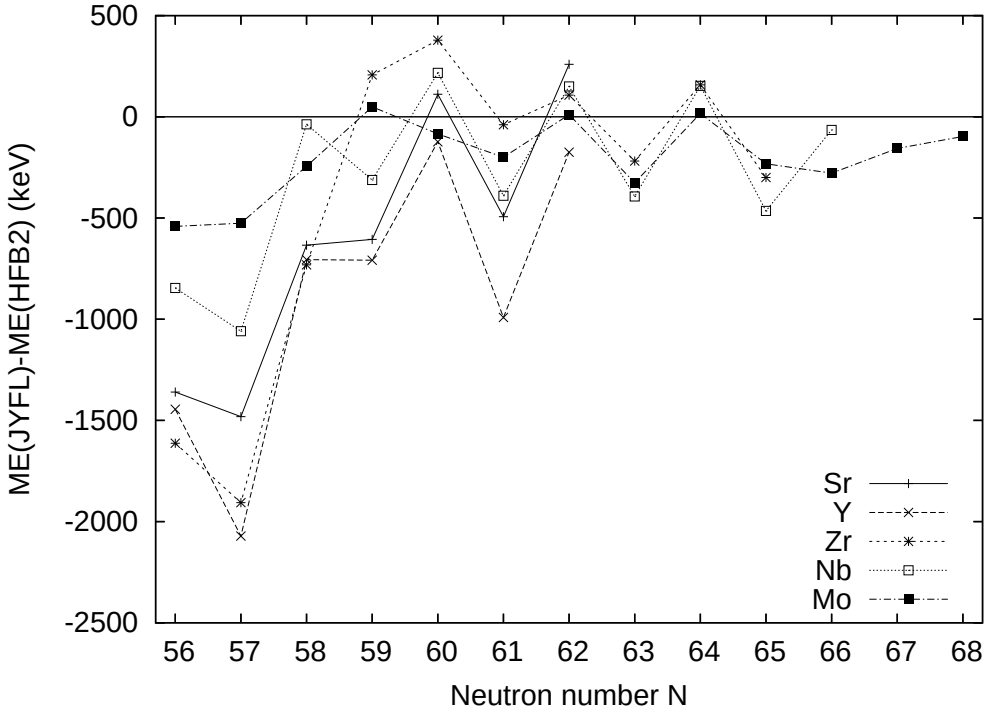

Figure 5.6: Comparison to the HFB2 model predictions.

presented here. ^{106}Mo, too, was measured by Graefenstedt et al., and also by Gross et al. [63] and Jokinen et al. [62], with all results agreeing with each other. However, our new value suggest the nuclide is less bound by about 110 keV.

Graefenstedt et al. also studied ^{107}Mo. If the mass of the daughter nucleus ^{107}Tc is taken from the AME03, the resulting mass value differs from our value by about 400 keV. If, however, the mass of ^{107}Tc is taken from this work, the corrected mass value agrees with our value. The mass value of ^{108}Mo given in the AME03 is based on extrapolation, which results in too small a mass by about 500 keV, even though the nuclide has previously been measured by Gross et al. [63] and Jokinen et al. [62]. Both these measurements yield mass values in agreement with our value. More recently, ^{108}Mo has been studied using the ESR storage ring at GSI in isochronous mode [65]. This measurement, too, agrees with ours. During the same ESR campaign the masses of ^{109,110}Mo were measured, with both results agreeing with the ones presented here. The AME03 mass values for both isotopes are based on extrapolations. As in the case of ^{108}Mo, these extrapolations overestimate the binding.

5.4.2 Comparison to global models

In [20, 21] the measured mass values of the isotopes of bromine, rubidium, technetium, ruthenium, rhodium and palladium have been compared to a selection of mass model predictions. The same is done here for the measured isotopes of strontium, yttrium, zirconium, niobium and molybdenum. Additional data is taken from the AME03 to extend the comparison for all elements to $N = 56$. They are compared to the HFB-2 (Fig. 5.6), and HFB-9 (Fig. 5.7), the HFBCS-1 (Fig. 5.8), the FRDM (Fig. 5.9), the ETFSI-1 (Fig. 5.10) and ETFSI-2 (Fig. 5.11), the two versions of the model by Duflo and Zuker (Figs. 5.12 and 5.13), and the KTUY mass formula (Fig. 5.14).

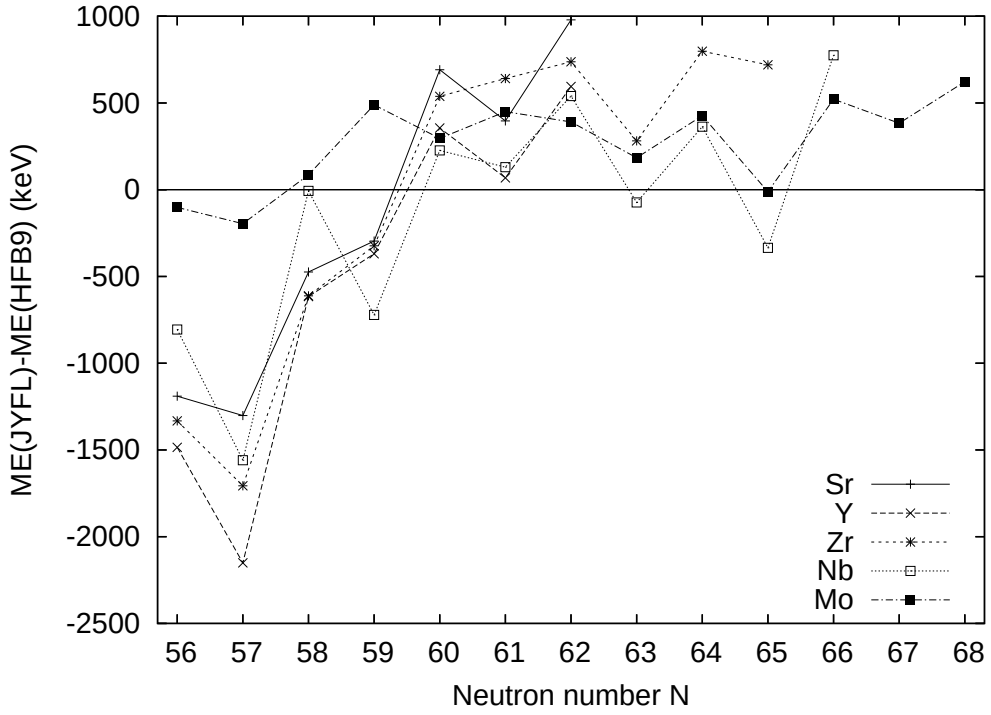

Figure 5.7: Comparison to the HFB9 model predictions.

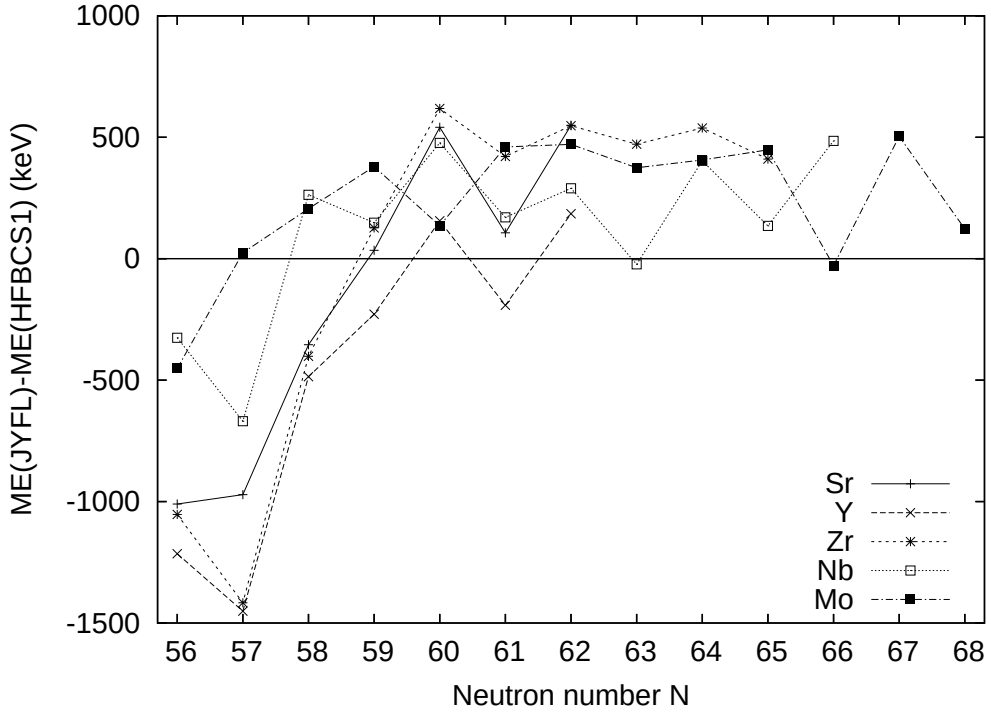

Figure 5.8: Comparison to the HFBCS-1 model predictions.

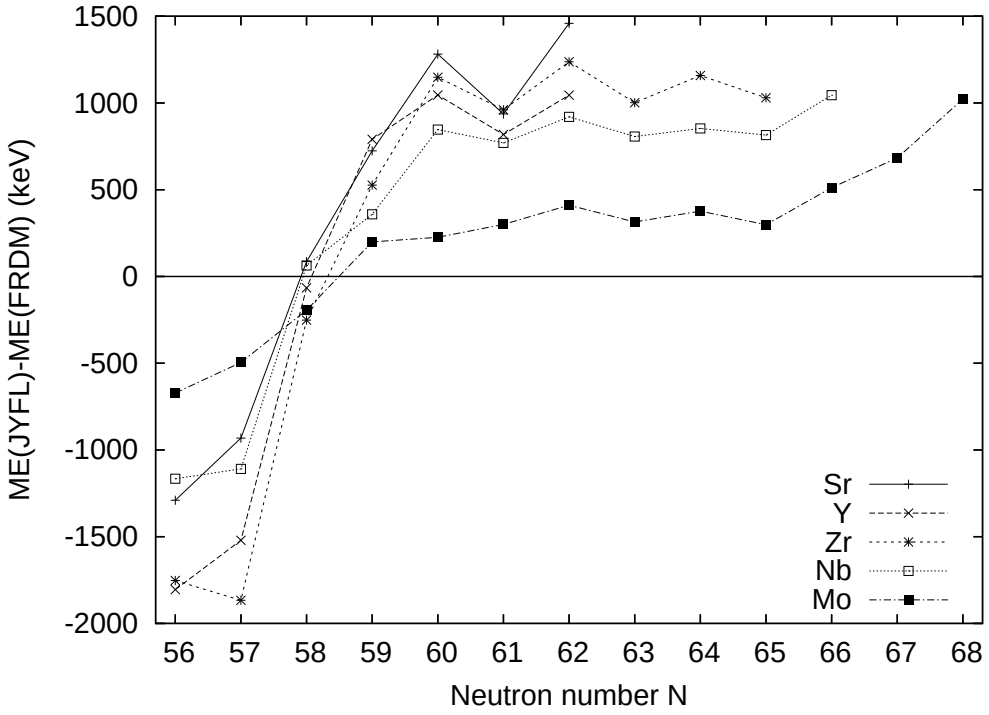

Figure 5.9: Comparison to the FRDM model predictions.

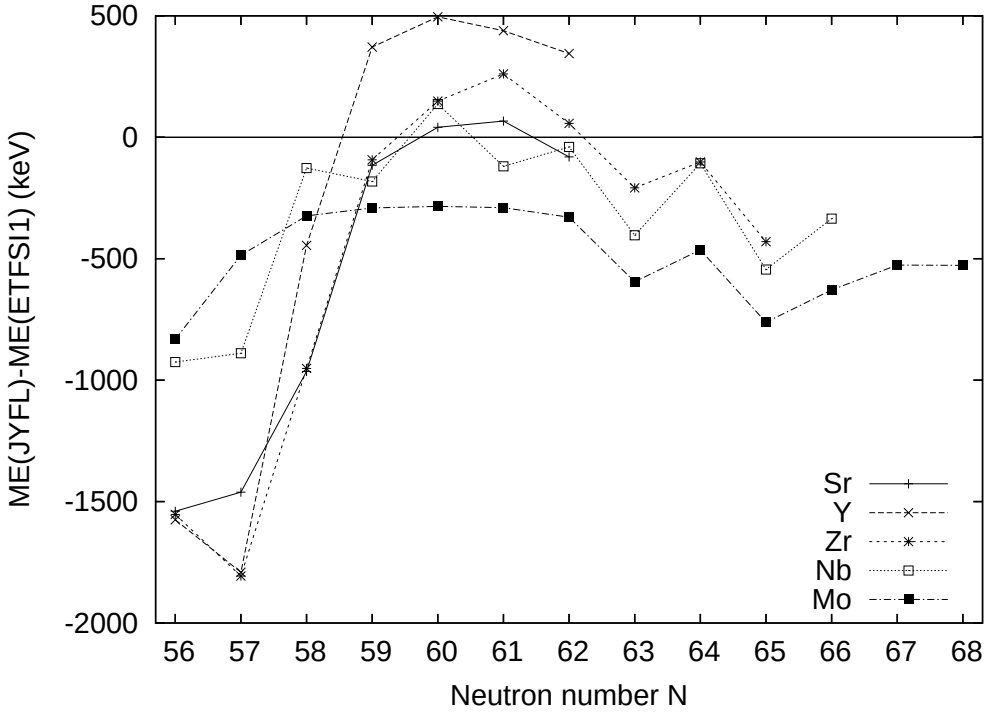

Figure 5.10: Comparison to the ETFSI-1 model predictions.

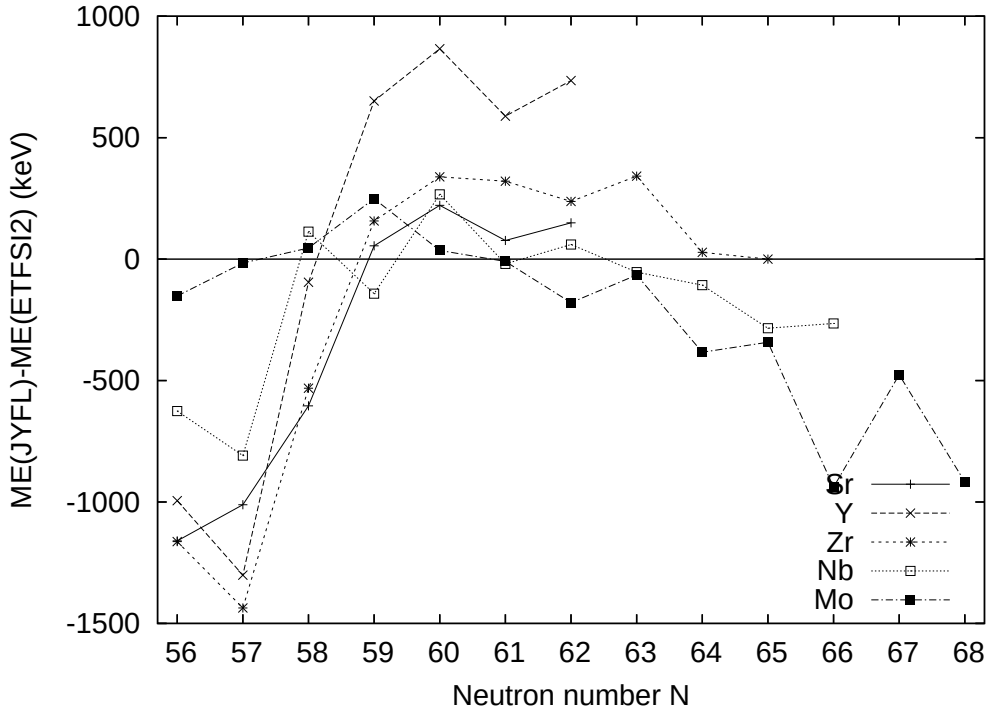

Figure 5.11: Comparison to the ETFSI-2 model predictions.

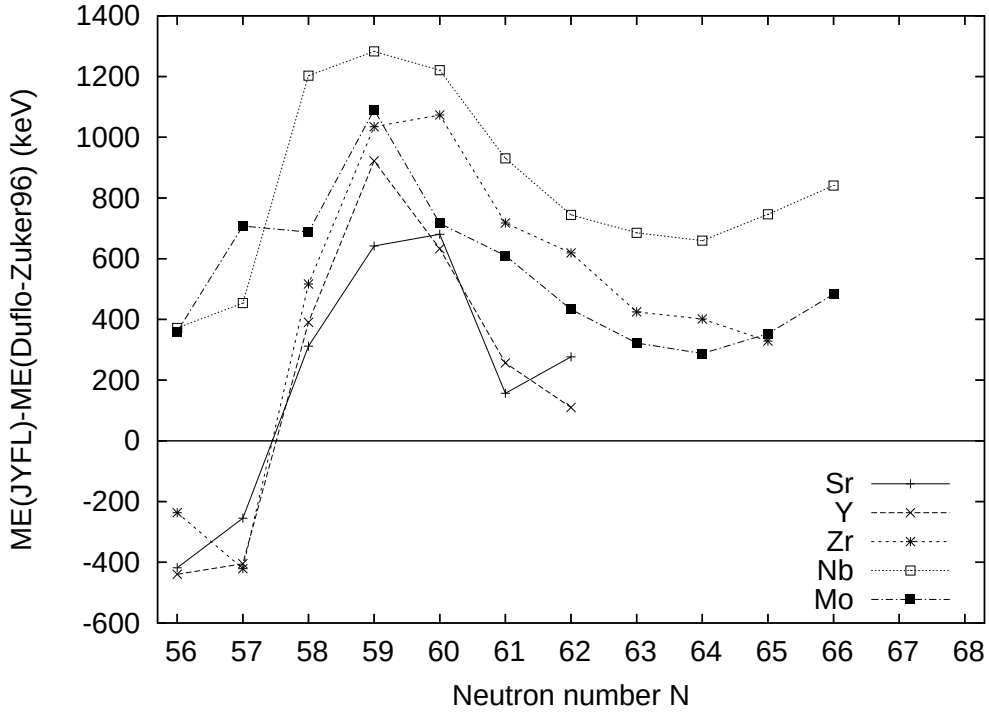

Figure 5.12: Comparison to the 10 parameter Duflo-Zuker model predictions.

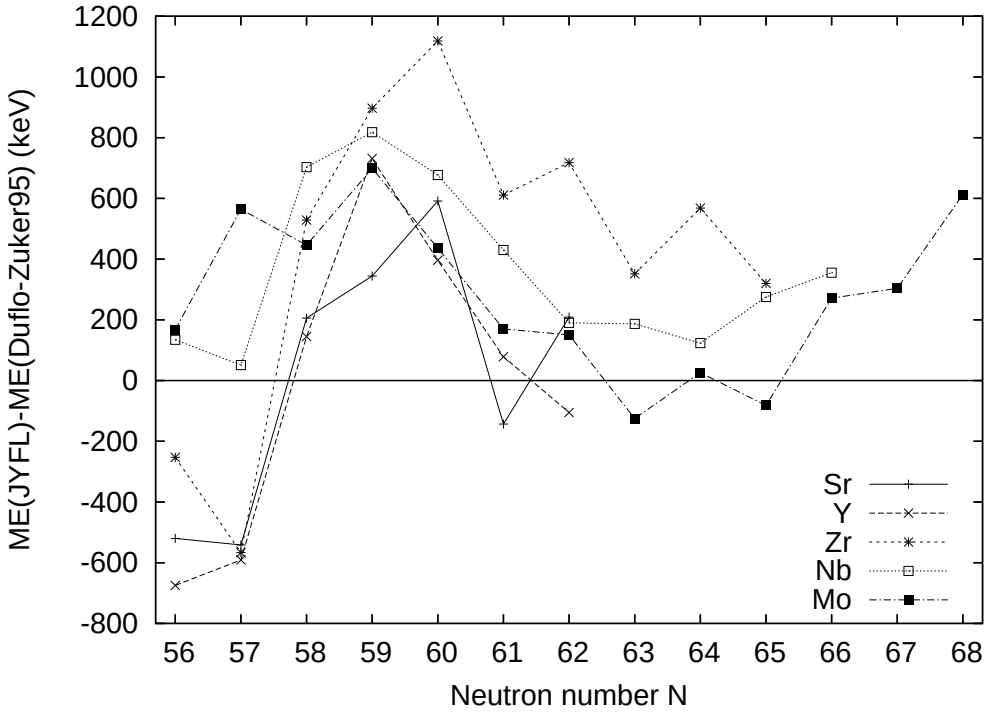

Figure 5.13: Comparison to the 28 parameter Duflo-Zuker model predictions.

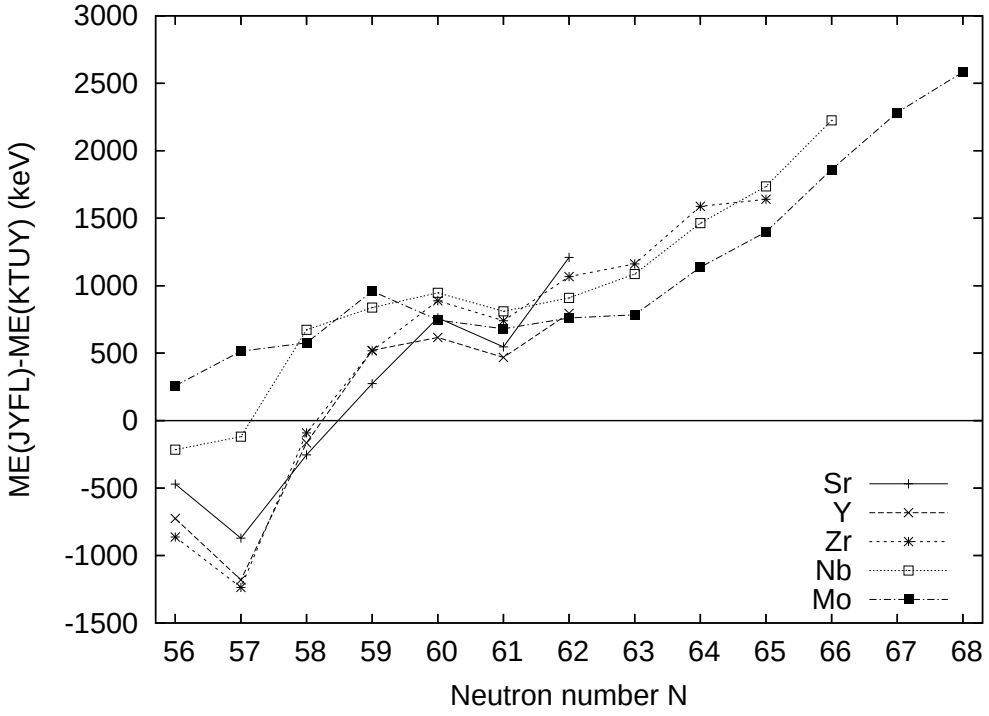

Figure 5.14: Comparison to the KTUY model predictions.

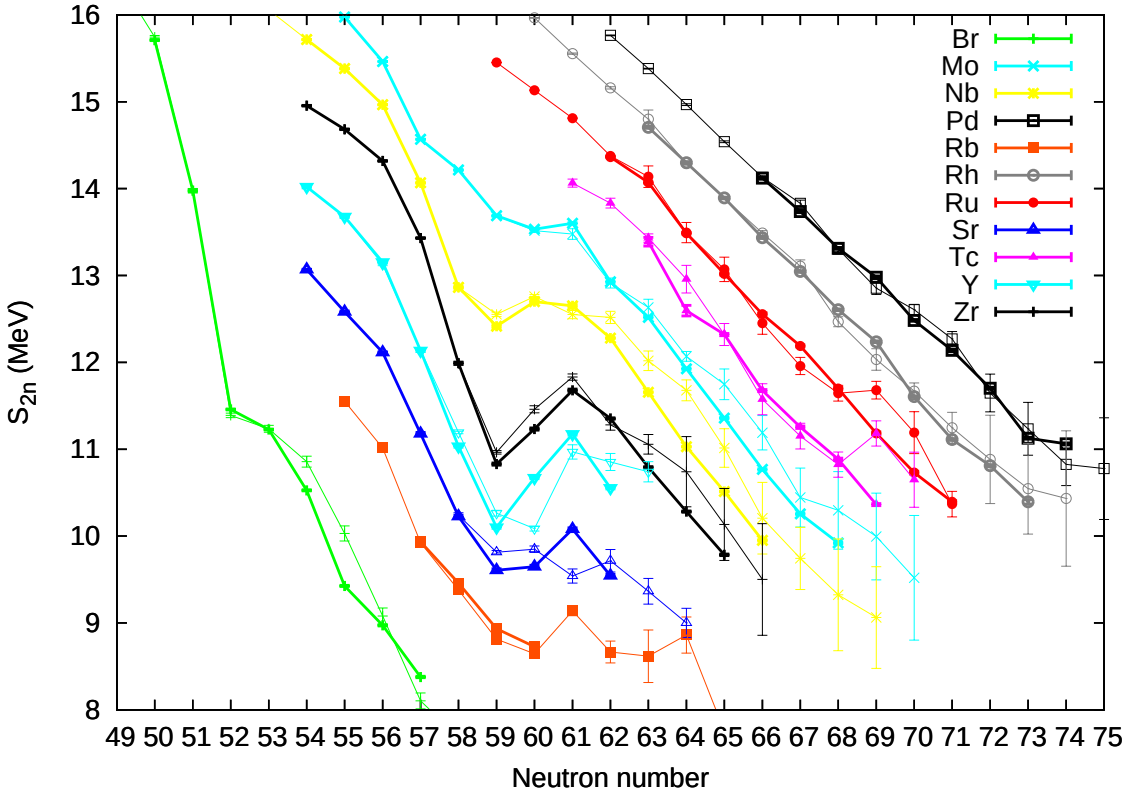

Figure 5.15: Two-neutron separation energy S_{2n} as a function of N.

It is interesting to note that all models seem to underbind the lighter nuclides, while overbinding the heavier ones (except for the two ETFSI calculations, which, at higher masses, tend to underestimate the binding again). All models change from less bound to more strongly bound than our mass values around $N \approx 59$. As was the case for the isotopes from technetium to palladium [20], the KTUY calculation gives far too low masses for the heavier nuclides compared here, with discrepancies of over 2.5 MeV. Both the calculations by Duflo and Zuker, as well, already in this region show the trend towards too large binding, which was also observed in the region from technetium to palladium, there especially in technetium. The HF based models all do comparatively well between $N = 60$ and $N = 68$, where the older HFB-2 seems to agree better than the newer HFB-9. All three models, however, seem to have problems reproducing the odd-even staggering. All in all, it seems that in the mass region examined here, none of the models yields the reliable predictions that would be needed for calculations of the astrophysical r-process.

5.4.3 Study of systematic trends

Two-neutron separation energy

The two-neutron separation energy $S_{2n} = -ME(A, Z) + ME(A-2, Z) + 2 \cdot ME(n)$, $ME(n)$ being the mass excess of the neutron, can be viewed as an indicator of major structural change and shell closures. Fig. 5.15 shows the two-neutron separation energy for all data included in this work. For the two isotopes closest to stability the needed mass excesses for the $(A-2)$ isotopes are taken from the AME03. The change in shell structure at $N = 60$ is clearly visible, especially around the

semi-magic zirconium. Another startling feature is the very smooth behaviour between technetium and palladium, which has been discussed in [20].
A different way of presenting the two-neutron separation energy is as a function the proton number Z, as shown in Fig. 5.16. In this figure, the change in structure is even more obvious, with an inversion of the two-neutron separation energies of $N = 60$ and $N = 62$ at $Z = 40$ in the even-N nuclei. The pronounced shell gap between $N = 56$ and $N = 58$ steadily decreases towards lower Z, i.e. more neutron-rich nuclei. In the odd-N nuclei the lines marking $N = 59$ and $N = 61$ are completely inverted up to $Z = 42$, where normal ordering is again established.

Due to the strikingly smooth behaviour of the two-neutron separation energy in the technetium, ruthenium, rhodium and palladium isotopes, a simplified liquid drop model equation was fitted to the values in [20]. For the even-even nuclei, this was compared to the E2 transition energy from the lowest excited 2^+ state to the 0^+ ground state, as shown again in Fig. 5.17. According to the microscopic calculations of Ref. [66], for even-even nuclei the shape change in the case of axial deformation from prolate to oblate is predicted to occur at $N = 66$ for ruthenium and $N = 68/70$ for palladium in good agreement with the energies of the first 2^+ states. For ruthenium, the decrease in the S_{2n} value (relative to the fit) beyond $N = 66$ coincides with the appearance and lowering of the oblate minimum. For palladium, the situation in light of the model calculation is quite different. Coexistence of two shapes close in energy and weakening deformation ($\beta_2 = -0.19, +0.14$) eventually seem to lead to stronger two-neutron binding. A weakening of the deformation at $N = 74$ is also supported by the increase in the energy of the first 2^+ state to nearly 450 keV. Therefore, it can be concluded that rather small changes in nuclear structure are visible in the ground state binding if the masses are known to a precision of significantly better than 100 keV.

It is also interesting to compare the two-neutron separation energy to the changes in the mean-square charge radii, Fig. 5.18. The charge radii are taken from [67, 68, 69]. A strong increase of the charge radius is observed at $N = 60$. This effect is strongest for yttrium, for which also the changes in the two-neutron separation energy are most pronounced.

Neutron separation energy

As stated in chapter 2, the neutron separation energy $S_n = -ME(A, Z) + ME(A-1, Z) + ME(n)$ can give a clue as to the path of the r-process, which is assumed to proceed where $S_n \leq 3$ MeV. As can be seen in Fig. 5.19 this limit has not yet been reached in this work, though ^{92}Br comes close. Due to the odd-even staggering, however, this means that the masses of at least two more bromine isotopes further from stability will have to be measured in order to actually reach the r-process path.

Valence proton-neutron interactions

In order to isolate the average empirical proton-neutron interaction energy, δV_{pn} has been defined as a double difference of masses. For even-even nuclei, the average interaction of the last two neutrons with the last two protons is given by

$$\delta V_{pn}^{ee}(Z,N) = \frac{1}{4}\left([B(Z,N) - B(Z,N-2)] - [B(Z-2,N) - B(Z-2,N-2)]\right). \qquad (5.7)$$

For nuclei with odd proton number and even neutron number, the interaction strength of the last proton with the last two neutrons is

$$\delta V_{pn}^{oe}(Z,N) = \frac{1}{2}\left([B(Z,N) - B(Z,N-2)] - [B(Z-1,N) - B(Z-1,N-2)]\right), \qquad (5.8)$$

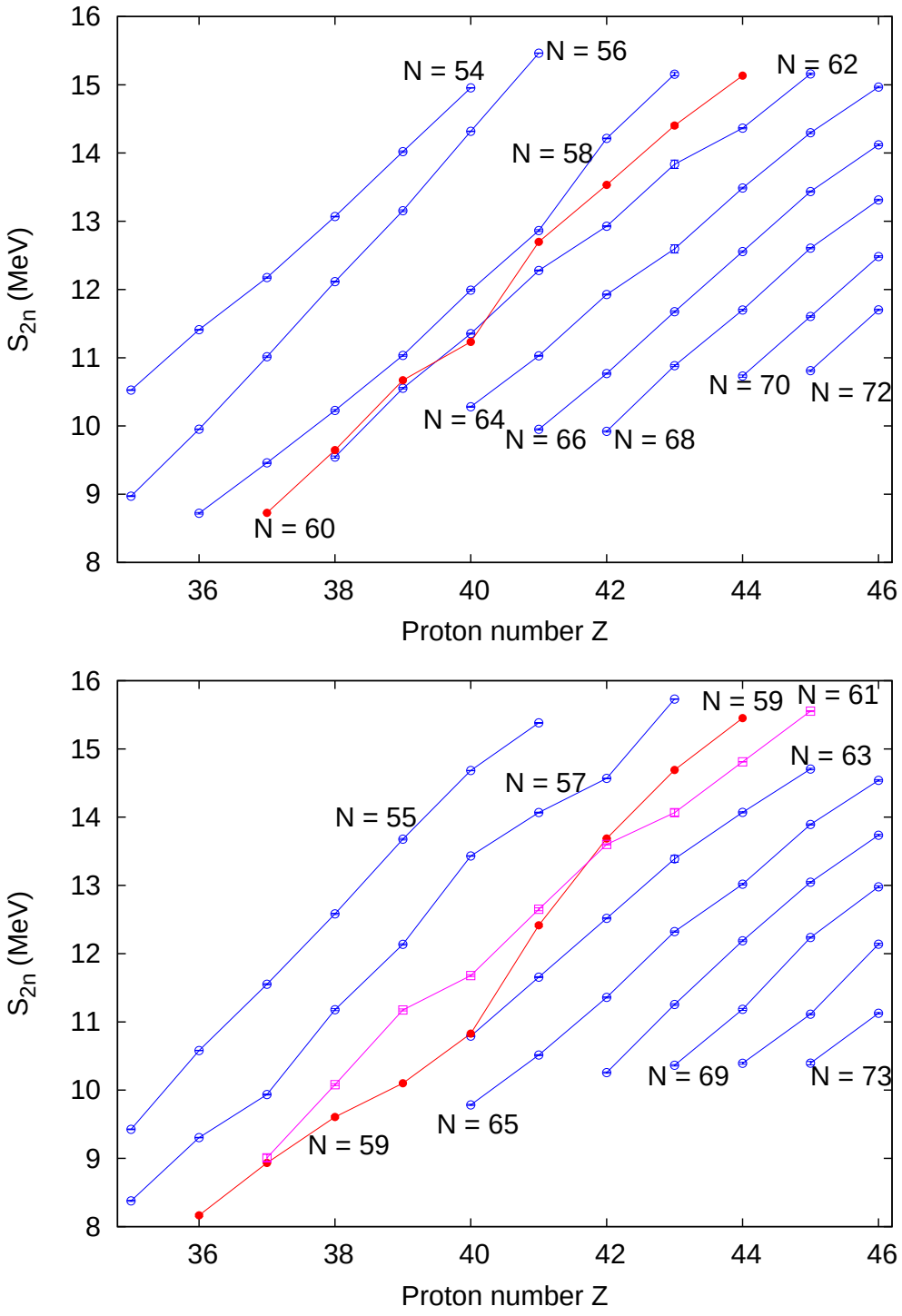

Figure 5.16: Two-neutron separation energy S_{2n} as a function of Z for even-N (top) and odd-N (bottom) nuclei.

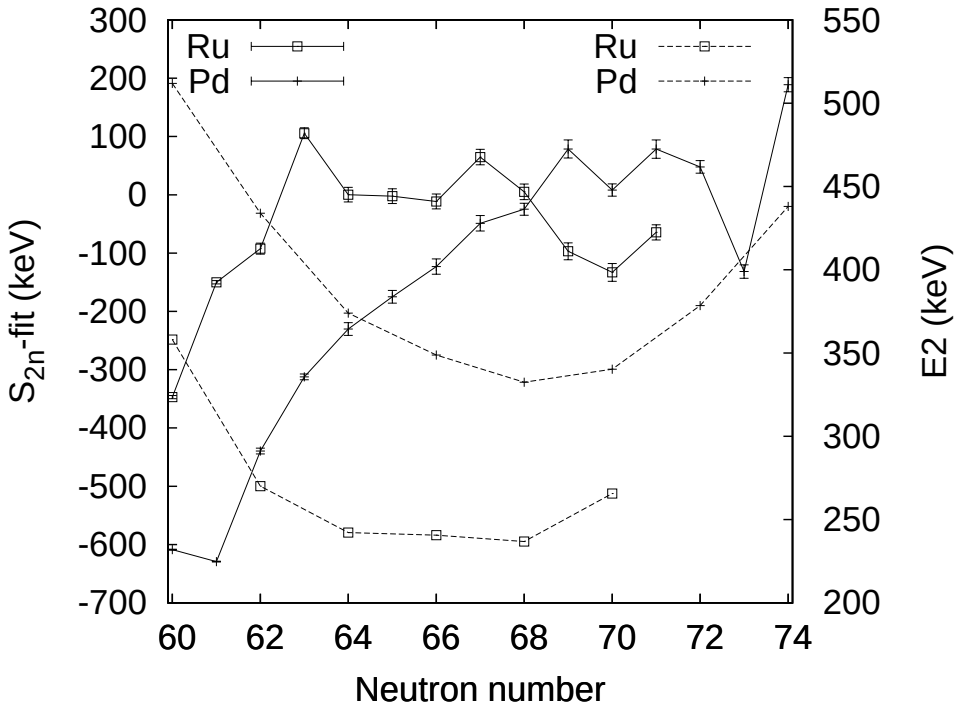

Figure 5.17: Two-neutron separation energy relative to the function given in [20] plotted with the E2 transition energy.

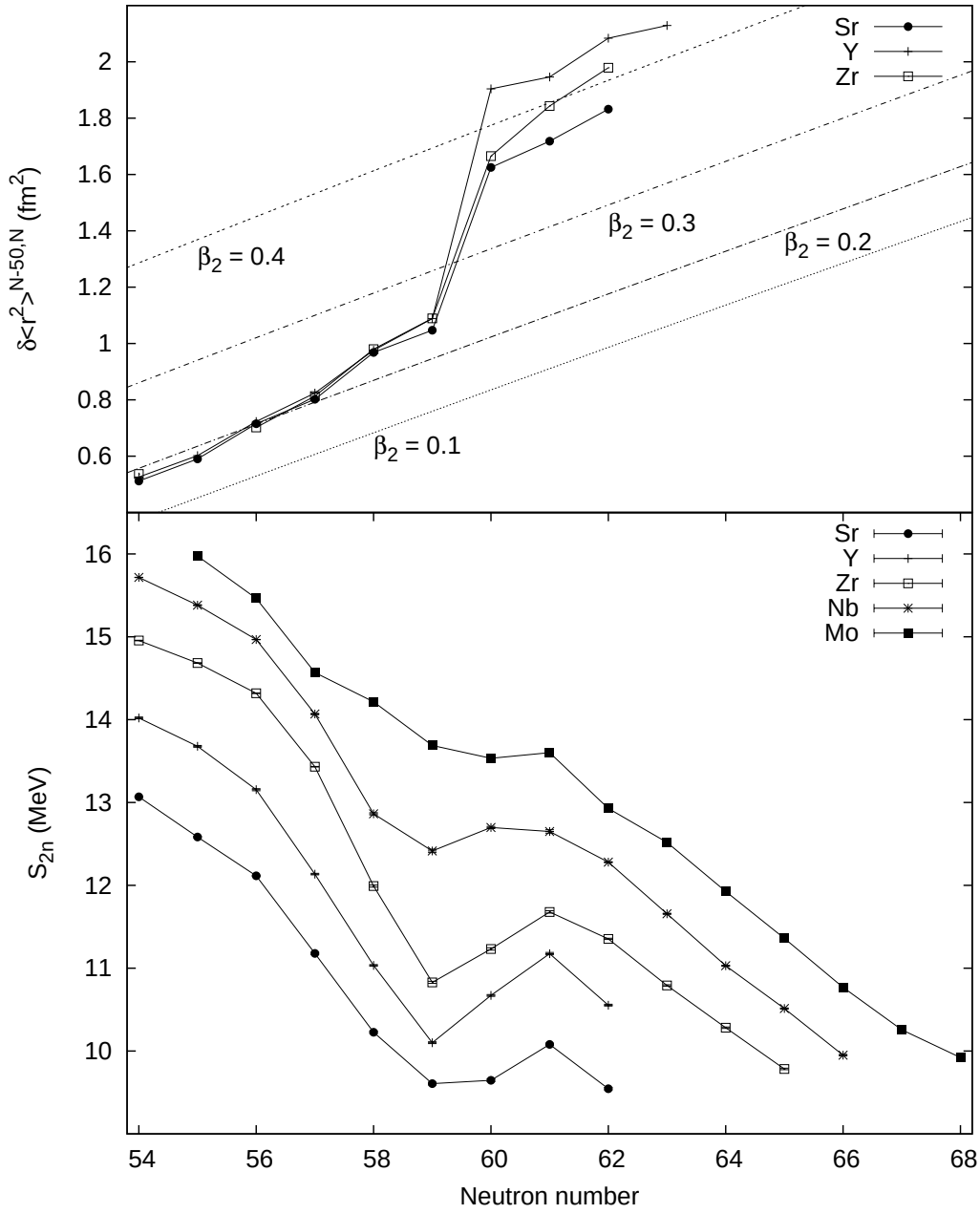

Figure 5.18: Two-neutron separation energies and relative mean-square charge radii $< \delta^2 >^{N-50,N}$ for the strontium, yttrium and zirconium isotopes around $N = 60$. Droplet model isodeformation lines [68] for yttrium are shown dashed.

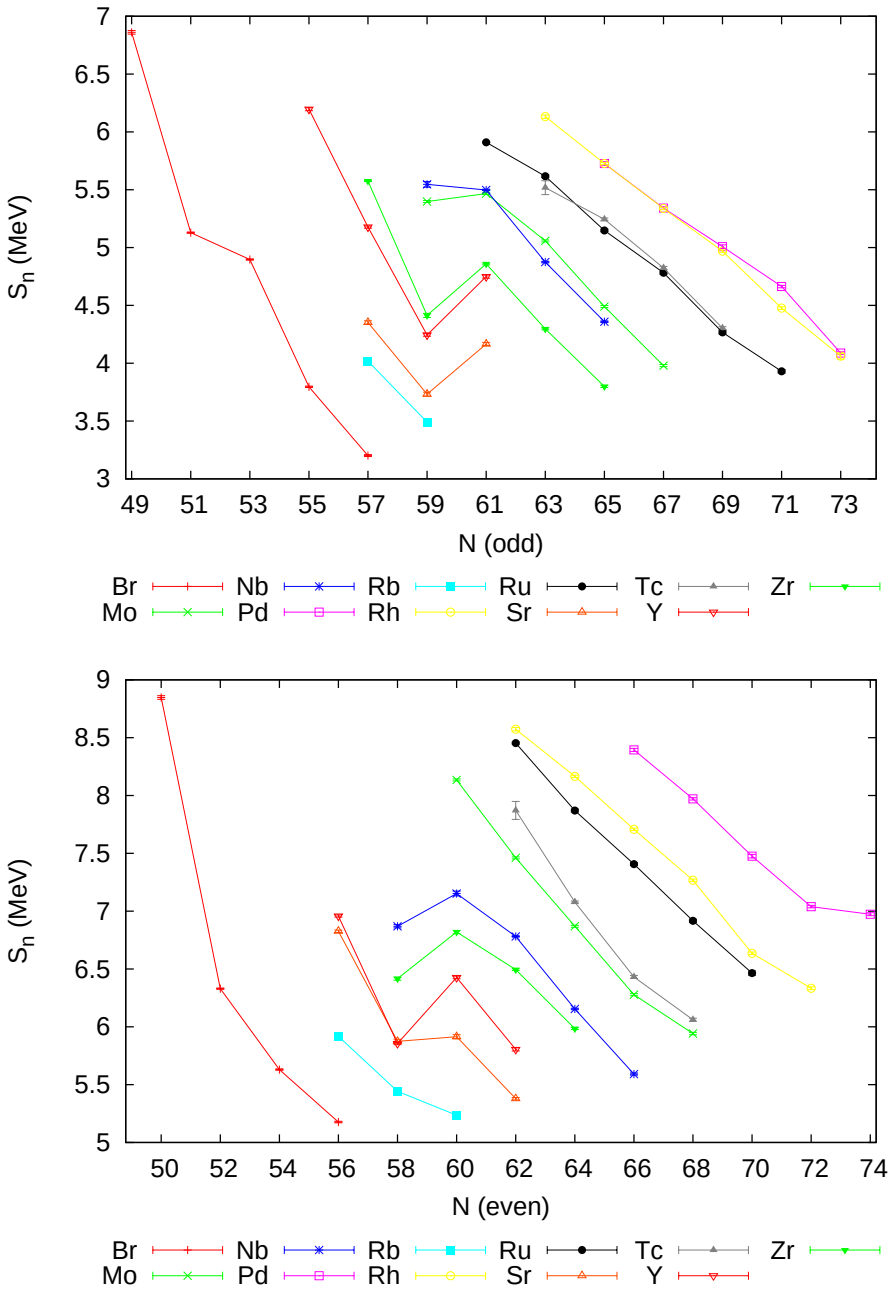

Figure 5.19: Neutron separation energy S_n for odd (a) and even (b) neutron numbers.

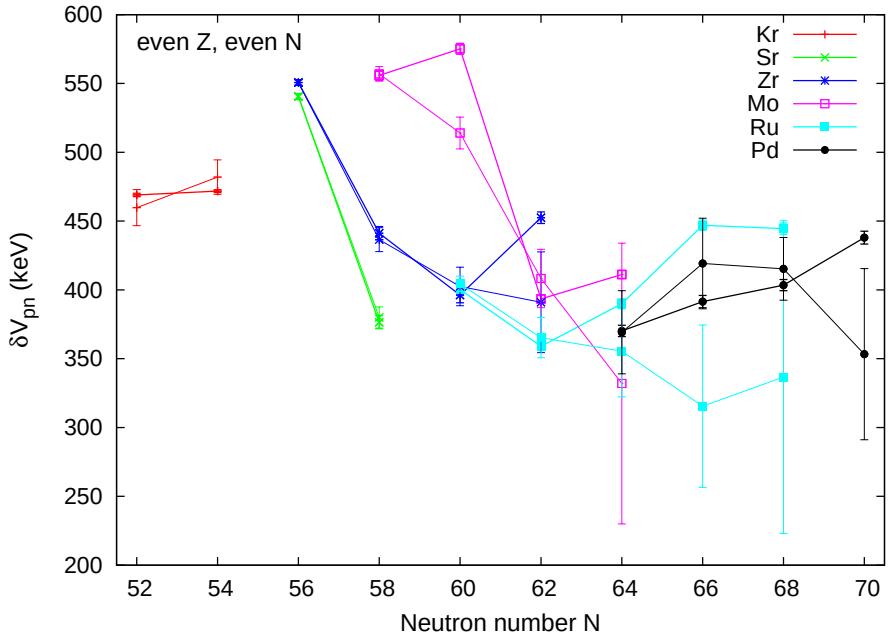

Figure 5.20: Average empirical proton-neutron interaction energy δV_{pn}^{ee} for even-even nuclei.

and similarly for even-Z–odd-N nuclei. δV_{pn} effectively cancels out other interactions to second order and isolates that of the last valence protons and neutrons. Larger values of δV_{pn} are expected if the last protons and neutrons are filling similar orbits. The δV_{pn} values calculated from the masses presented in this work, and including the krypton masses measured recently at ISOLTRAP [70], are shown in Figs. 5.20, 5.21 and 5.22, where the thin lines mark the old values based on the AME03, and the thick lines mark the new values based on the masses given in this work.

Brenner et al. [71] report several anomalies in the region covered here. The sudden increase of δV_{pn}^{eo} at ^{101}Zr has not been confirmed by our measurements. The other anomalies listed in [71] concern the δV_{pn}^{oe} of ^{101}Nb, ^{99}Y and ^{101}Y. It seems, however, that niobium and yttrium have been mislabelled in the relevant plot (Fig. 4 in [71]), and also the aforementioned anomalies are interchanged, i.e. they concern ^{99}Y, ^{101}Nb and ^{103}Nb. The sharp peak of δV_{pn} at ^{101}Nb is even more pronounced using the new data, with ^{101}Nb lying higher and ^{103}Nb lying lower than before. A similar discontinuity had been observed for ^{99}Y and ^{101}Y, with a sudden decrease at ^{99}Y and a sharp increase towards ^{101}Y. This anomaly has now been replaced by a relatively smooth behaviour. In addition, a sudden drop at ^{115}Pd has disappeared in the new values. The odd palladium isotopes, as well, now follow a smoother trend. Such a smooth behaviour is also observed for rhodium, and for the heavier ruthenium and technetium isotopes.

Since δV_{pn} is largest when the last protons and neutrons are filling orbits with large spatial overlap, it depends on the fractional filling of the neutron and proton shells [72]. In Fig. 5.23, δV_{pn}^{ee} is plotted as a function of both N and Z and the fractional filling of the shells $Z = 28$–50 and $N = 50$–82. According to the δV_{pn} scheme, the largest values are expected along the diagonal where the fractional filling are similar. This is not the case in this region.
Cakirli et al. [72] pointed out a correlation between δV_{pn} and $R_{4/2} = E(4_1^+)/E(2_1^+)$, which is considered to be a measure of collectivity and is plotted in Fig. 5.24. Clearly, collectivity increases abruptly in zirconium and strontium between $N = 58$ and $N = 60$, whereas molybdenum displays a smoother

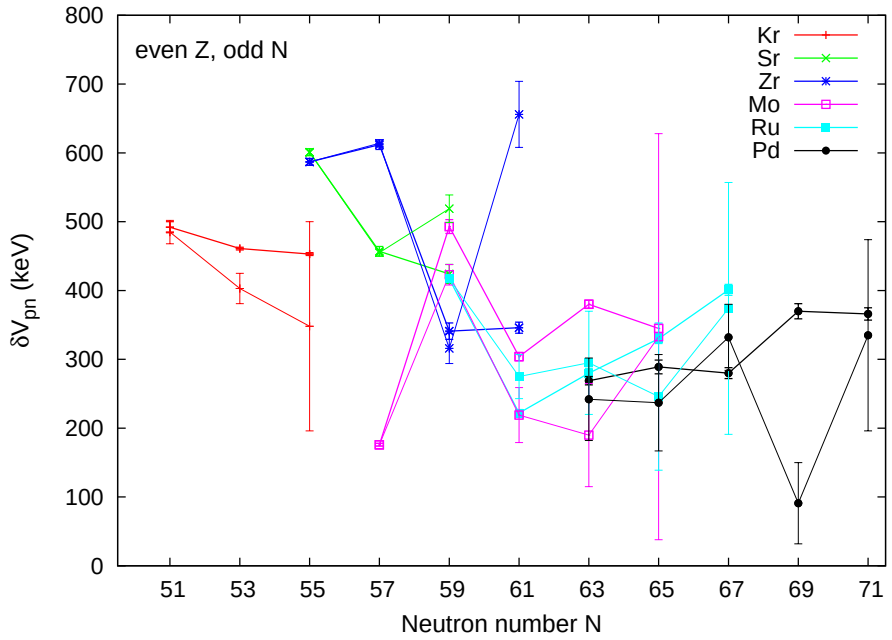

Figure 5.21: Average empirical proton-neutron interaction energy δV_{pn}^{eo} for even Z – odd N nuclei.

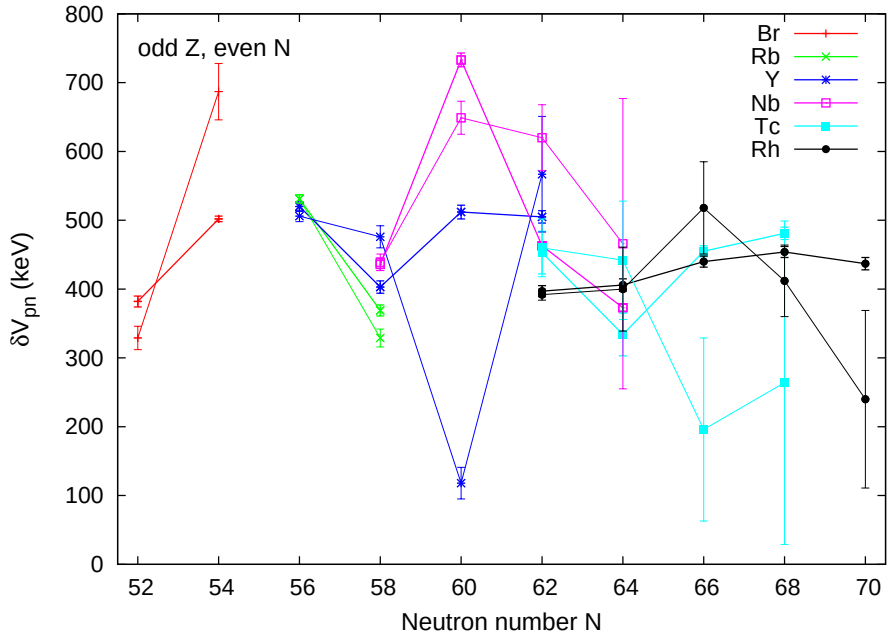

Figure 5.22: Average empirical proton-neutron interaction energy δV_{pn}^{oe} for odd Z – even N nuclei.

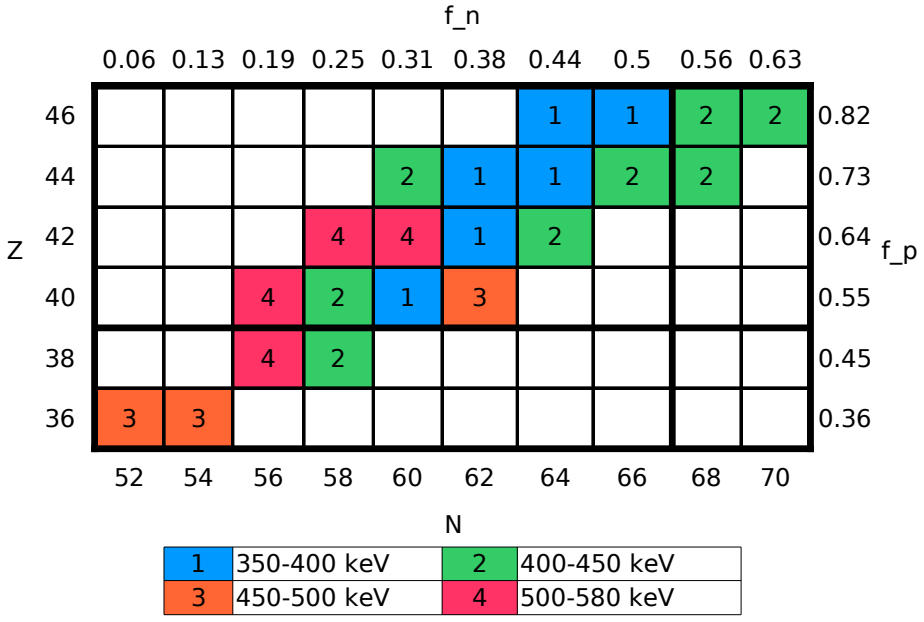

Figure 5.23: δV_{pn}^{ee} against N and Z. The fractional filling of the main shells is given on the top and right axis, respectively.

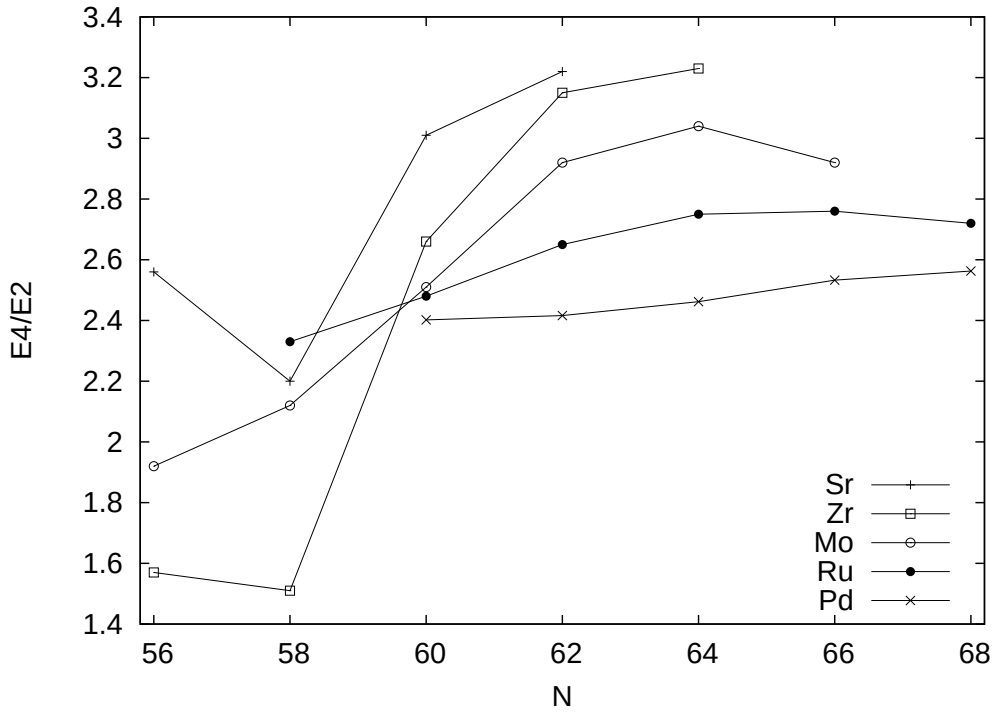

Figure 5.24: $E(4_1^+)/E(2_1^+)$ for strontium, zirconium, molybdenum, ruthenium and palladium.

Table 5.6: Comparison of δV_{pn} and $R_{4/2}$ for nuclides with corresponding numbers of valence proton and neutron particles or holes.

pair	δV_{pn} (keV)		$R_{4/2}$	
	p-h	p-p/h-h	p-h	p-p/h-h
^{110}Ru - ^{112}Ru	447.0(37)	444.5(41)	2.757	2.723
^{110}Pd - ^{116}Pd	370.2(41)	438.0(47)	2.462	2.578
^{112}Pd - ^{114}Pd	391.5(45)	403.5(41)	2.533	2.563
^{96}Zr - ^{94}Sr	550.7(21)	540.5(21)	1.571	2.564
^{98}Zr - ^{96}Sr	441.2(48)	376.5(47)	1.507	2.199

behaviour, as was the case for the two-neutron separation energy. In the palladium isotopes, $R_{4/2}$ is almost constant.

Cakirli et al. state that nuclei in the particle-particle (p-p) region (lower left corner of Fig. 5.23) and hole-hole (h-h) region (upper right corner of Fig. 5.23) both δV_{pn} and $R_{4/2}$ will be larger than for corresponding nuclei in the particle-hole (p-h) region (upper left corner of Fig. 5.23). In the limited dataset discussed here, only five such pairs can be compared. These are listed in Table 5.6 For the two palladium pairs the observation by Cakirli et al. holds, and the h-h nuclides have larger collectivity and larger valence proton-neutron interaction than the corresponding p-h nuclides. For the ruthenium pair the values are almost equal. For the two strontium-zirconium pairs, however, this simple model does not hold. While $R_{4/2}$ is still larger for the p-p nuclides than for the p-h nuclides, δV_{pn} shows the opposite behaviour.

An interesting application of the δV_{pn} scheme is the extrapolation of unknown mass values. δV_{pn} can be approximated by

$$\delta V_{pn}(Z,N) \approx \frac{\partial^2 B}{\partial Z \partial N} \,, \tag{5.9}$$

the mixed partial derivative of the binding energy. While it was seen in section 5.4.2 that the absolute binding energies predicted by current global models are rather unreliable when moving away from stability, this second derivative can be expected to be better reproduced, as the pairing only weakly affects δV_{pn}[73]. Thus, if three masses are known, and δV_{pn} can be calculated from model binding energies, it is possible to use Eq. 5.7 to extrapolate the fourth mass. For a sample of the models examined in section 5.4.2, δV_{pn} was calculated and compared to experimental values (including [70]), Figs. 5.25–5.29. All these models display discrepancies for strontium, zirconium and molybdenum around $N = 60$. The values for ruthenium and palladium are better reproduced, especially by the HBF-9 calculations. It is worth of notice that the deviations are in all cases below 300 keV. This is a considerable improvement over the agreement of the absolute binding energies from which the δV_{pn} are calculated. To test the mass prediction power of these δV_{pn} values, the binding energies of ^{110}Mo, ^{114}Ru, and ^{120}Pd were calculated using Eq. 5.7. The binding energies were taken from this work, except for those of ^{120,122}Cd which were taken from the AME03. The results are presented in Fig. 5.30. The models mostly give too large a binding energy, only in the case of ^{114}Ru does the HFB-9 result in a slightly low binding energy. The ETFSI-2 calculation agrees remarkably well with the experimental value for ^{120}Pd. Compared to the often large discrepancies found for the calculated absolute binding energies in section 5.4.2, the extrapolations based on δV_{pn} are far closer to the experimental values. This is, however, not surprising, since three of the four input parameters in Eq. 5.7 are taken directly from experiment, and the fourth value, the actual δV_{pn}, is usually around 500 keV. Another drawback is that each further step away from stability increases the uncertainty considerably.

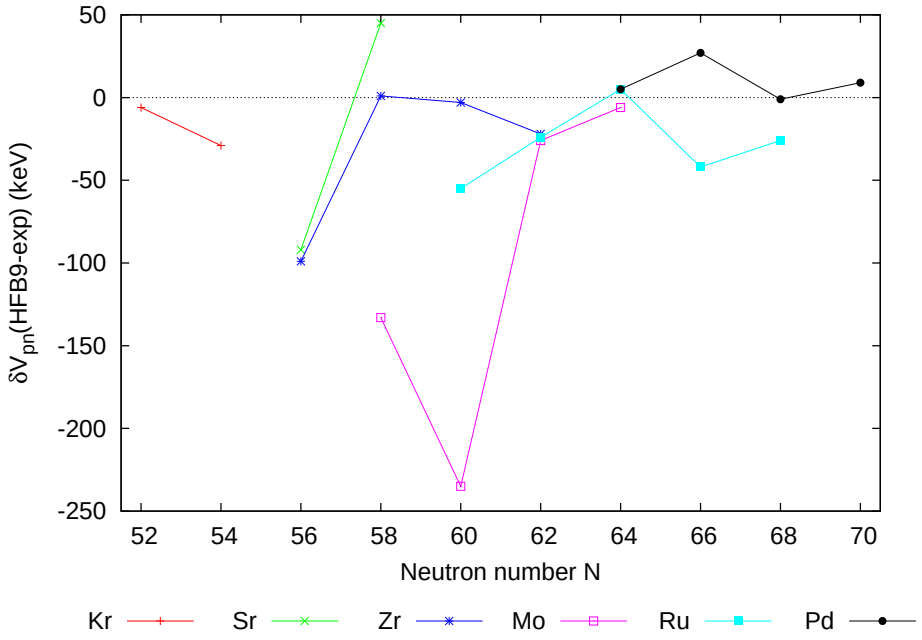

Figure 5.25: δV_{pn}^{ee}, HFB-9 for even-even nuclei.

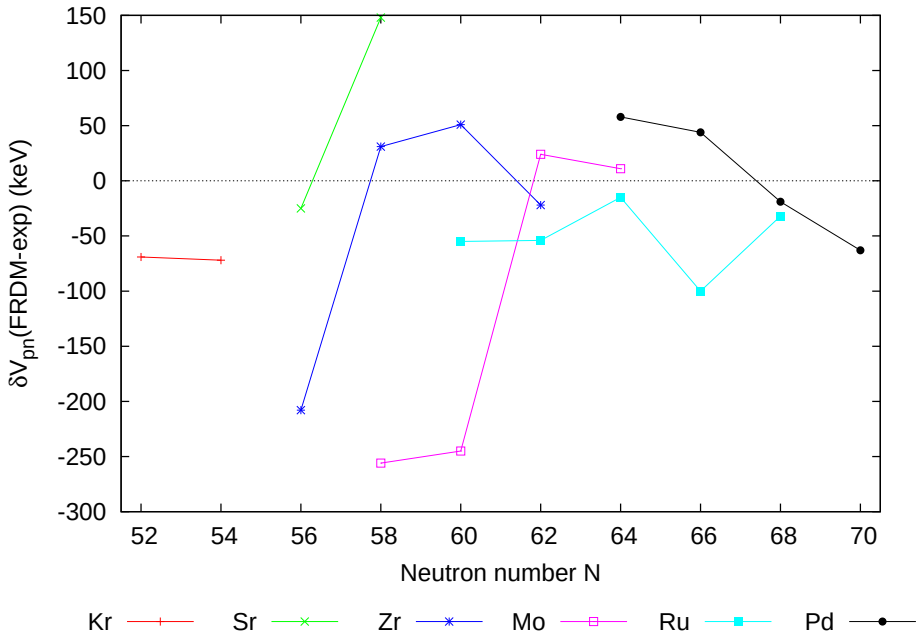

Figure 5.26: δV_{pn}^{ee}, FRDM for even-even nuclei.

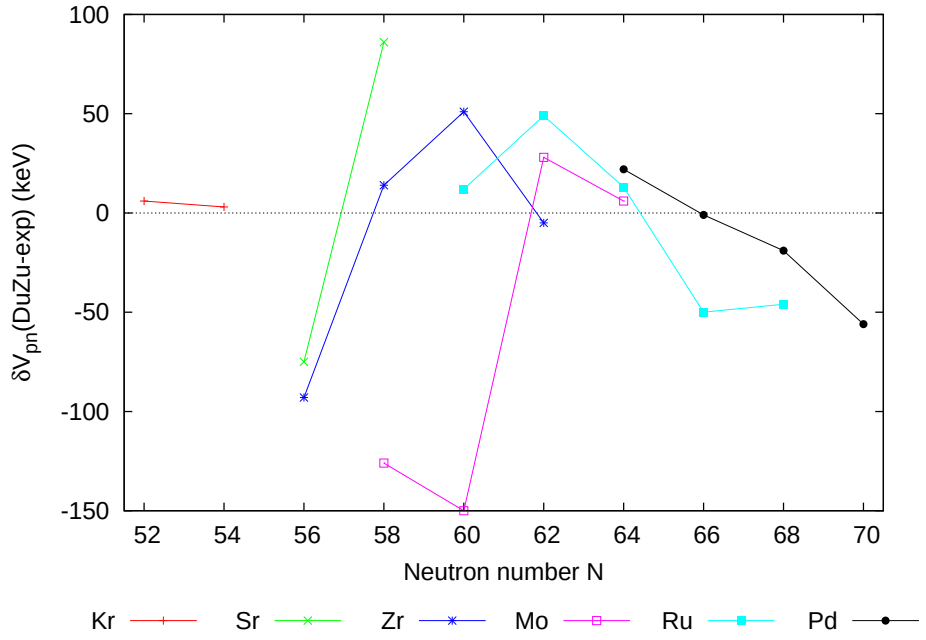

Figure 5.27: δV_{pn}^{ee}, Duflo-Zuker (28 parameters) for even-even nuclei.

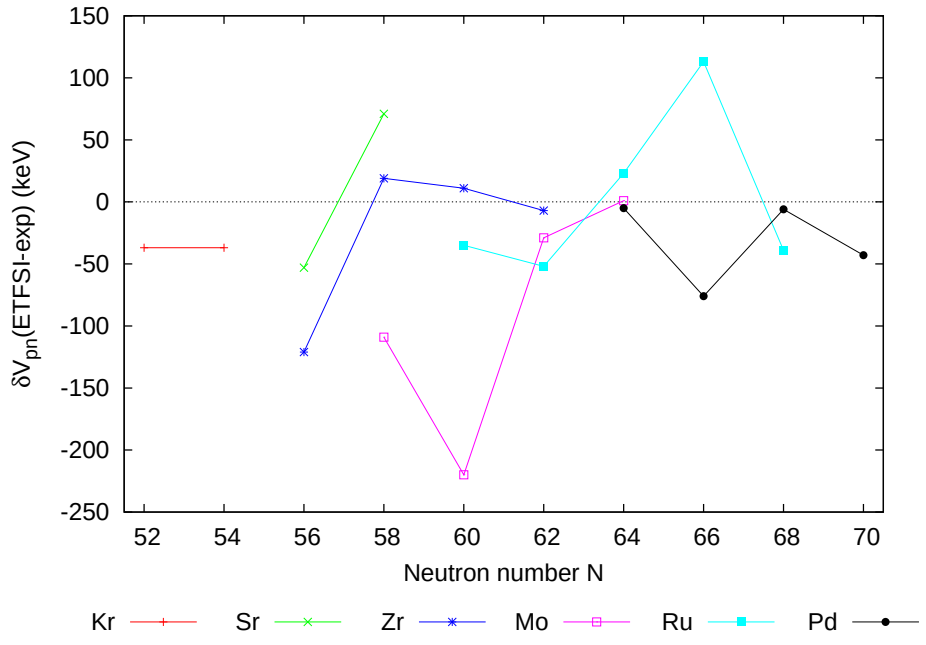

Figure 5.28: δV_{pn}^{ee}, ETFSI-2 for even-even nuclei.

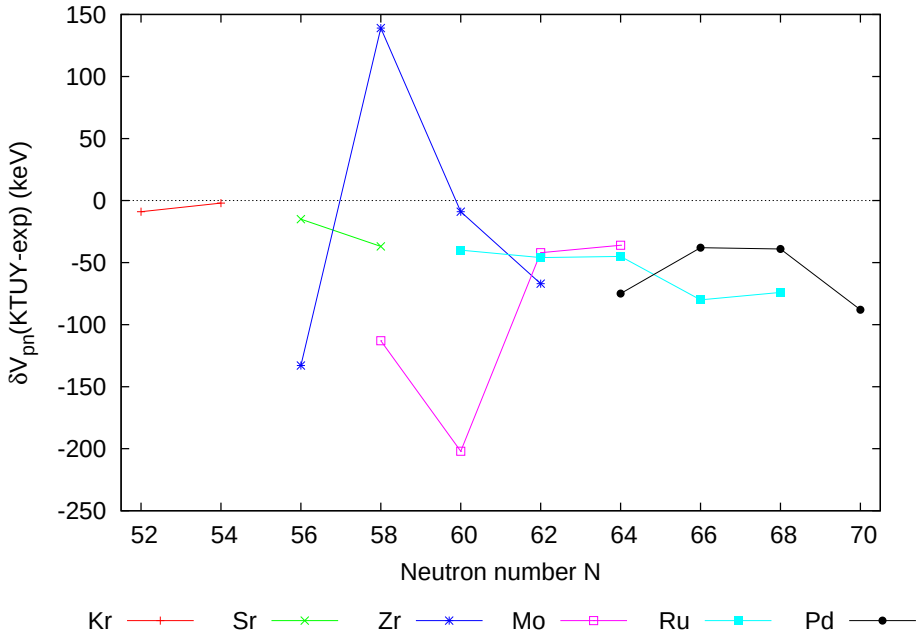

Figure 5.29: δV_{pn}^{ee}, KTUY for even-even nuclei.

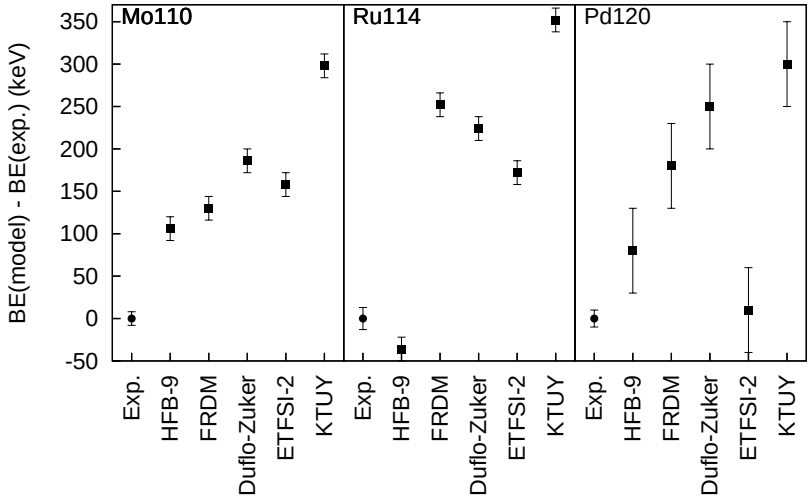

Figure 5.30: Extrapolated binding energies using theoretical δV_{pn} values, relative to the JYFLTRAP value. Note that larger values mean larger binding and smaller mass. The larger uncertainties for ^{120}Pd are due to the larger uncertainties of the binding energies of ^{120,122}Cd from the AME03 used to calculate this value.

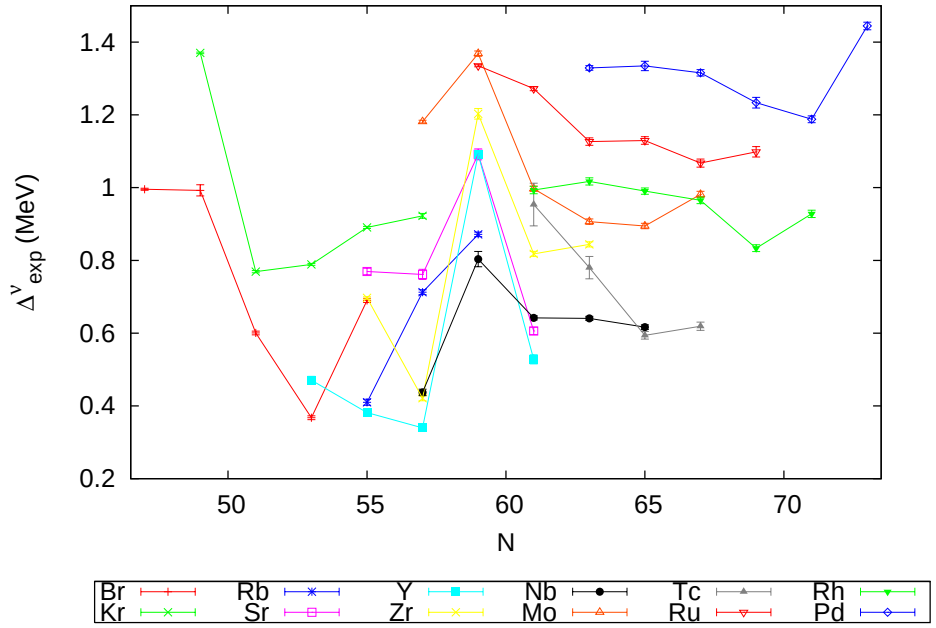

Figure 5.31: Neutron odd-even staggering three-point indicator Δ^{ν} as a function of neutron number N (N odd).

Odd-even staggering

A measure of the empirical pairing gap can be obtained from the three-point expression

$$\Delta^{(3)}(n) = \frac{\pi_n}{2}[B(n-1) + B(n+1) - 2B(n)] \,, \tag{5.10}$$

where $\pi_n = (-1)^n$ is the number parity, B is the (negative) binding energy, and n is the number of particles, either Z or N, while the other one is kept constant. Fig. 5.31 shows the odd-even staggering as a function of neutron number for odd N, calculated according to

$$\Delta^{(3)}_{\nu}(N) = -\frac{1}{2}[B(Z, N-1) + B(Z, N+1) - 2B(Z, N)] \,.$$

For ruthenium, rhodium and palladium and for the heavier molybdenum isotopes the pairing gap is relatively smooth, and its increase with increasing Z is visible, with the even-Z elements having a larger pairing gap. The sudden change at $N = 60$ in zirconium and yttrium clearly shows as a sharp peak at $N = 59$ and equally sharp decrease at $N = 60$. In strontium, niobium and molybdenum this effect is also present, albeit less pronounced. This peak shows that the indicator Δ^{ν} breaks down at this point, since the neighbouring even-N nuclides used in deriving Δ^{ν} have different deformations.

6 Spectroscopy at ISOLTRAP

The aim of this project is to install a tape station on top of the ISOLTRAP setup (Fig. 4.14). This will, on the one hand, enable background-free decay spectroscopy with isobarically and even isomerically pure samples, and on the other hand, it will assist precision mass measurements by allowing the determination of the measured species, especially in the case when only one of two or more isomeric states is observed in the trap. Using ISOLTRAP, a mass separation of about 100 keV can be reached, depending on the excitation time, which in turn depends on the half-life of the studied nuclide, and a ratio of contamination to ion-of-interest of up to 10^3 can be tolerated. While the mass resolution of the GPS/HRS together with the RILIS laser ion source theoretically provides isotopically pure beams, contaminations due to surface ionisation can still cause problems. Using ISOLTRAP for purification would therefore be feasible for mass numbers with large contaminations and for elements which cannot currently be ionised using RILIS. An example of the former is the region around neutron-rich mercury, thallium and lead, where contamination due to francium ions is a problem, as can be seen in Fig. 6.1. Thallium has 81 protons, thus the ground state should be formed by one proton hole in one of the close-lying $h_{11/2}s_{1/2}d_{3/2}$ orbits below the $Z = 82$ shell gap. For even-A–odd-N isotopes beyond $A = 206$ this hole can couple to a neutron in one of the $g_{9/2}d_{3/2}i_{11/2}$ orbits and thus form the low-lying states. ^{208}Pb is doubly magic, and therefore the low-lying nuclear structure of the heavier isotopes should be governed only by valence neutrons above $N = 126$. In higher-lying states excitation of protons across $Z = 82$ may take place. However, data on these nuclides is scarce, partly due to contamination problems. Trap-assisted spectroscopy would enable the study of the evolution of single-particle states with an increasing number of protons, thus shedding light on the little-known interaction between proton holes and neutrons around $Z = 82$ and $N = 126$.

6.1 Current situation

A picture of the upper part of the current ISOLTRAP setup, including the magnet for the precision trap and the extraction beamline is shown in Fig. 6.2. The beamline ends in a double cross in which the channeltron detector is housed. Alternatively, an MCP detector can be inserted. The electrode structure as reproduced in the ion-optical simulation program SIMION is shown in Fig. 6.3.

6.2 Designing the new extraction beamline in SIMION

Since the ring electrode is at -2.5 V when the ions are ejected and the tape is on ground, the ions do not have sufficient energy to reach the tape. Therefore, one of the electrodes in the drift section must be switched down. For this, the long drift tube before the valve was chosen, as it is the longest electrode, so the ions' time of flight through the electrode will be long enough for switching (around 6 μs).

The new geometry is limited by space constraints, as the crane bridge in the ISOLDE hall leaves only little space in the vertical, and the platform on which the precision trap is located gives a horizontal limit. Considering these limitations, three sets of three electrodes and one drift tube were added to the SIMION ion-optical bench, which will still leave ample room for the crane to pass above the

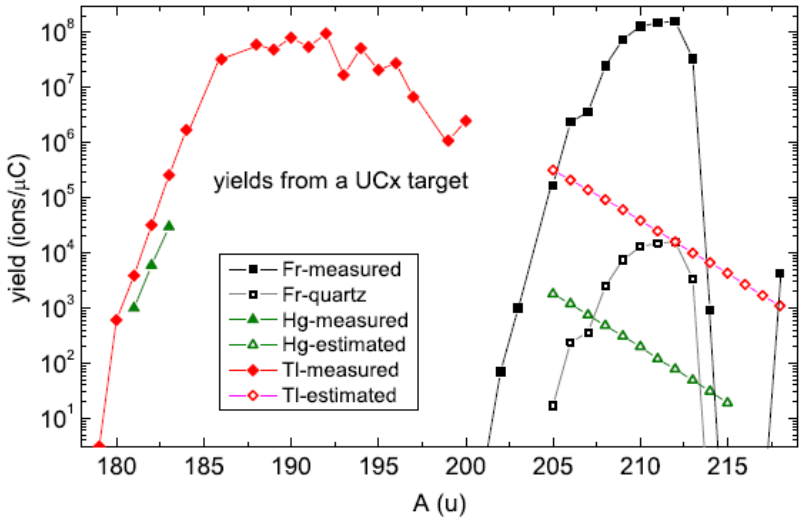

Figure 6.1: Yields at ISOLDE for mercury, thallium and francium using a uranium-carbide target and the RILIS. The neutron-rich yields of the francium surface-ions are measured, the RILIS yields for mercury and thallium are estimates. Using a quartz transfer line should reduce the francium contamination sufficiently to enable purification even of mercury.

Figure 6.2: The upper magnet and the extraction beamline of ISOLTRAP. The aluminium tube is part of the temperature stabilisation system.

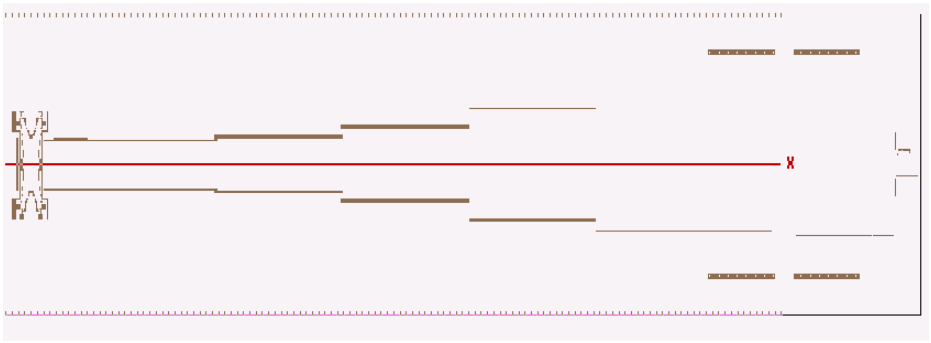

Figure 6.3: The ISOLTRAP extraction reproduced as a SIMION ion-optical bench as currently implemented. On the left is the hyperbolical precision trap, on the right hand side the Channeltron detector. A valve is located where the red cross is.

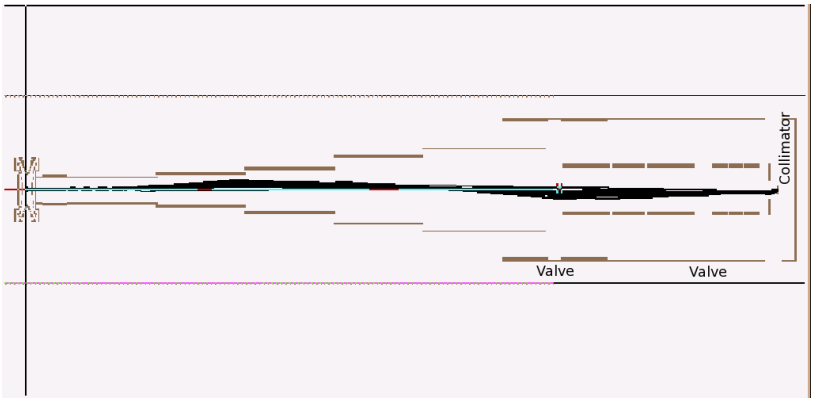

Figure 6.4: SIMION, simulation of the new geometry. The black lines mark the paths of a sample of ions being ejected from the trap.

new setup. The tape is located in a second, specially designed cross. With this design, ions of mass number $A = 85$ are in the pulsed tube about 405 μs after being extracted from the trap, depending on the applied voltages. Pulsing the tube by 200 V results in the detection of all ions, as can be seen in Fig. 6.4. A larger voltage difference might, however, be needed to prevent the ions from diffusing out of the tape during transportation.

Testing the Channeltron in the new geometry. The Channeltron was placed in the new geometry, removing the drift tube in the double cross above the lower valve. The channeltron will be located 44 mm lower than previously. It is, however, still possible to detect the ions after adjusting the electrode voltages. Instead of using the three new electrodes before the Channeltron as an einzel lens, the first two of these together with the previous drift tube can also be tuned as an einzel lens. The geometry including the Channeltron is shown in Fig. 6.5.

6.3 Construction of the new detection setup

In order to avoid having to construct a complicated beamline and support structure for the tape station, it was decided to keep the tape station in air and have a differential pumping section mounted

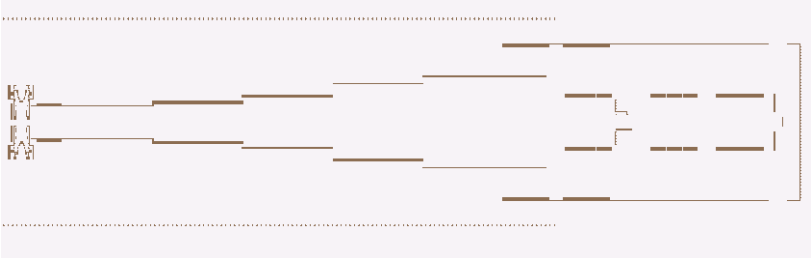

Figure 6.5: SIMION ion-optical bench of the new ISOLTRAP extraction geometry with the Channeltron.

on the main beamline where the tape is entering the cross. The tape station and detectors can then be placed lower, since the space above the trap is very limited due to the hall's bridge crane, as mentioned above. The tape station could also be placed on a separate table, simplifying construction and access. The detectors should, however, still be as close as possible to the implantation point, in order to reduce transport time and minimise the decay of short-lived nuclei.
The new setup will consist of two parts: a lower stage to replace the current Channeltron section, and an upper part for the tape, as was already implemented in the simulations. Each part needs access through various flanges to connect all needed devices. Between the two parts there will be a CF 100 valve to separate the high-vacuum (better than 10^{-8} mbar) lower part from the tape station, where the vacuum is expected to be considerably worse, of the order of a few 10^{-5} mbar. The design of both new chambers and the valve between them are shown in Fig. 6.6. The complete design of the new setup on the platform is shown in Fig. 6.7. The lower cross is mounted at an angle to enable access to the liquid helium filling valve. The actual tape station is placed below the three detectors. The design of the upper cross is specialised. It is shorter than a normal cross to fit at the end of the beamline. It will also provide mounting for the differential pumping chamber, see section 6.3.1. In addition, it will be possible to mount a MCP for tuning purposes.

6.3.1 Differential pumping section

The slit setup to bring the tape from vacuum to air is based on the one developed at GSI, Fig. 6.8. To accommodate two slits for the tape (into the vacuum and back out again) in a similar setup, the slits are rotated by 90° relative to the original slit, Fig. 6.9. The outer dimensions are identical, so the original chamber design, shown in Fig. 6.10, can be used.

6.4 Status

Some parts of the beamline have already been manufactured. Figure 6.11 shows the lower cross with the extension piece. The extension has been modified by adding a connection piece for the pressure gauges. Several flanges with electrical feedthroughs have been designed. These are shown in Fig. 6.12, attached to the lower cross and the upper part. The upper part has not yet been modified to allow connection of the differential pumping section.
A proposal has been submitted to the ISOLDE and Neutron Time-of-Flight Committee to perform mass measurements followed by β- and γ-decay studies on isobarically pure beams of neutron-rich mercury and thallium isotopes.

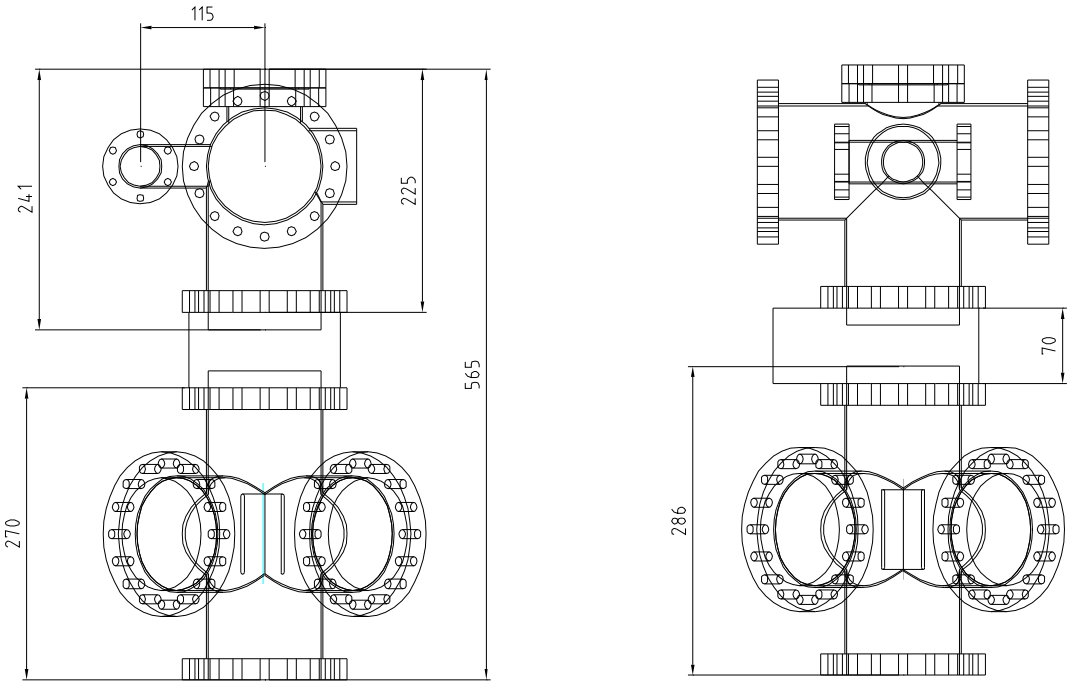

Figure 6.6: Design of both new crosses and the two valves after the ISOLTRAP precision trap, seen from two perspectives.

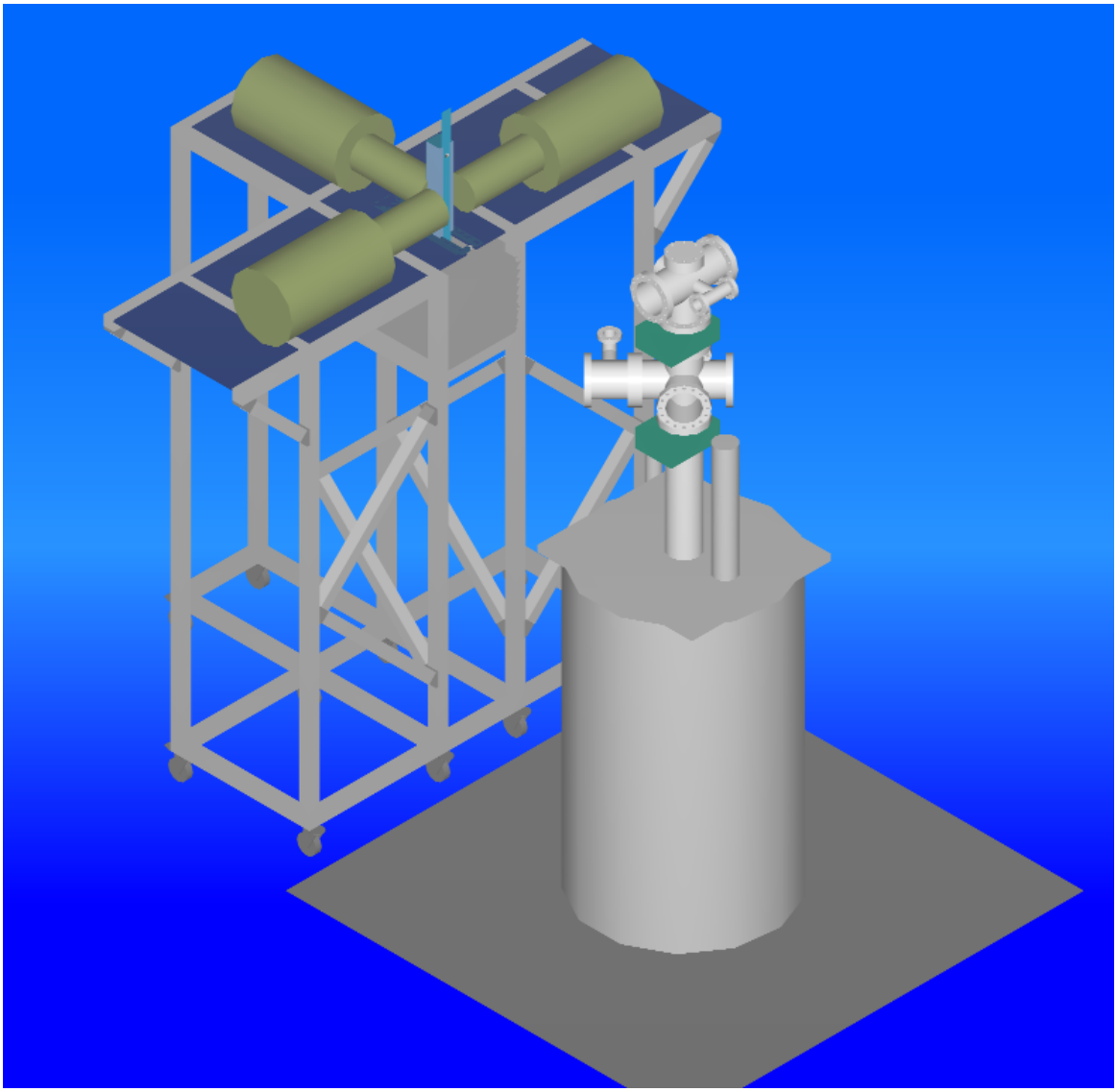

Figure 6.7: The trap and the detector/tape station table with three germanium detectors.

Figure 6.8: Differential pumping/slit system to guide the tape into vacuum developed by Wilfried Hüller at GSI.

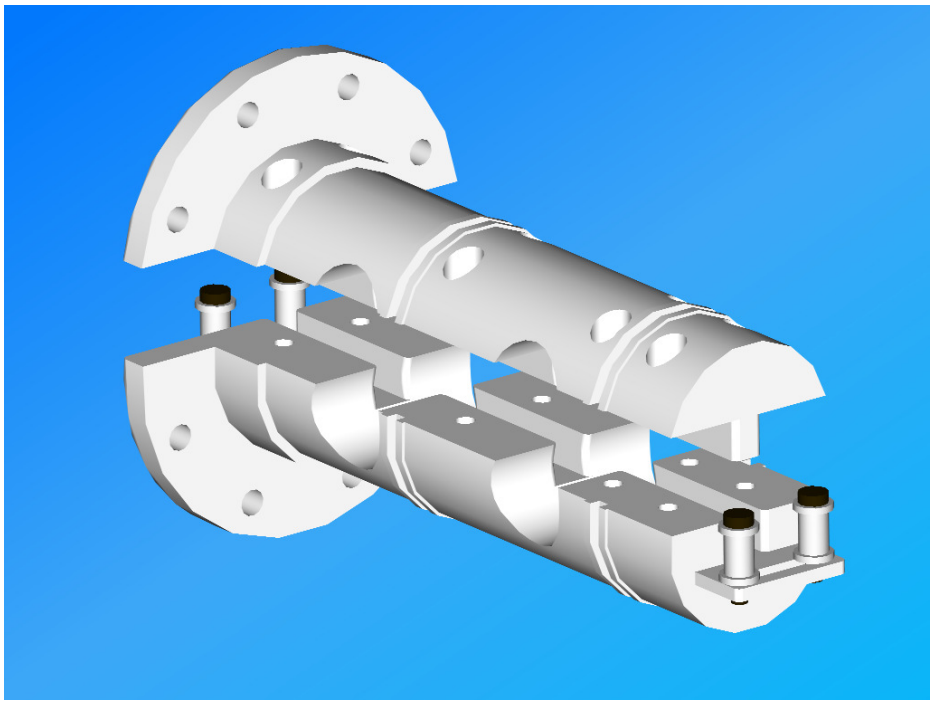

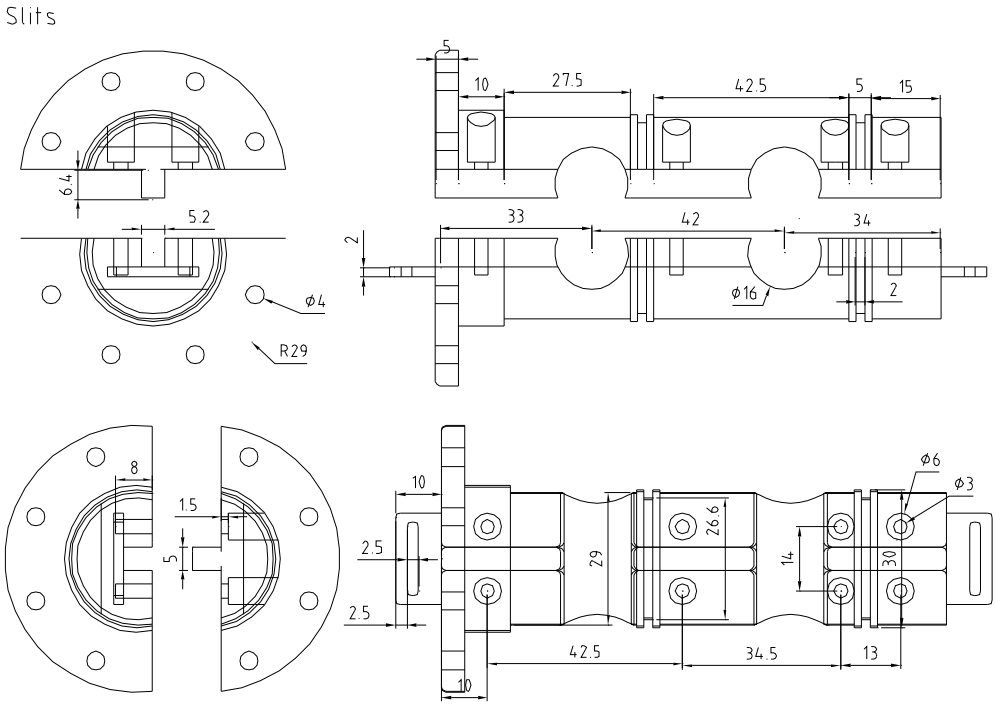

Figure 6.9: The inner part of the pumping section.

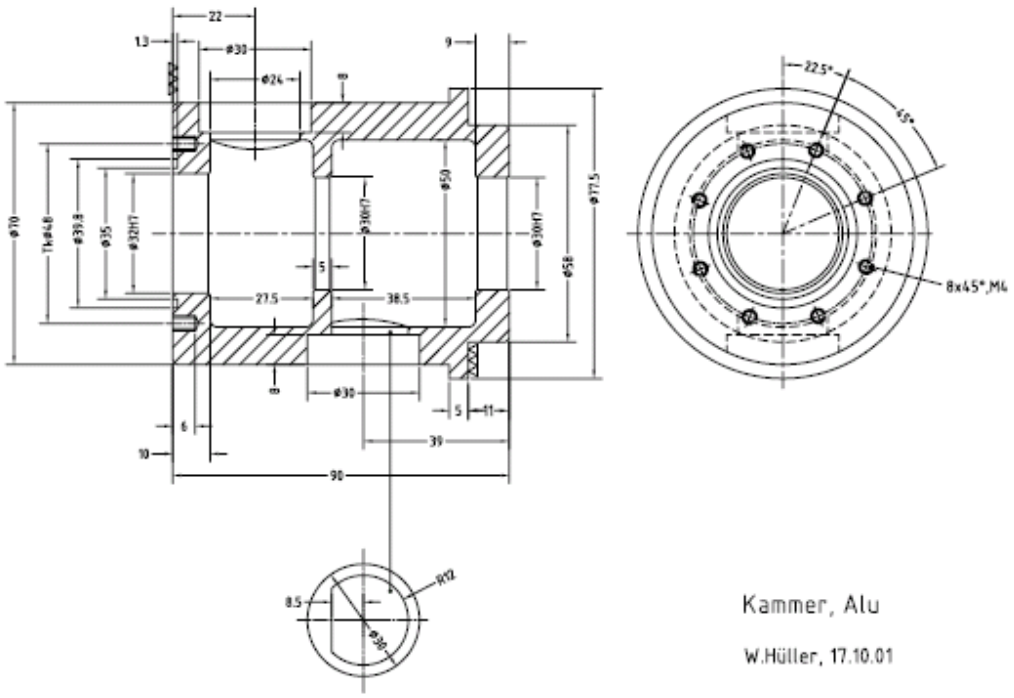

Figure 6.10: Differential pumping/slit system developed by Wilfried Hüller, outer chamber which will house the part in Fig. 6.9

Figure 6.11: The lower cross with the extension piece to enable the connection of a pump and pressure gauges.

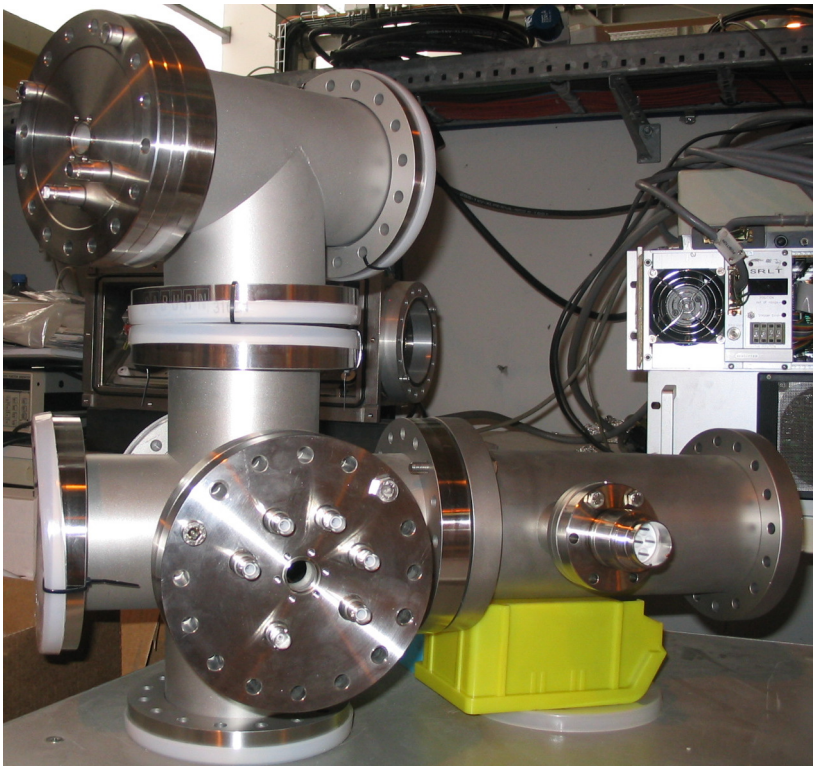

Figure 6.12: Lower cross, extension piece and upper part with flanges and electronic feedthroughs. The upper part has not yet been modified to add the flange for the differential pumping section.

7 Summary and outlook

All in all, 73 nuclear masses measured with the JYFLTRAP Penning trap mass spectrometer were presented in this work. Being located in a region of the nuclear chart portraying various shape changes, these mass values can help considerably improve the current knowledge of nuclear structure. The reached precision enables mapping of even relatively minor trends on the mass surface. The found discrepancies between the new results and the literature values showed in many cases, e.g. niobium and technetium, systematic trends. As the parameters of the mass models were fitted to this wrong input data, wrong model predictions are to be expected, and are indeed observed. This, in turn, can lead to wrong prediction for astrophysical processes. The mass measurement campaign initiated in this work is still being continued with mass measurements towards lighter nuclei around the N = 50 shell closure. So far, several neutron-rich isotopes of germanium, gallium, arsenic, selenium and nickel have been measured. At ISOLTRAP, neutron-rich krypton, copper and zinc isotopes have been measured. Combined, these precision data yield a new picture of the mass surface in this region of the nuclear chart. In the near future, this region will be further extended by measuring isotopes of heavier fission products at JYFLTRAP. In addition, several nuclides with unresolved isomeric states presented in this work may be revisited using a new technique for isomeric cleaning employing a Ramsey excitation [74] recently developed and tested at JYFLTRAP. Figure 7.1 shows a cleaning spectrum of ^{115}Sn and ^{115}In ($\Delta m \approx 500$ keV or 4.5 Hz) from an offline ion source. The dipole excitation frequency was applied as two time-separated fringes of 10 ms with a waiting time of 80 ms in between. After the excitation, the non-excited ions were transferred back into the first trap, while the ions in resonance had too large a cyclotron radius to pass the 2 mm diaphragm separating the traps. Thus, a clean sample can be obtained even for ion species with mass differences too small for purification in the first trap. The resulting, clean time-of-flight resonance spectra are shown in Fig. 7.2.

In order to improve the accuracy and precision of JYFLTRAP a carbon cluster source has been designed and will be installed for offline studies. This will lead to a better understanding of the systematic uncertainties encountered. In particular the mass dependent uncertainty can be remeasured by comparing carbon clusters of various sizes. The count rate effect, too, can be studied systematically in such a way. Another important factor is the timing of the potential wall between the two Penning traps. Its opening time must correspond exactly (within a few hundred ns) to the flight time of the ions in order for the ions to have as low a kinetic energy as possible upon entering the second trap. Any nonlinearities and irregularities of the voltage switches could thus be examined.

The design of a new decay spectroscopy setup after ISOLTRAP commenced in 2005. This effort is being continued and will provide a possibility for background free spectroscopy. The tape will be guided out of the vacuum through a differential pumping section to a separate measurement station, increasing the flexibility in setting up different detectors. The first parts have been manufactured by the workshop of the University of Mainz. A proposal for measurements in the region of neutron-rich mercury and thallium has been submitted.

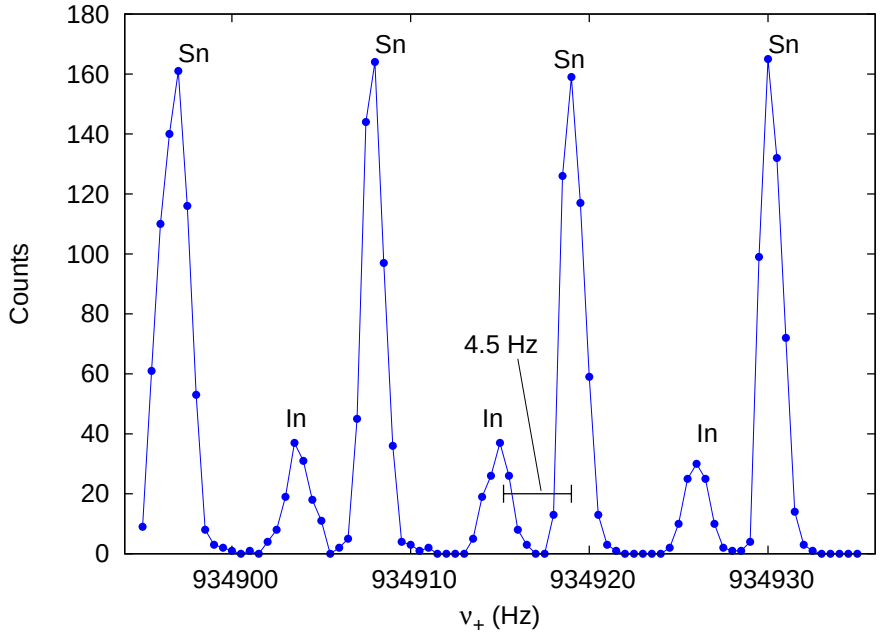

Figure 7.1: ν_+ scan in the precision trap using the Ramsey excitation method.

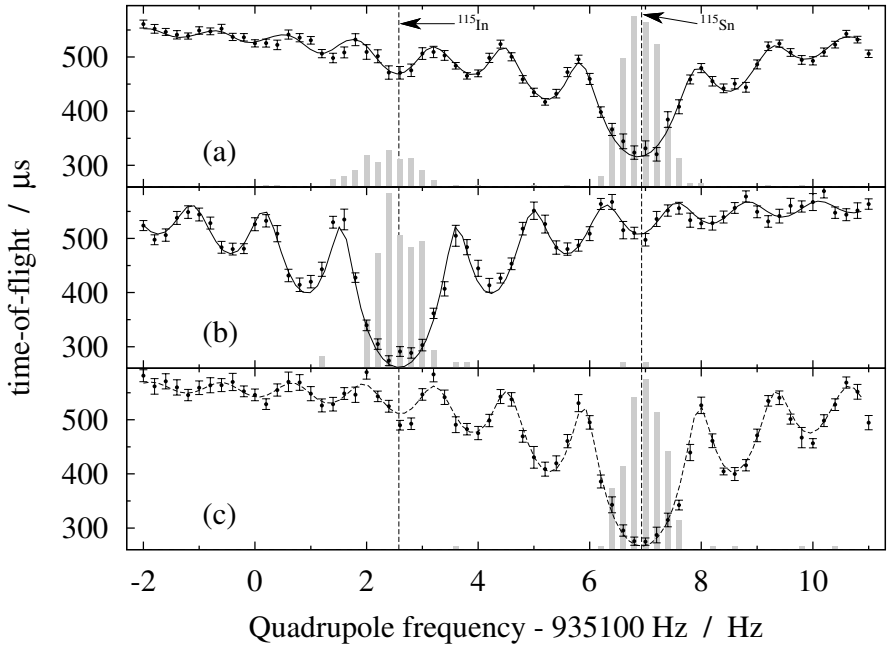

Figure 7.2: Time-of-flight resonance spectra of ^{115}Sn and ^{115}In, the shaded areas represent the ions in resonance (arb. scales). In the top panel, no additional cleaning in the precision trap was used. In the other panels, Ramsey cleaning was used. In the middle panel, the dipole excitation was set to the reduced cyclotron frequency ν_+ of ^{115}Sn, thus removing it from the trap and leaving a clean sample of ^{115}In. Finally, in the bottom panel, ^{115}In was removed, and ^{115}Sn measured.

A Analysis programs

A.1 Frequency calibration and contaminations

Unwanted contamination in the traps can often be hard to identify. If, however, a resonance frequency can be determined, it is possible to calculate the atoms and molecules that would have a corresponding resonance frequency. To this end, a program was written in C++ which, based on the AME03 [28] mass table, combines atomic masses and compares them to the observed one. No additional information about chemistry is included. The number of atoms in the molecule can be specified, as can be an uncertainty for the center frequency. The same program also serves to calibrate the timings and frequencies relevant for JYFLTRAP. Any molecule can be given, and the program will return the cyclotron frequencies in both traps, the reduced cyclotron frequency in the precision trap, which is needed for isomeric cleaning, and the transfer times between the cooler and purification trap, and between the purification and precision trap. To simplify the input, carbon clusters can be specified in multiples of ^{12}C. A graphical user interface was written using GTKmm, as seen in Fig. A.1.

A.2 Data fitting

In order to determine the ions' cyclotron frequency from a time-of-flight resonance spectrum, the theoretical line shape is fitted to the measured data points. This is done by the Levenberg-Marquardt method, a nonlinear least-squares fitting routine. The original code was taken from the *Numerical Recipes in C* [75] and adopted to fit the theoretical time-of-flight resonance shape. Based on this fitting routine, two separate programs were developed to analyse data from JYFLTRAP. The program used in this work is command line based, reading in an ASCII input file. In the input file it is possible to limit the used data according to different criteria. The recorded ion bunches can be sorted depending on the total number of ions recorded. This can be used to limit the minimum and maximum ions per bunch which will be included in the analysis and to do a count rate class analysis [49]. For the count rate class analysis, an additional linear fitting routine is used to extrapolate the frequency to a specified ion number, depending on the assumed efficiency of the extraction and the detector. A second way of limiting the used data is to limit the time-of-flight window during which ions have to arrive at the detector. This has to be done after sorting the recorded bunches according to the ion number, so that the total number of ions in the trap is used for the count rate class analysis. Setting a time-of-flight window can be used to reduce the background and enhance the time-of-flight effect.

Several resonance spectra of the same ion species can be specified in the input file and will be handled by the program without having to restart it. All the spectra taken during a run can thus be fitted at the same time. The program will output ASCII files giving the fitted parameters and the frequencies, and plots of all fitted spectra, all count rate class analyses, and the fitted frequencies versus time. Thus, it is possible to quickly get a good overview of the data. Since the input file is saved as well, modification and re-fitting can easily be done. A graphical user interface was written in Python to generate the input file for the fitting program, see Fig. A.2.

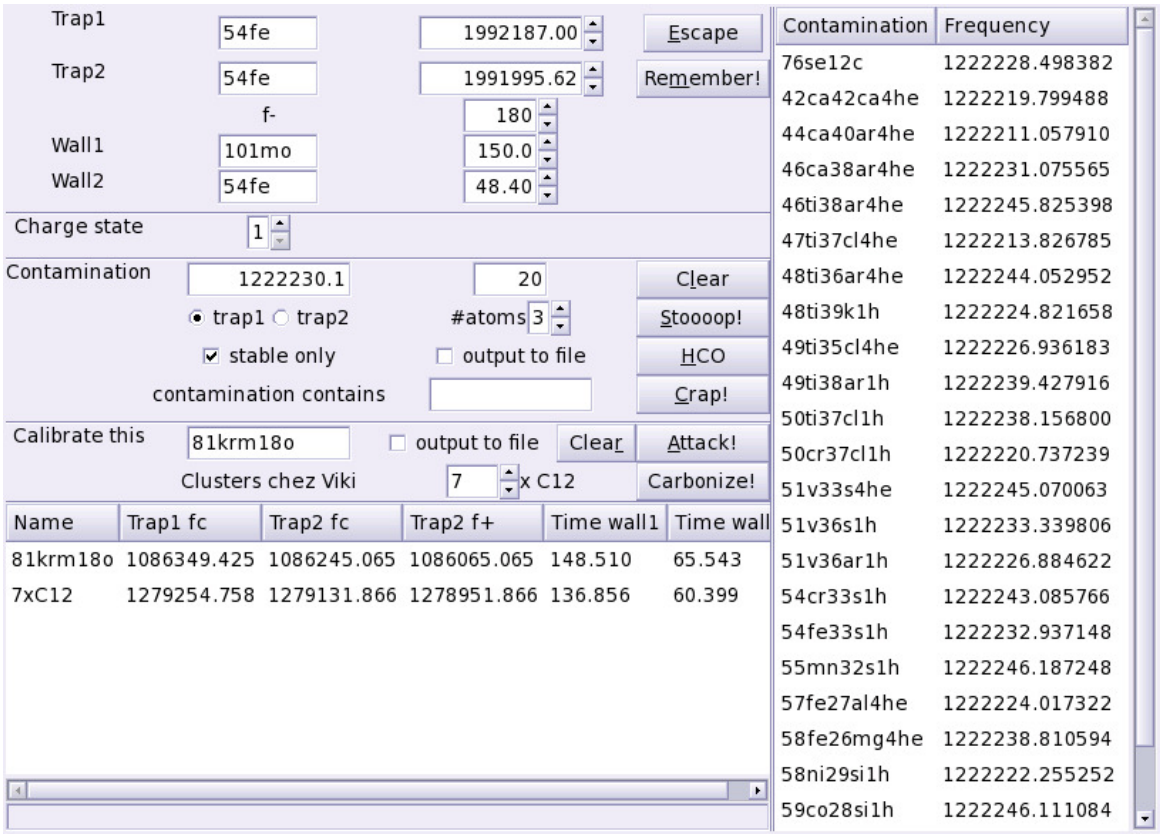

Figure A.1: A calculator for frequencies and timings and for determining contaminations from measured frequencies.

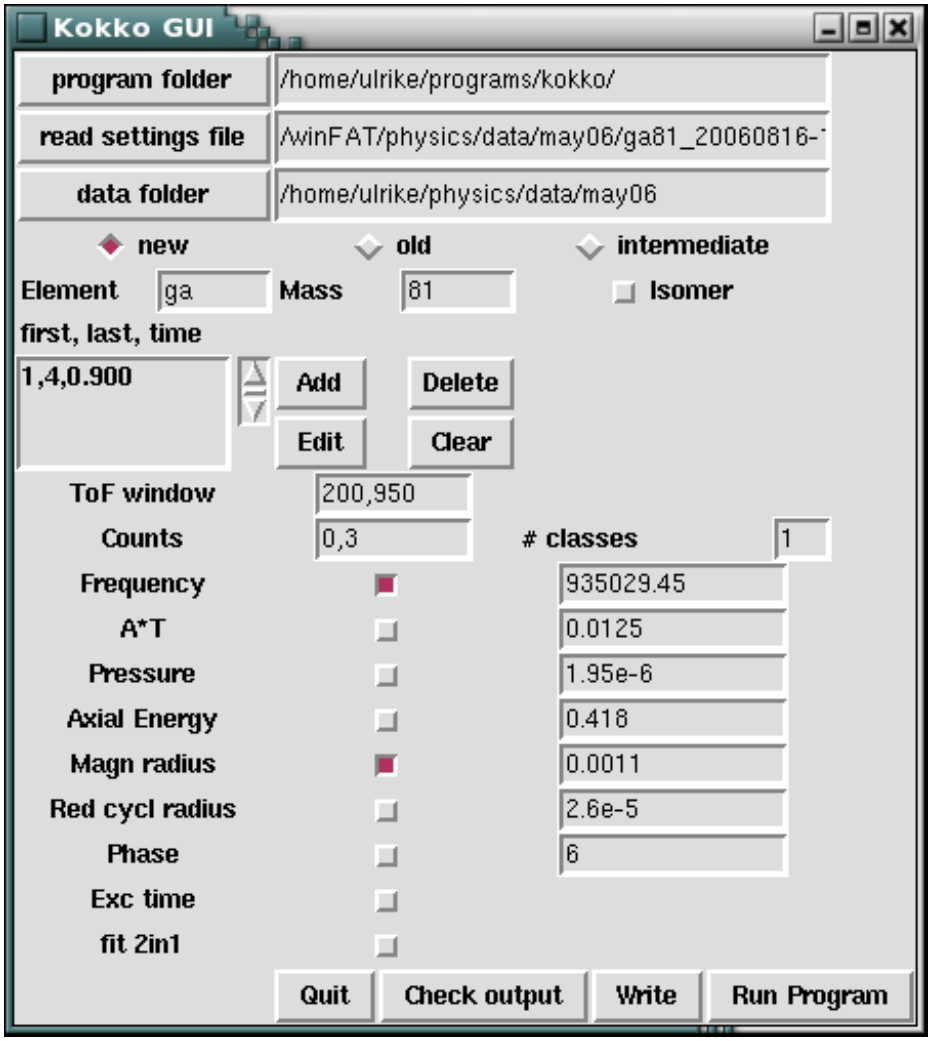

Figure A.2: A GUI for the fitting program.

The lists of fitted frequencies generated by the fitting program can be read in by different programs, also written in C++. One of these determines the fluctuation of the magnetic field from the reference measurements, another the average count rate effect from all fitted resonances, and finally one which calculates the frequency ratios and mass excesses and compares them to the AME03 values. Uncertainties accounting for the magnetic field fluctuations, the count rate and the mass dependent uncertainty can be included.

Bibliography

[1] J. Stachel, P. V. Isacker, K. Heyde, Interpretation of the $A \approx 100$ transitional region in the framework of the interacting boson model, Phys. Rev. C 25 (1982) 650–657.

[2] R. Aryaeinejad, J. D. Cole, R. C. Greenwood, S. S. Harrill, N. P. Lohstreter, Band crossing in neutron-rich Pd isotopes via spontaneous fission of ^{252}Cf, Phys. Rev. C 48 (1993) 566–573.

[3] G. Lhersonneau, B. Pfeiffer, K.-L. Kratz, Evolution of deformation in the neutron-rich Zr region from excited intruder state to the ground state, Phys. Rev. C 49 (1994) 1379–1390.

[4] M. Houry, R. Lucas, M.-G. Porquet, C. Theisen, M. Girod, M. Aiche, M. Aleonard, A. Astier, G. Barreau, F. Becker, J. Chemin, I. Deloncle, T. Doan, J. Durell, K. Hauschild, W. Korten, Y. L. Coz, M. Leddy, S. Perries, N. Redon, A. Roach, J. Scheurer, A. Smith, B. Varley, Structure of neutron rich palladium isotopes produced in heavy ion induced fission, Eur. Phys. J. A 6 (1999) 43–48.

[5] B. Pfeiffer, K.-L. Kratz, F.-K. Thielemann, W. B. Walters, Nuclear structure studies for the astrophysical r-process, Nucl. Phys. A 693 (2001) 282–324.

[6] U. Hager, T. Eronen, J. Hakala, A. Jokinen, V. S. Kolhinen, S. Kopecky, I. Moore, A. Nieminen, M. Oinonen, S. Rinta-Antila, J. Szerypo, J. Äystö, First Precision Mass Measurements of Refractory Fission Fragments, Phys. Rev. Lett. 96 (2006) 042504.

[7] Y.-Z. Qian, Nuclear physics and astrophysics of the r-process, Nucl. Phys. A 752 (2005) 550–559.

[8] D. Lunney, J. M. Pearson, C. Thibault, Recent trends in the determination of nuclear masses, Rev. Mod. Phys. 75 (2003) 1021.

[9] S. Rinta-Antila, T. Eronen, V.-V. Elomaa, U. Hager, J. Hakala, A. Jokinen, P. Karvonen, H. Penttilä, J. Rissanen, T. Sonoda, A. Saastamoinen, J. Äystö, Decay study of neutron rich zirconium isotopes employing Penning trap as a spectroscopy tool, Eur. Phys. J. A 31 (2007) 1–7.

[10] P. Ring, P. Schuck, The Nuclear Many-Body Problem, Springer Verlag, 1980.

[11] C. F. v. Weizsacker, Zur Theorie der Kernmassen, Z. Phys. A 96 (1935) 431–458.

[12] A. Bohr, B. R. Mottelson, Nuclear Structure I, New York Reading (MA), 1969.

[13] F. Tondeur, S. Goriely, J. M. Pearson, M. Onsi, Towards a Hartree-Fock mass formula, Phys. Rev. C 62 (2000) 024308.

[14] S. Goriely, Further explorations of Skyrme-Hartree-Fock-Bogoliubov mass formulas. IV: Neutron-matter constraint, Nucl. Phys. A 750 (2005) 425–443.

[15] S. Goriely, M. Samyn, P.-H. Heenen, J. M. Pearson, F. Tondeur, Hartree-Fock mass formulas and extrapolation to new mass data, Phys. Rev. C 66 (2002) 024326.

[16] P. Moller, J. R. Nix, W. D. Myers, W. J. Swiatecki, Nuclear Ground-State Masses and Deformations, At. Data and Nucl. Data Tables 59 (1995) 185.

[17] S. Goriely, Nuclear inputs for astrophysics applications, in: S. Wender (Ed.), Proc. Int. Conf. on Capture Gamma-Ray Spectroscopy and Related Topics, AIP, 2000.

[18] J. Duflo, A. P. Zuker, Microscopic mass formulas, Phys. Rev. C 52 (1995) 23.

[19] H. Koura, T. Tachibana, M. Uno, M. Yamada, Nuclidic Mass Formula on a Spherical Basis with an Improved Even-Odd Term, Prog. Theor. Phys. 113 (2005) 305.

[20] U. Hager, V.-V. Elomaa, T. Eronen, J. Hakala, A. Jokinen, A. Kankainen, S. Rahaman, S. Rinta-Antila, A. Saastamoinen, T. Sonoda, J. Äystö, Precision mass measurements of neutron-rich Tc, Ru, Rh and Pd isotopes, Phys. Rev. C 75 (2007) 064302.

[21] S. Rahaman, U. Hager, V.-V. Elomaa, T. Eronen, J. Hakala, A. Jokinen, A. Kankainen, P. Karvonen, I. Moore, H. Pentillä, S. Rinta-Antila, J. Rissanen, S. Saastamoinen, T. Sonoda, J. Äystö, Precise atomic masses of neutron-rich Br and Rb nuclei close to the r-process path, Eur. Phys. J. A 32 (2007) 87.

[22] S. Pittel, P. Federman, A unified shell-model picture of nuclear deformation, Int. Journ. Mod. Phys. E 2 (Supp. 1993) 3–16.

[23] S. Nilsson, Kgl. Dan. Viden. Selsk. Mat. Fys. Medd. 29. (1955)

[24] R. B. Firestone, Table of Isotopes, 1996.

[25] E. M. Burbidge, G. R. Burbidge, W. A. Fowler, F. Hoyle, Synthesis of the Elements in Stars, Rev. Mod. Phys. 29 (4) (1957) 547–650.

[26] H. Schatz, R. Toenjes, B. Pfeiffer, T. C. Beers, J. J. Cowan, V. Hill, K.-L. Kratz, THORIUM AND URANIUM CHRONOMETERS APPLIED TO CS 31082-001, Ap. J. 579 (2002) 626.

[27] U. Hager, A. Jokinen, V.-V. Elomaa, T. Eronen, J. Hakala, A. Kankainen, P. Karvonen, I. Moore, H. Pentillä, S. Rahaman, S. Rinta-Antila, J. Rissanen, S. Saastamoinen, T. Sonoda, J. Äystö, accepted for publication in Nucl. Phys. A (2007).

[28] G. Audi, O. Bersillon, J. Blachot, A. H. Wapstra, The NUBASE evaluation of nuclear and decay properties, Nucl. Phys. A 729 (2003) 3–128.

[29] F. Montes, A. Estrade, P. T. Hosmer, S. N. Liddick, P. F. Mantica, A. C. Morton, W. F. Mueller, M. Ouellette, E. Pellegrini, P. Santi, H. Schatz, A. Stolz, B. E. Tomlin, O. Arndt, K.-L. Kratz, B. Pfeiffer, P. Reeder, W. B. Walters, A. Aprahamian, A. Wohr, β-decay half-lives and β-delayed neutron emission probabilities for neutron rich nuclei close to the $N = 82$ r-process path, Phys. Rev. C 73 (2006) 035801.

[30] H. Savajols, The SPEG Mass Measurement Program at GANIL, Hyperfine Interactions 132 (2001) 245–254.

[31] M. Chartier, W. Mittig, G. Auger, B. Blank, J. M. Casandjian, M. Chabert, J. Fermé, L. K. Fifield, A. Gillibert, A. S. Lalleman, A. Lépine-Szily, M. Lewitowicz, M. M. Cormick, M. H. Moscatello, F. de Oliveira, N. A. Orr, G. Politi, F. Sarazin, H. Savajols, C. Spitaels, P. V. Isacker, A. C. C. Villari, M. Wiescher, The Mass Programme at GANIL Using the CSS2 and CIME Cyclotrons, Hyperfine Interactions 132 (2001) 275–281.

[32] T. Radon, H. Geissel, G. Münzenberg, B. Franzke, T. Kerscher, F. Nolden, Y. N. Novikov, Z. Patyk, C. Scheidenberger, F. Attallah, K. Beckert, T. Beha, F. Bosch, H. Eickhoff, M. Falch, Y. Fujita, M. Hausmann, F. Herfurth, H. Irnich, H. C. Jung, O. Klepper, C. Kozhuharov, Y. A. Litvinov, K. E. G. Löbner, F. Nickel, H. Reich, W. Schwab, B. Schlitt, M. Steck, K. Sümmerer, T. Winkler, H. Wollnik, Schottky mass measurements of stored and cooled neutron deficient projectile fragments in the element range of $57 \leq Z \leq 84$, Nucl. Phys. A 677 (2000) 75.

[33] Y. A. Litvinov, T. J. Burvenich, H. Geissel, Y. N. Novikov, Z. Patyk, C. Scheidenberger, F. Attallah, G. Audi, K. Beckert, F. Bosch, M. Falch, B. Franzke, M. Hausmann, T. Kerscher, O. Klepper, H.-J. Kluge, C. Kozhuharov, K. E. G. Lobner, D. G. Madland, J. A. Maruhn, G. Munzenberg, F. Nolden, T. Radon, M. Steck, S. Typel, H. Wollnik, Isospin Dependence in the Odd-Even Staggering of Nuclear Binding Energies, Phys. Rev. Lett. 95 (2005) 042501.

[34] J. Stadlmann, M. Hausmann, F. Attallah, K. Beckert, P. Beller, F. Bosch, H. Eickhoff, M. Falch, B. Franczak, B. Franzke, H. Geissel, T. Kerscher, O. Klepper, H.-J. Kluge, C. Kozhuharov, Y. A. Litvinov, K. E. G. Lobner, M. Matos, G. Munzenberg, N. Nankov, F. Nolden, Y. N. Novikov, T. Ohtsubo, T. Radon, H. Schatz, C. Scheidenberger, M. Steck, H. Weick, H. Wollnik, Direct mass measurement of bare short-lived ^{44}V, ^{48}Mn, ^{41}Ti and ^{45}Cr ions with isochronous mass spectrometry, Phys. Lett. B 586 (2004) 27–33.

[35] M. D. Lunney, G. Audi, C. Borcea, M. Dedieu, H. Doubre, M. Duma, M. Jacotin, J. F. Képinski, G. L. Scornet, M. de Saint Simon, C. Thibault, MISTRAL collaboration, MISTRAL: A new program for precise atomic mass determinations of nuclides far from stability, Hyp. Interact. 99 (1996) 105–114.

[36] D. Lunney, C. Monsanglant, G. Audi, G. Bollen, C. Borcea, H. Doubre, C. Gaulard, S. Henry, M. deSaintSimon, C. Thibault, C. Toader, N. Vieira, Recent Results on Ne and Mg from the MISTRAL Mass Measurement Program at ISOLDE, Hyp. Interact. 132 (2001) 297–305.

[37] T. Eronen, V. Elomaa, U. Hager, J. Hakala, A. Jokinen, A. Kankainen, I. Moore, H. Penttilä, S. Rahaman, J. Rissanen, A. Saastamoinen, T. Sonoda, J. Äystö, Q Values of the Superallowed Emitters ^{26}Al^m, ^{42}Sc, and ^{46}V and Their Impact on V_{ud} and the Unitarity of the Cabibbo-Kobayashi-Maskawa Matrix, Phys. Rev. Lett. 97 (2006) 232501.

[38] J. Äystö, Development and applications of the IGISOL technique, Nucl. Phys. A 693 (2001) 477–494.

[39] E. Kugler, The ISOLDE facility, Hyperfine Interactions 129 (2000) 23–42.

[40] K. Blaum, G. Bollen, F. Herfurth, A. Kellerbauer, H.-J. Kluge, M. Kuckein, S. Heinz, P. Schmidt, L. Schweikhard, Recent developments at ISOLTRAP: towards a relative mass accuracy of exotic nuclei below 10^{-8}, J. Phys. B: At. Mol. Opt. Phys 36 (2003) 921–930.

[41] M. König, G. Bollen, H.-J. Kluge, T. Otto, J. Szerypo, Quadrupole excitation of stored ion motion at the true cyclotron frequency, Int. J. Mass Spectrometry 142 (1995) 95–116.

[42] G. Sikler, Massenspektrometrie kurzlebiger Sr- und Sn-Isotope und Aufbau der SHIPTRAP-Penningfallen, Ph.D. thesis, Universität Heidelberg, diss. 2009-01 (2003).

[43] G. Bollen, S. Becker, H. J. Kluge, M. König, R. B. Moore, T. Otto, H. Raimbault-Hartmann, G. Savard, L. Schweikhard, H. Stolzenberg, I. Collaboration, ISOLTRAP: a tandem Penning trap system for accurate on-line mass determination of short-lived isotopes, Nucl. Instr. Meth. A 368 (1996) 675–697.

[44] G. Savard, S. Becker, G. Bollen, H. J. Kluge, R. B. Moore, T. Otto, L. Schweikhard, H. Stolzenberg, U. Wiess, A new cooling technique for heavy ions in a Penning trap, Phys. Lett. A 158 (1991) 247.

[45] A. Nieminen, J. Huikari, A. Jokinen, J. Äystö, P. Campbell, E. C. A. Cochrane, EXOTRAPS collaboration, Beam cooler for low-energy radioactive ions, Nucl. Instr. Meth. A 469 (2001) 244–253.

[46] V. S. Kolhinen, Penning trap for isobaric purification of ion beams at IGISOL, Ph.D. thesis, University of Jyväskylä (2003).

[47] F. Herfurth, J. Dilling, A. Kellerbauer, G. Bollen, S. Henry, H.-J. Kluge, E. Lamour, D. Lunney, R. Moore, C. Scheidenberger, S. Schwarz, G. Sikler, J. Szerypo, A linear radiofrequency ion trap for accumulation and bunching and emittance improvement of radioactive ion beams, Nucl. Instr. Meth. A 469 (2001) 254–275.

[48] G. Bollen, H.-J. Kluge, M. König, T. Otto, G. Savard, H. Stolzenberg, Resolution of nuclear ground and isomeric states by a Penning trap mass spectrometer, Phys. Rev. C 46 (1992) R2140.

[49] A. Kellerbauer, K. Blaum, G. Bollen, F. Herfurth, H.-J. Kluge, M. Kuckein, E. Sauvan, C. Scheidenberger, L. Schweikhard, From Direct to Absolute Mass Measurement: A Study of the Accuracy of ISOLTRAP, Eur. Phys. J. D 22 (2003) 53–64.

[50] F. Blönnigen, G. Bewersdorf, C. Geisse, W. Lippert, B. Pfeiffer, U. Stöhlker, H. Wollnik, Proc. 7th Int. Conf. Atomic Masses and Fundamental Constants AMCO7 (1984) 134.

[51] H. Mach, E. K. Warburton, R. L. Gill, R. F. Casten, J. A. Becker, B. A. Brown, J. A. Winger, Meson-exchange enhancement of the first-forbidden $^{96}\mathrm{Y}^{g}(0^{-})\rightarrow{}^{96}\mathrm{Zr}^{g}$ (0^{+}) β transition: β decay of the low-spin isomer of ^{96}Y, Phys. Rev. C 41 (1) (1990) 226–242.

[52] H. Raimbault-Hartmann, G. Audi, D. Beck, G. Bollen, M. de Saint Simon, H.-J. Kluge, M. König, R. B. Moore, S. Schwarz, G. Savard, J. Szerypoe, High-accuracy mass determination of neutron-rich rubidium and strontium isotopes, Nucl. Phys. A 706 (2002) 3–14.

[53] P. Peuser, H. Otto, N. Kaffrell, G. Nyman, E. Roeckl, Total β-decay energies and the mass-energy surface of very neutron-rich nuclei near mass 100, Nucl. Phys. A 332 (1979) 95–108.

[54] R. Decker, K. D. Wünsch, H. Wollnik, E. Koglin, G. Siegert, G. Jung, Präzise Q_β-Wert-Messungen mit einem Intrinsic-Germanium Detektor an leichten, neutronenreichen Spaltprodukten, Z. Phys. A 294 (1980) 35–49.

[55] M. Graefenstedt, U. Keyser, F. Münnich, F. Schreiber, Proc. 5th Int. Conf. Nuclei far from Stability NUFAST-5 AIP Conf. Proc.164 (1987) 30.

[56] M. Groß, Experimental Q_β-values of very neutron-rich light fission products in the mass range $85 \leq A \leq 108$, in: Int. conf. on Atomic Masses and Fundamental Constants, 1992.

[57] R. Iafigliola, H. Dautet, S. W. Xu, J. K. P. Lee, R. Chrien, R. Gill, M. Shmid, Proc. 7th Int. Conf. Atomic Masses and Fundamental Constants AMCO7 (1984) 141.

[58] A. G. Blair, J. G. Beery, E. R. Flynn, Nuclear States of ^{98}Zr, Phys. Rev. Lett. 22 (10) (1969) 470–473.

[59] U. Keyser, H. Berg, F. Münnich, B. Pahlmann, R. Decker, B. Pfeiffer, Proc. 6th Int. Conf. Atomic Masses and Fundamental Constants AMCO-6 (1980) 443.

[60] M. Graefenstedt, U. Keyser, F. Münnich, F. Schreiber, H. R. Faust, H. Weikard, Nuclear Structure Effects in the Mass Region Around A=100 and Derived from Experimental Q_β-Values, Z. Phys. A 327 (1987) 383–392.

[61] R. F. Casten, E. R. Flynn, O. Hansen, T. J. Mulligan, A study of the neutron-rich isotopes near A=100 by means of the (t,p) reaction, Nucl. Phys. A 184 (1972) 357–376.

[62] A. Jokinen, T. Enqvist, P. P. Jauho, M. Leino, J. M. Parmonen, H. Penttilä, J. Äystö, K. Eskola, Beta decay of ^{108}Mo and neighbouring even Mo-isotopes, Nucl. Phys. A 584 (1995) 489–508.

[63] M. Groß, P. Jürgens, U. Keyser, S. Kluge, M. Mehrtens, S. Müller, F. Münnich, J. Wulff, H. R. Faust, Determination of high Q_β-values by beta-gamma-coincidence measurements with a plastic scintillator telescope, Nucl. Instr. Meth. A 311 (1992) 512–519.

[64] M. Graefenstedt, P. Jürgens, U. Keyser, F. Münnich, F. Schreiber, K. Balog, T. Winkelmann, H. R. Faust, Experimental Beta-Decay Energies of Very Neutron-Rich Fission Products with $107 \geq A \geq 109$, Z. Phys. A 334 (1989) 239–245.

[65] M. Matoš, Isochronous Mass Measurements of Short-Lived Neutron Rich Nuclides at the FRS-ESR Facilities, Ph.D. thesis, University of Giessen (2004).

[66] J. Skalski, S. Mizutori, W. Nazarewicz, Equilibrium shapes and high-spin properties of the neutron-rich A $\approx$ 100 nuclei, Nucl. Phys. A 617 (1997) 282–315.

[67] P. Campbell, H. L. Thayer, J. Billowes, P. Dendooven, K. T. Flanagan, D. H. Forest, J. A. R. Griffith, J. Huikari, A. Jokinen, R. Moore, A. Nieminen, G. Tungate, S. Zemlyanoi, J. Äystö, Laser Spectroscopy of Cooled Zirconium Fission Fragments, Phys. Rev. Lett. 89 (2002) 082501.

[68] B. Cheal, M. Gardner, M. Avgoulea, J. Billowes, M. Bissell, P. Campbell, T. Eronen, K. Flanagan, D. Forest, J. Huikari, A. Jokinen, B. Marsh, I. Moore, A. Nieminen, H. Pentillä, S. Rinta-Antila, B. Tordoff, G. Tungate, J. Äystö, The shape transition in the neutron-rich yttrium isotopes and isomers, Phys. Lett. B 645 (2007) 133–137.

[69] P. Lievens, E. Arnold, W. Borchers, U. Georg, M. Keim, A. Klein, R. Neugart, L. Vermeeren, R. E. Silverans, On the odd-even staggering of mean-square charge radii in the light krypton and strontium region, Europhys. Lett. 33 (1996) 11–16.

[70] P. Delahaye, G. Audi, K. Blaum, F. Carrel, S. George, F. Herfurth, A. Herlert, A. Kellerbauer, H.-J. Kluge, D. Lunney, L. Schweikhard, C. Yazidjian, High-accuracy mass measurements of neutron-rich Kr isotopes, Phys. Rev. C 74 (2006) 034331.

[71] D. Brenner, R. Cakirli, R. Casten, Valence proton-neutron interactions throughout the mass surface, Phys. Rev. C 73 (2006) 034315.

[72] R. B. Cakirli, R. F. Casten, Direct Empirical Correlation between Proton-Neutron Interaction Strengths and the Growth of Collectivity in Nuclei, Phys. Rev. Lett. 96 (2006) 132501.

[73] M. Stoitsov, R. B. Cakirli, R. F. Casten, W. Nazarewicz, W. Satuła, Empirical Proton-Neutron Interactions and Nuclear Density Functional Theory: Global, Regional and Local Comparisons, submitted to Phys. Rev. Lett. (2007).

[74] N. F. Ramsey, A molecular beam resonance method with separated oscillating fields, Phys. Rev. 78 (6) (1950) 695–699.

[75] `http://www.nrbook.com/a/bookcpdf.html`.